Freie Universität Berlin

Development of Low-Temperature Photon Scanning Probe Microscopy and Nanoscale Characterization of Ultrathin ZnO Layers on Ag(111)

Dissertation
zur Erlangung des Grades eines
Doktors der Naturwissenschaften (Dr. rer. nat.)

am Fachbereich Physik
der Freien Universität Berlin

Shuyi Liu

June 2019

This work was started in June 2014 and finished in October 2018 in the group of Dr. Takashi Kumagai at the Department of Physical Chemistry of the Fritz-Haber-Institut der Max-Planck-Gesellschaft.

Berlin, June 2019

Erstgutachter: Prof. Dr. Martin Wolf

Zweitgutachterin: Prof. Dr. Stephanie Reich

Datum der Disputation: 24.09.2019

Abstract

Photon scanning probe microscopy (photon-SPM) provides a promising route to study a light-matter interaction at the nanometer scale and even down to the single-molecule level, which is an interesting topic not only for fundamental science, but also for a new evolution of nanotechnology. This thesis describes the development of a home-designed low-temperature (LT-) photon-SPM, which combines a parabolic mirror and a lens on the cold STM stage. We demonstrate that this instrument offers a precise beam alignment capability to attain highly reproducible experiments.

Using the LT-photon-SPM, we first show a novel plasmon-assisted resonant electron transfer in an scanning tunneling microscope (STM) junction, where resonant electron transfer from a plasmonic tip to field emission resonances (FERs) over a Ag(111) surface is induced by visivble continuous-wave excitation. This process can serve as a simple and intriguing model to examine the interplay between localized surface plasmon excitation and resonant electron transfer in a plasmonic nanocavity. The resonant electron transfer is observed in FER spectroscopy and the plasmon-assisted process is manifested as a downshift of the FER peaks in the spectra.

We also examined tip-enhanced Raman spectroscopy (TERS) for ultrathin ZnO layers epitaxially grown on a Ag(111) surface. The local geometric and electronic structure of ZnO/Ag(111) is investigated by combined experiments of STM, STS, and atomic force microscopy. With increasing thickness of the ZnO layers, the conduction band minimum was found to downshift as well as the work function was reduced. Strong TERS signals for 2-ML and 3-ML ZnO were obtained under the conditions where both chemical and physical enhancement mechanisms were satisfied. It is also revealed that the TERS intensity is sensitive to the local electronic structure leading to a high spatial resolution of TERS is below 1 nm.

Kurzfassung

Die Photon-Scanning-Probe-Mikroskopie (Photon-SPM) bietet eine vielversprechende Möglichkeit, die Wechselwirkung zwischen Licht und Materie im Nanometerbereich oder sogar bis auf die Ebene einzelner Moleküle zu untersuchen. Dies ist sowohl für die Grundlagenforschung als auch für neue technologische Anwendungen interessant. In dieser Arbeit wurde ein selbstgebautes Tieftemperatur (LT-) Photon-SPM entwickelt und dessen neuartigen Fähigkeiten demonstriert. In das LT-Photon-SPM wurde ein Parabolspiegel mit präziser Bewegungssteuerung integriert, der durch Piezoelemente auf dem kalten SPM-Tisch gesteuert werden und dadurch eine hochwertige und bequeme Ausrichtungsmöglichkeit für die Durchführung reproduzierbare Experimente bietet.

Mit dem LT-Photon-STM wurde ein neuartiger resonanter Elektronentransfermechanismus in einer plasmonischen Nanokavität entdeckt, bei dem plasmonisch unterstütztes Elektronentunneln von einer plasmonischen Spitze zu Feldemissionsresonanzen über der Ag(111)-Oberfläche durch CW-Laseranregung im sichtbaren Bereich induziert wird. Korrelationen zwischen der laserinduzierten Änderung der FER-Spektren und den plasmonischen Eigenschaften des Übergangs wurden untersucht. Als Kennzeichen eines plasmonunterstützten resonanten Tunnelprozesses wurde ein Herabschieben des ersten Peaks in den FER-Spektren beobachtet, die der einfallenden Photonenenergie entspricht.

Ebenfalls wurde die spitzenverstärkte Raman-Spektroskopie für ultradünne ZnO-Schichten untersucht, die epitaktisch auf einer Ag(111)-Oberfläche gewachsen wurden. Die lokale geometrische und elektronische Struktur von ZnO/Ag(111) wurde durch kombinierte Experimente mit STM, STS und Rasterkraftmikroskopie untersucht. Mit zunehmender Dicke der ZnO-Schichten wurde festgestellt, dass sich die Position des Leitungsbandminimum energetisch verringerte, genauso wie die Austrittsarbeit. Starke TERS-Signale für 2-ML- und 3-ML-ZnO blieben unter Bedingungen erhalten, bei denen sowohl chemische als auch physikalische Verstärkungsmechanismen erfüllt sind. Es hat sich auch gezeigt, dass die TERS-Intensität empfindlich gegenüber der lokalen elektronischen Struktur ist, was dazu führt, dass die hohe räumliche Auflösung von TERS unter 1 nm liegt.

Abbreviations

AFM atomic force microscopy

CPD contact potential difference

FER field emission resonance

IRAS infrared reflection absorption spectroscopy

LT-photon-SPM low temperature photon scanning probe microscopy

LDOS local density of states

ML mono-layer

NA numerical aperture

NPc naphthalocyanine

STM scanning tunneling microscopy

STHM scanning tunneling hydrogen microscopy

STS scanning tunneling spectroscopy

SPM scanning probe microscopy

STML scanning tunneling microscope induced luminesecence

SPP surface plasmon polariton

SERS surface enhanced Raman spectroscopy

SXRD surface x-ray diffraction

TERS tip enhanced Raman spectroscopy

UHV ultra-high vacuum

Contents

1 Introduction 1

2 Basic principles of Methods: STM, AFM, photon-SPM, TERS 9

2.1 Scanning tunneling spectroscope (STM) 9

2.1.1 Working principle of STM 9

2.1.2 Scanning tunneling spectroscopy (STS) 11

2.2 Atomic force microscopy (AFM) 12

2.2.1 Working principle of AFM 12

2.2.2 Contact potential difference (CPD) 14

2.4 Tip enhanced Raman spectroscopy (TERS) 15

2.4.1 Classical description of Raman scattering 15

2.4.2 Quantum description of Raman scattering 17

2.4.3 Enhanced Raman spectroscopy 19

2.4.4 Selection rule of TERS 22

2.3 Photon SPM 22

2.3.1 Introduction 22

2.3.2 Technical challenges of photon-SPM 23

2.3.3 Strategy of SPM combined with optics 24

2.3.4 Customized optical SPM system 26

2.3.5 Optical alignment 29

2.4 Preparation of ultra-thin ZnO layers on Ag(111) 30

3 Plasmon assisted electron tunneling 32

3.1 Introduction 32

3.2 FER spectra under illumination 33

3.3 Plasmon assisted tunneling 38

3.4 Plasmon-assisted tunneling over 2-ML ZnO/Ag(111) 41

3.5 Conclusion 41

4 Local characterization of ultrathin ZnO layers on Ag(111) by SPM 43

4.1 Local geometric and electronic structure of the ultrathin ZnO layers on Ag(111) 43

4.1.1 Introduction 43

4.1.2 STM imaging and band structures 44

4.1.3 Local work function measurement 47

4.1.4 Conductance maps 51

4.1.5 Conclusions 53
4.2 STHM imaging for ZnO layers on Ag(111) 53
4.2.1 Introduction 53
4.2.2 STHM imaging of ZnO layers, conductance and mechanical properties of the junction 54
4.2.3 Simulation of the junction with two H_2 inside 61
4.2.4 Defective feature of 3-ML ZnO layer 66
4.2.5 Conclusion 67
5 TERS measurement of ultrathin ZnO layers on Ag(111) 68
5.1 Introduction 68
5.2 TERS over ultrathin ZnO layers 68
5.3 Enhancement mechanism of TERS 72
5.4 Interaction between ZnO layer and Ag(111) 74
5.3 Conclusions 75
6 Summary and outlook 77
Bibliography 81
Publications 97
Acknowledgments 99

1 Introduction

Interaction between light and matter is a ubiquitous phenomena in daily life and of fundamental importance in many areas of science and technology. A prominent example in nature is photosynthesis in plants to convert solar energy into chemical energy where photon absorption and charge separation are the elementary processes. The reversed process, *i.e.*, charge recombination and light emission, is also the basis of optoelectronic devices such as light emitting diodes (LEDs). Understanding of such elementary processes at the atomistic level has become more and more important in modern physical chemistry, surface science, and biophysics, whereby microscopy can explore heterogeneity hidden in the ensemble [1]. Studying light–matter coupling at the nanoscale is scientifically important and may also lead to various applications, such as metal nanoparticle arrays that can enhance light emission in LEDs [2] or the photovoltaic energy conversion efficiency [3].

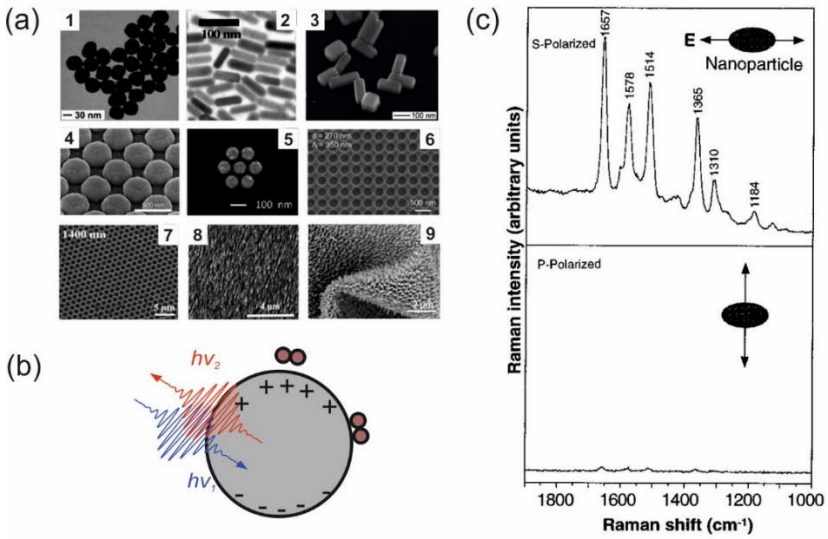

Figure 1.1. (a) SEM images of various types of nanoparticles or nanostructures for a SERS measurement. (1)-(3) Colloidal structures: Spherical gold nanoparticles, gold nano-rods, and silver nano-bar. (4)-(6) Solid structure: silver plasmonic nanodome array, gold nanocluster and gold nano-holes. (7)-(9) Flexible structures: silver nano-voids, silver nano-columnar film, and silver nano-pillars [*Nanophotonics* 6(5), 831–852 (2017)]. (b) Schematic of SERS process. The gray circle represents a metallic nanoparticle and the dark red circles adsorbed

molecules. (c) SERS spectra obtained for a single rhodamine 6G molecule adsorbed on an ellipsoidal shape Ag [*Science* 275, 1102–1106 (1997)]. The field enhancement occurs with an incident beam polarized parallel to the long axis of ellipsoid, leading to much stronger Raman signal with the beam polarized perpendicular to it.

One of the most important applications of light–matter interactions is materials characterization, *i.e.*, spectroscopy including fluorescence, infrared absorption, Raman scattering, X-ray diffraction, to name a few. They are commonly used in modern science to reveal structures and dynamics of various materials. Optical microspectroscopy is a powerful tool to investigate microscopic structures and properties of materials. However, the spatial resolution is typically limited by the diffraction limit to roughly a half of wavelength (hundreds of nanometers in the visible range), which hinders direct observation of nanoscale materials and single molecules. Near field is an electromagnetic field localized in tens of nanometers region from a surface or interface. It can overcome the diffraction limitation for the microspectroscopy and surface plasmon of metallic nanostructures play a crucial role in that.

Surface plasmon plays a central role in the field of plasmonics. The control of surface plasmons has been rapidly developed with the advances of nanoscale fabrication techniques and has provided many applications in a wide range of research areas including biosensing [4], photovoltaics [5], photochemistry [6], and optical engineering at nanoscale (nano-optics) [7]. Surface enhanced Raman spectroscopy (SERS) is one of the important applications of plasmonics, which allows ultrasensitive vibrational spectroscopy even down to the single-molecule level [8]. The discovery of surface enhanced Raman scattering dates back to 1970s, and was discovered for pyridine molecules adsorbed on roughened silver surfaces [9]. The enhancement mechanism has been attributed to surface plasmon excitation [10, 11, 12]. SERS has also been benefited from the development of nanoscience and nanotechnology in the last few decades as plasmonically active nanoparticles or surfaces can be synthesized as shown in **Figure 1.1a**. **Figure 1.1b** illustrates the SERS process on a metallic nanoparticle. The incident laser excites a localized surface plasmon of the nanoparticle, which results in a strongly enhanced near field. The interaction of this near-field and adsorbed molecules leads to an enhancement of the Raman scattering process. **Figure 1.1c** shows the SERS spectrum of single rhodamine 6G molecule. Although SERS has a very high chemical sensitivity, it does not offer

imaging capability, which hampers to examine the correlation between nanostructure and near-field properties as well as details of the enhancement mechanisms of the Raman scattering process. Tip-enhanced Raman spectroscopy (TERS) has emerged as a promising approach to endow imaging capability for SERS—a combination of SERS with a scanning probe microscope (SPM) which offers atomic resolution imaging [13, 14, 15, 16].

SPM was invented in 1980s when scanning tunneling microscopy (STM) was first reported in the early 1982 [17] and atomic force microscopy (AFM) was developed later [18]. SPM is a powerful tool to investigate nanoworlds and has become one of the central analytical methods in nanoscience and nanotechnology. In addition to the imaging capability with atomic resolution, SPM can also perform various local spectroscopies at the atomic scale. For example, scanning tunneling spectroscopy (STS) can study the local electronic states [19, 20], the vibrational energy can be measured by inelastic electron tunneling spectroscopy (IETS) [21] and by STM action spectroscopy in which the vibrational excitation induced reactions of single molecules are directly observed [22], and the local work function can be measured by field emission resonnce (FER) and contact potential difference (CPD) measurement [23]. Manipulation of single atoms and molecules is another very unique ability of SPM, which allows to make artificial structures and examine fundamental physics at nanoscale. For example, a first demonstration of SPM manipulation is “atomic letters” made by positioning individual Xenon atoms [24], followed by quantum corrals constructed with tens of atoms on a metal surface which lead to confinement of the surface electrons [25]. Combing SPM with optics can further extend the capability of SPM [26, 27]. Photon-SPM—a combination of SPM with optical excitation and detection as schematically shown in **Figure 1.2a**—has emerged as a promising approach to investigating light–matter interactions at the nanoscale, even down to the atomic and molecular level. For example, STM-induced luminescence (STML) is a typical measurement by photon-SPM as exampled in **Figure 1.2b**. In photon-STM, radiation of the localized surface plasmon in the junction is detected, which is excited through inelastic electron tunneling. Vibrational features have also been observed in the STML of single porphyrin molecules [28, 29, 30]. Recently, coherent intermolecular dipole-dipole coupling between zinc-phthalocyanines molecules [31], resonance energy transfer from a magnesium phthalocyanine molecule to a free-base phthalocyanine molecule [32] have been demonstrated with photon-SPM.

Metallic nanocavities play an important role in plasmonics as they can confine light to nanometric volumes and generate strong field enhancement [33]. Experimentally, the size and

geometry of a nanocavity are challenged to be determined precisely (with Ångström accuracy), and near-field properties in such nanocavities imperfectly understood. Because SPM can control the gap distance with the sub-Ångström precision and can also determine morphology of the sample surface, the photon-SPM has the advantage to study the near-field properties of controlled sub-nanometer gaps. The interplay between surface plasmon excitation and electron transfer in nanocavities are intimately related to applications in photovoltaics, photo-catalysis and so on [34]. To reveal the underlying physical mechanisms, it is essential to investigate the plasmonic property and plasmon-induced processes for well-define nanocavities. As a test case, we study plasmon-assisted resonant electron tunneling from tip to field emission resonances (FERs) in an STM junction. This process can serve as a simple and intriguing model to examine the interplay between localized surface plasmon excitation and resonant electron transfer in a plasmonic nanocavity.

Tip enhanced Raman spectroscopy (TERS) is another prominent experimental technique in photon-SPM which combines scanning probe microscopy (SPM) with surface enhancend Raman spectroscopy [35, 36, 37,15]. Vibrational features of various single molecules have been observed by TERS [38]. In TERS experiments, an Au or Ag tip and substrate are typically used because they are plasmonic materials active for visible light. An electromagnetic field in the STM junction is strongly enhanced through surface plasmon excitation. TERS has evolved as a promising technique for nanoscale vibrational microspectroscopy and demonstrated the ability to resolve surface morphology along with chemical sensitivity even at sub-nanometer scale as shown in **Figure 1.2c**. However, there are still some technical challenges (such as instrumental design, laser beam alignment) and scientific questions (such as spatial resolution, selection rule) remain to be explored [39, 40, 41].

The achievable spatial resolution of TERS is still under discussion. Previously, it was shown that the spatial resolution of TERS is typically limited to be 3 to 15 nm [42, 43, 44, 45, 46, 47]. However, Dong and coworker in China reported the first sub-nanometer resolution TERS experiment in 2013 (**Figure 1.2b**) [48]. They observed a non-linear Raman scattering process similar as third order stimulated Raman scattering and the extremely-high spatial resolution was attributed to this non-linearity. In this thesis, we demonstrate that spontaneous Raman scattering can also offer sub-nanometer resolution. Optical response of the nanocavity is usually simulated using classical electrodynamics by solving Maxwell's equations. However, in TERS measurements, the gap distance could approach to the sub-nanometer regime where the quantum mechanical effects become important. Thereby, non-local effects and quantum

tunneling of electrons in the nanocavity have to be taken into account, which leads to shift of the plamon resonance and reduce the field enhancement compare to a pure classical description [49]. Recently, it has been proposed that an atomic-scale protrusion in plasmonic cavity can confine the field at the sub-nanometer scale [50] and a quantum theory description is necessary for a comprehensive understanding of the plasmonic response at the sub-nanometer scale [51].

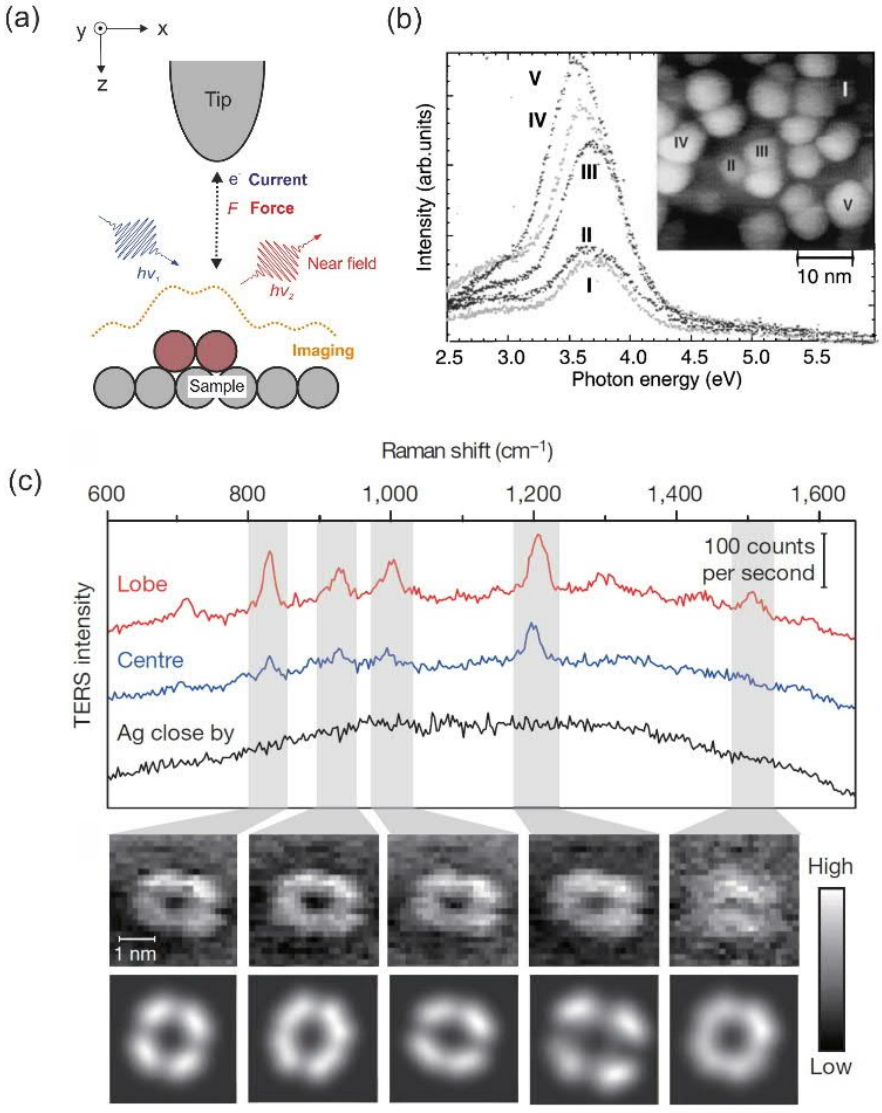

Figure 1.2. (a) Schematic of photon-SPM. Structure of these systems is a junction consisting of a tip and a sample that is an atomically flat surface with adsorbates (atom, molecule, cluster, ultra-thin films). The working distance between the tip and the sample (*z* direction) is a few Å to nanometers, also include the relative lateral positions (*x* and *y* directions), which are controlled by a feedback circuit. The tunneling current and force can be detected by STM and AFM, respectively. A laser

beam can be focused on the junction and the optical signal can be detected with optical setup. (b) (c) Typical measurements by phonon-SPM. (b) is the STML measured with tip over Ag clusters [*Phys. Rev. Lett.* 84, 3994 (2000)]. The STML spectra show different intensity and the resonance wavelength represents plasmon properties of the different size clusters. (c) is the TERS mapping for single meso-tetrakis (3,5-di-tertiarybutylphenyl)-porphyrin molecule [*Nature* 498, 82–86 (2013)]. The TERS shows a sub-nanometer spatial resolution that can do single molecule chemical mapping.

Selection rules are of fundamental importance in vibrational spectroscopy. Molecular vibrations that causes a change in polarizability are Raman active and symmetric vibrations usually have a large cross section in normal Raman scattering. However, when the size of the confined field becomes comparable with the scale of molecules, the field gradient is not uniform any more. Therefore, the selection rules applied in the normal Raman scattering may not be maintained for TERS [39, 52, 53]. Due to the specific field distribution in TERS, also silent modes could be excited [39] and vibrations perpendicular to the surface would be enhanced [48, 54, 55, 56].

Single-molecule detection has been achieved with TERS by several groups for different dye molecules [57, 44, 58]. To obtain a sufficient enhancement factor, both the physical and chemical resonance conditions need to be satisfied in TERS measurements. The physical resonance requires spectral matching of plasmonic resonance with the frequency of incident and scattering light. It can be satisfied generally because plasmonic resonance of the junction can be tuned by changing the tip apex conditions by tip-forming procedure *i.e.*, applying a short voltage pulse between tip and substrate or by poking the tip into substrate in a controlled manner [59]. The chemical resonance requires the excited photon energy matches with optical gap of measured sample. To meet chemical resonance conditions, a proper laser wavelength should be chosen. We clearly demonstrate that the two resonance conditions contribute to the TERS signal.

Stability is a practical challenge in TERS measurement. Plasmon excited in the junction decays non-radiatively and generates “hot electrons” [60]. In plasmonic nanocavities, chemical reactions can be triggered either by the enhanced field directly or by the hot carriers in the junction [61, [62]]. Therefore, such induced diffusion or desorption processes can occur during

TERS measurements, which implies practical problems to obtain stable spectra. On the other hand, plasmon excitation can be useful to drive chemical reactions intentionally [63]. For example metallic nanoclusters have attracted increasing attention for the fundamental science research and possible applications to plasmonic catalysts [64, 65, 66, 67, 68, 69, 70]. As a sample for TERS measurement should be stable enough to avoid the possible diffusion, desorption and chemical reaction, we have studied ultrathin ZnO layers as a model system to apply TERS that is stable during the measurement.

Oxide films have wide-ranging applications in catalysis [71], electronic devices [72], gas sensors [73]. Ultrathin oxide films grown on a single crystal metal surface exhibit well-defined structures [74] and often exhibit distinctive properties from the bulk materials resulting from the interaction with the metal substrate, such as strain due to lattice mismatch [75]. They have been often used as a support for metal nanoparticles in model catalysis research [76], which are suitable for various surface science techniques such as STM, low energy diffraction, and photoelectron spectroscopy. Properties of ultrathin oxide films, with a thickness of a few monolayers, vary depending on the number of layers [77]. And the nature of such materials cannot be extrapolated from the bulk crystals. However, growing thicker films on metal surface will be a protocol to infer the structures and properties of bulk oxide surfaces [78]. Because local properties play critical role in oxide materials, it is essential to characterize these with local techniques. For example, the presence of intrinsic and extrinsic defects make the wurtzite ZnO be n-type semiconductor [79], oxygen vacancy plays central role for chemical reactions on the TiO_2 surface such as water dissociation, CO oxidation and so on [80]. In this thesis, ultrathin ZnO layers epitaxially grown on a Ag(111) surface are studied in detail with local techniques SPM, STS and TERS. Molecular hydrogen trapped inside STM junction can enhance the spatial resolution to resolve submolecular structures of planar organic molecules [81], which is named as scanning tunneling “hydrogen” microscopy (STHM). The ZnO layer system is also used as a model system to verify the modified STHM and to study the fundamental process of TERS.

This thesis is organized as follows:

Chapter 2 describes the physical principle of STM, AFM, and TERS. Our customized photon-SPM setup is also introduced.

Chapter 3 describes plasmon-assisted resonant tunneling in plasmonic STM junctions consisting of a Ag or Au tip and a Ag(111) surface. The resonant tunneling process occurs via

FERs formed over the Ag surface. As a hallmark of the plasmon-assisted resonant tunneling, we observe a downshift of the first peak in the FER spectra by a fixed amount equal to the incident photon energy. STM-induced luminescence measurement for the Ag and Au tip reveals the clear correlation between the laser-induced change in the FER spectra and the plasmonic properties of the junction. The plasmon-assisted tunneling process is also observed over the ultrathin ZnO layers, which have different work function from the Ag(111) surface. Our results clarify a novel resonant electron transfer mechanism in a plasmonic nanocavity.

Chapter 4 describes the local characterization of ultrathin ZnO layers epitaxially grown on the Ag(111) surface using the reactive deposition method. Local electronic structure and local work function of different thickness ZnO layers are investigated by STM, STS and CPD. Atomic resolution imaging of 2- and 3-ML ZnO is also obtained by using scanning tunneling "hydrogen" microscopy (STHM). Both local work function measuring and atomic resolution imaging show structure transition between 2- and 3-ML ZnO layers. Conductance and mechanical properties of the STHM junction were also investigated in detail. We propose a new STHM imaging mechanism different from the previous studies [82]. It is found that the junction involves multiple H_2 and a simplified model with two H_2 inside the STM junction was suggested and simulated to reproduce the experimental observations.

Chapter 5 describes the TERS measurement of the ultrathin ZnO layers on Ag(111). In TERS spectra, the characteristic vibrational modes are observed, which are red-shifted as compared to those of the bulk ZnO. The TERS intensity linearly depends on the laser fluence, indicating spontaneous Raman scattering. The TERS intensity also strongly depends on the excitation wavelength and on the localized surface plasmon resonance of the STM junction. The crucial role of the spectral matching effect (chemical enhancement mechanism) is clearly demonstrated for 2- and 3-ML ZnO layers which have a different conduction band minimum. Furthermore, in combination with STS, it is revealed that the local electronic structure significantly affects the TERS intensity. Finally, we examine the spatial resolution of TERS using a step edge between the bare Ag surface and the ZnO layer, showing the nanometer-scale spatial resolution of nanometer-scale resolution which differs inside and outside the tunneling regime. Our results suggest that TERS will be a very powerful tool to study local structures and properties of low-dimensional materials at the nanometer scale.

Chapter 6 summarizes the finding and gives an outlook of this thesis.

2 Basic principles of Methods: STM, AFM, photon-SPM, TERS

2.1 Scanning tunneling spectroscope (STM)

2.1.1 Working principle of STM

STM was invented by Binnig and Rohrer in 1982 [83]. Its working principle relies on quantum tunneling of electrons. As illustrated in **Figure 2.1a**, a bias voltage (usually from several mV to several V) is applied between the tip and the sample to generate a small current flow (usually from several pA to tens of nA) in the STM junction. Thus, a conductive sample is necessary for STM measurements. The tunneling current exponentially decays as the tip–sample distance increases, which is used to control the vacuum gap distance at high precision. STM imaging can be performed with the constant height or constant current mode. In the constant height mode, the tip–sample distance is fixed during scanning and the variation of the tunneling current is recorded. In the constant current mode, the tunneling current is fixed to the constant value and the topographic image of the surface is recorded.

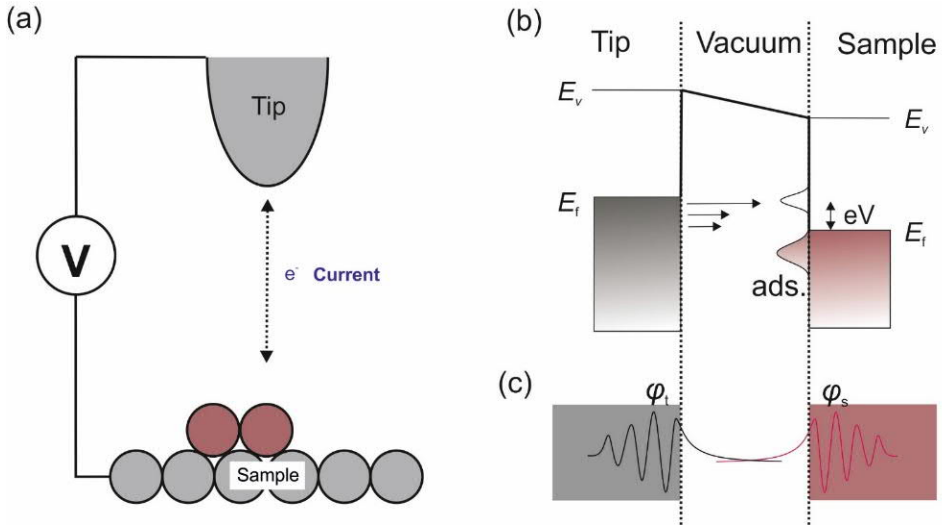

Figure 2.1. (a) Schematic of scanning tunneling microscopy. (b) Energy diagram of the biased STM junction. Adsorbate forms hybridized states on the surface. (c) Schematic of the distribution of wave functions.

The current flows between the tip and sample as a consequence of electron tunneling, where the electrons near the Fermi level tunnel through the vacuum barrier as shown in **Figure 2.1b**. The original equilibrium situation is lifted by the applied bias *V*. The Fermi level (E_f) of the tip is higher by *eV* than that of the sample, then the electrons in the range from E_f to *eV* can tunnel from the filled states of the tip to the empty states of the sample.

Electron tunneling in STM junctions can be described by Bardeen's approach [84], which is also called the transfer Hamiltonian method and extended later by Tersoff and Hamann [85,86]. In Bardeen's approach, the electron tunneling is treated as a one-particle process. Coupled electronic states through the interaction between tip and sample are also ignored. These approximations are valid for a low tunneling regime. This is the case for the STM junction with a typical vacuum barrier width of ~1 nm. The eigenstates of the sample (φ_S) and the tip (φ_T) are separated as illustrated in **Figure 2.1c**. The *k*th eigenstate satisfies the Schrödinger equation in one dimensional potential:

$$i\hbar\frac{\partial\varphi_j^k}{\partial t} = \left(-\frac{\hbar^2}{2m}\frac{\partial^2}{\partial z^2} + U_j\right)\varphi_j^k \qquad (2.1)$$

where *j* is S or T, U_j the potential function of the tip or the sample, *m* electron mass, $\hbar$ reduced Planck constant, and $\varphi_j = \varphi_j^k e^{-iE_k t/\hbar}$ with eigenenergy E_k (*k*=1, 2, 3...). In the tunneling regime, the time evolution is governed by Schrödinger equation containing the full potential:

$$i\hbar\frac{\partial\varphi}{\partial t} = \left(-\frac{\hbar^2}{2m}\frac{\partial^2}{\partial z^2} + U_S + U_T\right)\varphi \qquad (2.2)$$

where φ is the wave function of the whole system including the tip and the sample. Considering electron tunneling from a tip state φ_T^n (*n*=1, 2, 3…) to the sample, φ can be expanded in a linear combination of φ_j^k:

$$\varphi = a_m(t)\varphi_T^m e^{-iE_m t/\hbar} + \sum_{k=1}^{\infty} c_k(t)\varphi_S^k e^{-iE_k t/\hbar} \qquad (2.3)$$

where $a_n(t)$, $c_k(t)$ are coefficients. By inserting equation (2.3) into equation (2.2), the tunneling probability per unit time is obtained:

$$P_{mn} = \frac{d}{dt}|c_n(t)|^2 = \frac{2\pi}{\hbar}\delta(E_T^m - E_S^n)|M_{mn}|^2 \qquad (2.4)$$

where $M_{mn} = < \varphi_S^n | U_S | \varphi_T^m >$ is the tunneling matrix. This single electron tunneling rate from a state φ_T^m to φ_S^n follows Fermi's Golden rule, which is a general consequence of the first-order time-dependent perturbation theory. Using equation (2.4), the total tunneling current is obtained as the sum of every single electron tunneling rate in the energy range of eV:

$$I_{T\to S} = \frac{2\pi e}{\hbar}\sum_{mn}|M_{mn}|^2\delta(E_T^m - E_S^n - eV) \qquad (2.5)$$

In Tersoff and Hamann approach, a spherically symmetric function (s-wave) around r_0 is used for the tip wave function. The total tunneling current is then proportional to the local density of states of the sample and experientially decays as the barrier width increases:

$$I \propto \int_{E_F}^{E_F+eV} \rho(r_0, E)dE \qquad (2.6)$$

where $\rho(r_0, E) = \sum_k |\varphi_S^k(r_0)|^2\,\delta(E_k - E)$, is the local density of states of sample. For a small bias V, $\propto e^{-Az}$, in which $A = \frac{1}{\hbar\sqrt{2m\phi}}$, ϕ is the work function of the tip and the sample (assumed to be equal). The above approaches describe a general picture of the tunneling process in which the total tunneling current arises from all relevant orbitals and the tunneling probability exponentially decays as the barrier width increases.

2.1.2 Scanning tunneling spectroscopy (STS)

STS is a powerful electronic spectroscopy at the nanoscale that can measure the local electronic states even with the atomic-scale resolution. According to equation (2.6), the conductance dI/dV of the junction is proportional to the local density of states. This channel is commonly detected by means of the lock-in technique. In the measurement, the bias voltage is modulated by a small oscillation voltage $V_{mod}\sin\omega t$. Then the modulated tunneling current is given by Taylor expansion:

$$I(V + V_{mod}\sin\omega t) = I(V) + \frac{dI}{dV}V_{mod}\sin\omega t + \cdots. \qquad (2.7)$$

The current at the frequency ω can be selectively extracted by the lock-in amplifier, which is proportional to the conductance.

The STS can be measured either with the constant height mode or the constant current mode. In the former case, the tip–sample distance is fixed during the bias sweep. The measured conductance spectrum corresponds to the local density of states. In the latter case, the tip–sample distance is varied during the bias sweep to keep the tunneling current constant, in which the measured spectrum does not directly represent the local density of states but the electronic resonance still can be resolved. In this method, saturation of tunneling currents in the trans-impedance amplifier can be avoided, allowing to measuring a broad voltage range.

2.2 Atomic force microscopy (AFM)

2.2.1 Working principle of AFM

Force between a probe tip and a sample surface is detected in AFM that was invented in 1986 by Binnig, Quate, and Gerber [87]. In contrast to STM, a conductive sample is not required so that characterization of insulate materials is also possible by AFM. A tip is mounted on a cantilever as shown in **Figure 2.2a**, and force acting between the tip and the sample is detected as a variation of the resonant frequency of the cantilever oscillation. There are static and dynamic operation modes in AFM. In the static mode, deflection of the cantilever caused by the force acting on the tip is detected that is widespread to obtain nanometers resolution. We performed all the measurement with dynamic mode (frequency modulation mode) in this thesis, which is routinely used to obtain atomic resolution images (non-contact AFM). The cantilever oscillates at its resonance frequency f_0 that is excited by a mechanical actuator in the dynamic mode. The oscillation amplitude or the frequency shift is detected to measure the force acting on tip.

In this thesis, qPlus sensor is used to perform AFM measurements, which simplified the AFM construction significantly, also allows measuring STM simultaneously [88]. The qPlus sensor has been invented by Franz J. Giessibl in 1996, which is currently used in many ultra-high vacuum AFM systems [89]. In qPlus sensor (**Figure 2.2 b**), the cantilever is made of quartz that is surrounded by gold electrodes as schematically show in **Figure 2.2c**. Due to the piezoelectricity of the quartz, the distortion of cantilever generates surface charges that can be collected by the electrodes, so that the mechanical signal is converted to the electronic version. Vice versa, the oscillation of cantilever can also be excited by the applied bias through the electrodes. Oscillation of the cantilever is controlled and monitored by phase locked loop [88].

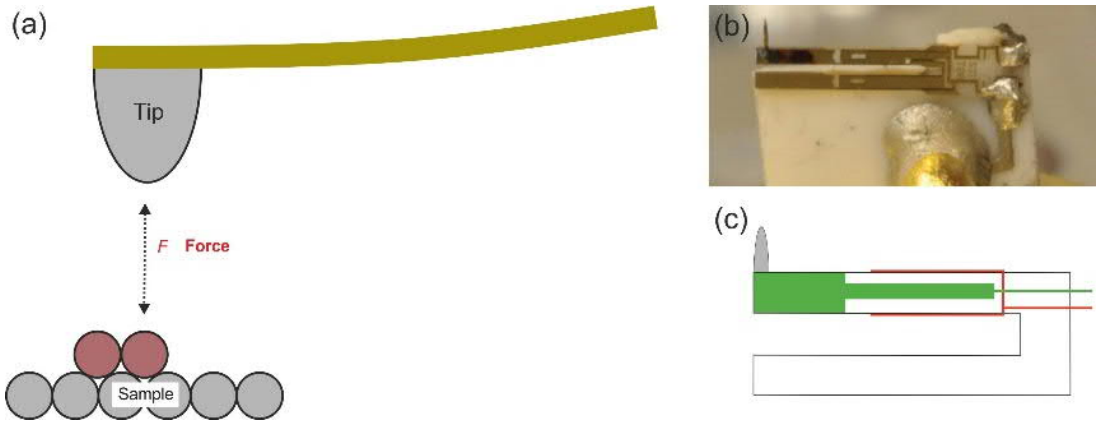

Figure 2.2. (a) Schematic of atomic force microscopy. (b) Picture of the qPlus sensor we used. (c) Schematic of the qPlus sensor. The green and red part are the gold electrodes.

The resonance frequency of the cantilever without force acting on the tip is given by

$$f_0 = \frac{1}{2\pi}\sqrt{\frac{k}{m}}, \qquad (2.8)$$

where k is the spring constant and m is the effective mass of the sensor. In a simple case, the interaction between the tip and sample is consider as a restoring force with the spring constant k_{ts}, which makes the resonance frequency shift. The shifted resonance frequency of the cantilever is given by

$$f = \frac{1}{2\pi}\sqrt{\frac{k + k_{ts}}{m}}. \qquad (2.9)$$

if $k_{ts} \ll k$, the resonance frequency shift can be approximated

$$\Delta f \approx \frac{f_0}{2}\frac{k_{ts}}{k}, \qquad (2.10)$$

In practice, the interaction between the tip and the sample is not a simple restoring force with the spring constant k_{ts}. In particular, for the measurement with a large amplitude oscillation at a small tip–sample distance, the simple consideration deviates significantly. At a small tip–sample distance, the Pauli repulsion will be predominated. The force acting on tip is

r^{-7} decay as the distance r increases, which is different from the linear dependence of a recover force. However, Giessibl [90] has derived the formula of the frequency shift for an arbitrary force $F(z)$ acting on the tip with any vibration amplitude a.

$$\Delta f = -\frac{f_0}{\pi a k}\int_{-1}^{1} F\big(z + a(1+u)\big)\frac{u}{\sqrt{1-u^2}}du\ , \qquad (2.12)$$

where Δf is the frequency shift, f_0 is the resonance frequency, k isthe spring constant of the cantilever, and z is the distance between tip and sample. To determine the force from the measured frequency shift, Sader and Jarvis derived the formula by inverting equation (2.12) [91], giving the interaction force:

$$F(z) = 2k\int_{z}^{\infty}\left(1+\frac{a^{0.5}}{8\sqrt{\pi(t-z)}}\right)\frac{\Delta f(t)}{f_0} - \frac{a^{1.5}}{\sqrt{2(t-z)}}\frac{d\left(\Delta f(t)/f_0\right)}{dt}\,dt\ . \qquad (2.13)$$

The interaction energy $U(z)$ between tip and sample can be obtained by integrating equation (2.13):

$$U(z) = 2k\int_{z}^{\infty}\frac{\Delta f(t)}{f_0}\left((t-z) + \frac{a^{0.5}}{4}\sqrt{\frac{t-z}{\pi}} + \frac{a^{1.5}}{\sqrt{2(t-z)}}\right)dt\ . \qquad (2.14)$$

2.2.2 Contact potential difference (CPD)

CPD can be used to measure the local work function by AFM. Work functions of the tip and the sample are usually different, which result in a contact potential when they are close enough to the surface. The tip and the sample have the same vacuum level when they are at a large distance, as schematically shown in **Figure 2.3a**. Their Fermi levels may be different. When the tip–sample distance is reduced to the tunneling regime, the charge transfer happens between them because of the different Fermi levels. This generates an electrostatic field in the junction (**Figure 2.3b**) that responds to the potential drop V_{CPD}. Amount of the CPD corresponds to the work function difference between the tip and the sample. The contact potential can be compensated by an applied bias of V_{CPD} as shown in **Figure 2.3c**.

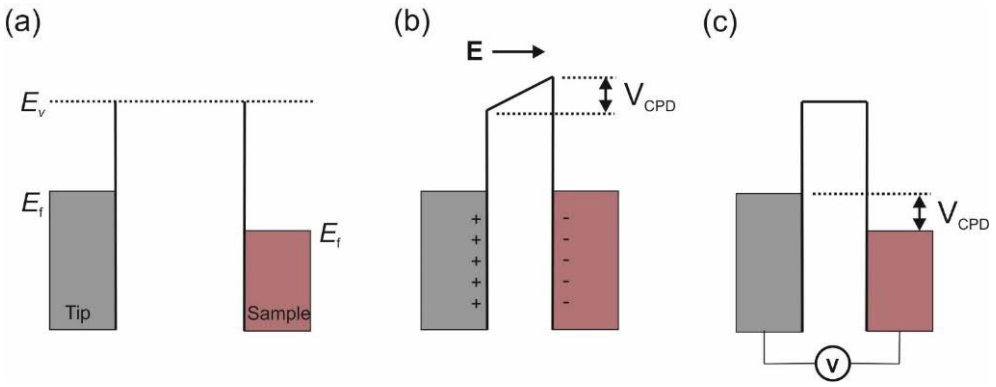

Figure 2.3. (a) Energy diagram of tip and sample at a large distance. They share the same vacuum level. The Fermi levels are different because of their different work functions. (b) In the tunneling regime, the charge transfer between tip and sample occurs to makes the Fermi level aligned, which creates the electrostatic field inside the junction. (c) The electrostatic field can be compensate by the applied bias (V_{CPD}).

The electrostatic field in the junction causes extra electric force on the tip that is

$$F_{el.st.} = \frac{1}{2}\frac{\partial C}{\partial z}(V_{CPD} - V)^2 \qquad (2.15)$$

where C is the capacity of the junction (the tip–sample junction can be regard as a capacitor), z and V are the distance and the applied bias voltage between tip and sample, respectively. From equation (2.12), it is clear that the observed frequency shift is proportional to the force acting on the tip. The applied bias V swept with tip–sample distance fixed in CPD measurements. From equation (2.15) a frequency shift curve is expected to be a parabolic shape as shown in **Figure 4.5** of chapter 4. The contact potential difference V_{CPD} corresponds to the bias of the maximum of the parabolic response in the frequency shift curve. Since the electrostatic field is mainly located under the tip apex, a spatial resolution ~1 nm can be obtained in the CPD measurement.

2.3 Tip enhanced Raman spectroscopy (TERS)

2.3.1 Classical description of Raman scattering

Raman scattering is an inelastic process upon the interaction of light with matter. A photon with the energy E_i exchanges a energy quantum (vibration or other excitation) with the matter, which results in the photon energy becomes to be E_f. This energy exchange can create a quantum of vibrational energy in the matter that is named Stokes Raman process. In that case $E_i > E_f$, it can also annihilate a quantum of vibrational energy in the matter that is named Anti-Stokes Raman process.

The spontaneous Raman scattering can be described in classical theory [92]. The most significant multipole source is the electric dipole oscillator. For a simple consideration, an incident light induces an oscillating electric dipole of the matter, leading to light emission to almost every direction (emission along the dipole direction is zero and maximum at the perpendicular direction). Namely, the original incident light is scattered to almost every direction. The strength of an oscillating electric field is given by

$$E = E_0 \cos 2\pi\omega t \qquad (2.16)$$

where E_0 is the vibrational amplitude and ω the frequency of the light. Considering the simplest case that the light scattered by a diatomic molecule. The molecule is polarized by the electric field of light.

$$P = \alpha E = \alpha E_0 \cos 2\pi\omega t \qquad (2.17)$$

where P is the induced dipole moment, α is the polarizability. Considering the molecule vibrates with the frequency ν, it leads to the nuclear displacement

$$q = q_0 \cos 2\pi\nu t \qquad (2.18)$$

where q_0 is the vibrational amplitude. For a small q_0, the polarizability changed with nuclear displacement can be written as Taylor expansion:

$$\alpha = \alpha_0 + \left(\frac{\partial\alpha}{\partial q}\right)_0 q + \cdots . \qquad (2.19)$$

where α_0, $\left(\frac{\partial\alpha}{\partial q}\right)_0$ are the polarizability and the derivate as displacement at the equilibrium position, respectively. From equation (2.17)–(2.19) the induced dipole moment

$$P = \alpha_0 E_0 \cos 2\pi\omega t + \frac{1}{2}\left(\frac{\partial\alpha}{\partial q}\right)_0 q_0 E_0 [\cos 2\pi(\omega + \nu)t + \cos 2\pi(\omega - \nu)t] . \quad (2.20)$$

The first term of equation (2.20) represents an oscillating dipole at frequency ω that contributes to the Rayleigh scattering. The second and third terms represent oscillating dipoles at frequency $\omega + \nu$ and $\omega - \nu$ which represent the anti-Stokes and Stokes Raman scattering, respectively.

For an oscillating dipole moment with amplitude μ_0 (dipole moment $P = P_0 \cos 2\pi\,\omega t$, where P_0, ω are oscillation amplitude and frequency, respectively), the radiation power of per solid angle is given by

$$\frac{dW}{d\Omega} = \frac{P_0^2 \omega^4}{32\pi^2 \epsilon_0} \sin\theta^2 \,, \qquad (2.21)$$

where ϵ_0 is the permittivity of vacuum, θ the radiation angle with respect to the dipole direction. By inserting the third term of equation (2.20) into equation (2.21), one obtains the radiation power of Stokes Raman process

$$\frac{dW}{d\Omega}_{Stokes} \propto \left(\frac{\partial\alpha}{\partial q}\right)_0^2 E_0^2 (\omega - \nu)^4 \,. \qquad (2.22)$$

Equation (2.22) tells the main feature of Raman scattering. Intensity of Raman scattering is proportional to the incident light intensity. In practice, a visible laser is usually used for Raman spectroscopy that the frequency $\omega \gg \nu$, so that the intensity is also proportional to frequency of incident laser ω.

2.3.2 Quantum description of Raman scattering

In a semi-classical quantum theory, light is treated as a classic electromagnetic field, while matter is considered in a quantum picture. The nth eigenstate (with wave function $\varphi_n^0(t)$) satisfies the time-dependent Schrödinger equation

$$i\hbar \frac{\partial \varphi_n^0(t)}{\partial t} = H_0\, \varphi_n^0(t) \,, \qquad (2.23)$$

where $\hbar$ is reduced Planck constant, H_0 is Hamitonian of the matter, $\varphi_n^0(t) = \varphi_n^0 e^{-iE_n t}$ is the wave function with eigenenergy of E_n. Interaction energy between the electromagnetic field and the matter is $-\boldsymbol{PE}$, where $\boldsymbol{P} = \sum_n e_n \boldsymbol{r}_n$ is the electric dipole operator, e_n and $\boldsymbol{r}_n$ are the charge and the position of the nth charge, respectively, $\boldsymbol{E}$ is the electric field of light. The interaction energy is a time-dependent perturbation that makes the Schrödinger equation change to

$$i\hbar\frac{\partial\varphi_n(t)}{\partial t} = (H_0 - \boldsymbol{PE})\varphi_n(t)\,. \qquad (2.24)$$

The perturbed time-dependent wave function

$$\varphi_n(t) = \sum_{k=0}^{\infty}\varphi_n^k(t)\,, \qquad (2.25)$$

$\varphi_n^k(t)$ is the kth order perturbed wave function.

The scattering of light is still assumed to originate from an oscillating dipole, but the dipole becomes to the transition dipole associated with state transition. In Raman scattering, the matter is scattered from the initial ith state to the final fth state, and the electric dipole moment is given by

$$P_{if} = \int \varphi_f(t)^*\boldsymbol{P}\varphi_i(t)d\boldsymbol{r}\,. \qquad (2.26)$$

Classical radiation associated with the dipole moment is $I_{if} \propto |P_{if}|^2$. In a first-order approximation and considering the electromagnetic field as uniform, the total intensity of the scattering light averaged over all orientations is given by

$$I_{if} = \frac{2^3\pi}{3^2c^4}I_0(w-v)^4\sum_{\rho,\sigma}\left|(\alpha_{\rho\sigma})_{if}\right|^2\,, \qquad (2.27)$$

with the polarizability tensor

$$(\alpha_{\rho\sigma})_{if} = \sum_r\left[\frac{(M_\rho)_{rf}(M_\sigma)_{ir}}{E_r - E_i - \hbar w} + \frac{(M_\rho)_{ir}(M_\sigma)_{rf}}{E_r - E_f + \hbar w}\right]. \qquad (2.28)$$

where c is the velocity of light, I_0 and w are the intensity and the frequency of the incident light, respectively, E_i, E_r, and E_f are the energy of initial, intermediate and final states of the matter, respectively, $v = \frac{E_f - E_i}{\hbar}$ is the frequency shift of scattered light, $\rho = x, y, z$ and $\sigma = x, y, z$ are the coordinate system of matter, $(M_\rho)_{rf}$, $(M_\sigma)_{ir}$, $(M_\rho)_{ir}$, $(M_\sigma)_{rf}$ are the transition dipoles along a specific directions given out by $(M_k)_{mn} = \int \varphi_m^0(t)^*\boldsymbol{e}r_k\varphi_n^0(t)d\boldsymbol{r}$. In Raman scattering by molecules, the sum in equation (2.28) goes over all vibronic states of the molecules.

In the discussion of a semi-classical treatment above, the relation between the transition dipole and scattering is hypothesized. An exact comprehension of Raman scattering should be

considered in a pure quantum theory. Both the radiation and matter are quantized. The problem can still be solved with the perturbation theory and the same result was obtained as equation (2.27) and (2.28) [93].

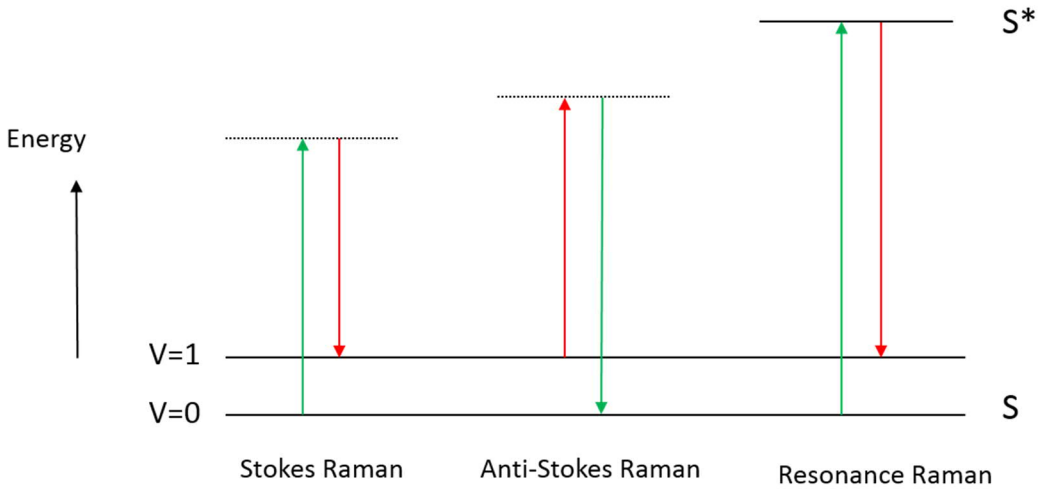

Figure 2.4. energy diagram of Raman scattering.

In the perturbation theory, Raman scattering is a second-order process, in which an incident photon is annihilated and a new photon with different energy is created. **Figure 2.4** illustrates the energy diagram of Raman scattering. The dashed lines are virtual levels and the solid lines are quantum states of the matter (or molecule). In the Stokes Raman scattering, the molecule is originally in ground and an incident photon is absorbed, yielding a photon with a smaller energy, while the molecule is vibrationally excited. On the other hand, the molecule is originally in vibrational excited state in the anti-Stokes Raman scattering, an incident photon is absorbed and a photon with a larger energy is reemitted, while that the molecule returns to the ground state. In non-resonance Raman scattering, the photon absorption and reemission take place through the virtual states, while in resonance Raman scattering a real excited electronic state is involved. Under the resonance condition $E_r - E_i = \hbar w$, the intensity has maximum from equation (2.27) and (2.28).

2.3.3 Enhanced Raman spectroscopy

Since Raman cross section of molecules is extremely small (10^{-31} ~10^{-28} cm^2), enhancement of Raman scattering is necessary in order to measure small amount molecules. One possible enhancement mechanism is the chemical enhancement. As shown above, the Raman cross

section becomes extremely large under the resonance condition. In the resonance Raman measurement, a laser should be chosen to match its photon energy close to the electronic transition of the target molecule, then the cross section can be enhanced as much as five orders [94]. There is another mechanism named physical enhancement in SERS, which occurs through enhancement of a local electric field by surface plasmon excitation. This has been considered as the mainly enhancement mechanism in SERS.

Matter is polarized under an extra electric field. Considering a simple case of metallic spheres that can be polarized by a uniform external field E_{ext}, the polarization leads to an induced electric field E_{ind} originating from the induced charge redistribution. The resulting total electric field is $E_{fin} = E_{ext} + E_{ind}$. For a metallic sphere as show in **Figure 2.5a**, the E_{fin} is much larger than E_{ext} at pole positions (marked with a red ellipse) due to the denser induced charge. In the gap between two spheres, the electric field becomes even larger because the induced charge of both spheres contributes to the E_{ind} (**Figure 2.5b**). The collective oscillation of electrons has a resonant frequency and quantum of this oscillation is named plasmon. When a metallic nanoparticle or nanostructure is illuminated, the conduction electrons are oscillated by the optical field and surface plasmon can be excited. It enhances the localized electric field and the enhancement factor is defined as

$$g = \frac{|E_{fin}|}{|E_{ext}|}. \qquad (2.29)$$

Common plasmonic materials used in plasmonics are Au and Ag nanoparticles, which have plasmon resonances in the visible range. Ag nanoparticles have advantage of a large field enhancement due to its smaller dephasing time of SPP. For a metal sphere much smaller than the wavelength of light, the collective oscillation of the electrons in the nanoparticle can be regarded as an oscillating dipole.

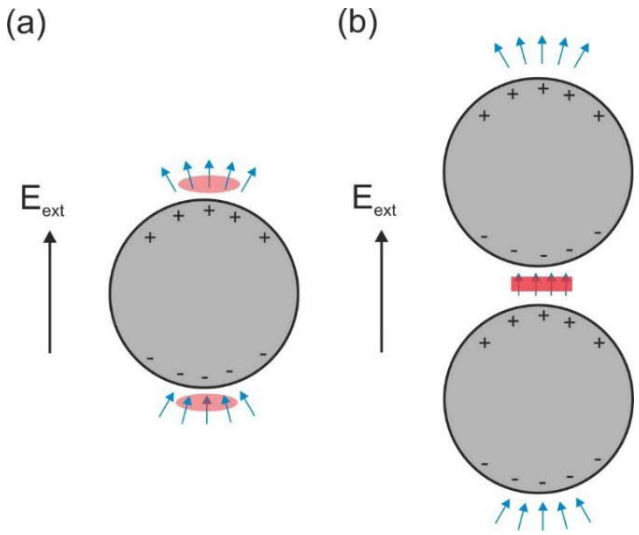

Figure 2.5. (a) Schematic of induced electric field of a metal sphere. (b) Schematic of induced electric field of metal sphere dimer. Positions where electric field strongly enhanced are marked by red shapes.

Molecules in the vicinity of a nanoparticle surface feel the enhanced electric field by g^2. The oscillating dipoles of Raman scattering (the second and third terms in equation (2.20)) also interact with the nanoparticle, amplifying the emission. Therefore, the total enhancement of Raman intensity is proportional to g^4 [95]. There are numerical simulations for Raman enhancement of single and dimer Ag nanospheres (60 nm) under resonance conditions [95] with a gap size of 2 nm in the dimer. The Raman enhancement at the hot spots (nanoscale regions with a strongly enhanced local electromagnetic field, which are indicated by red- parts in **Figure 2.5**) are ~10^3 and ~10^9 for single and dimer sphere, respectively. Owing to the large field enhancement, nanocavity plays a crucial role in enhanced Raman spectroscopy and many other plasmon-driven processes.

The spatial resolution of conventional optical microscopy is limited to be hundreds of nanometers for visible light due to the diffraction limit. TERS is invented in 2000 [15, 96, 97, 98], which can overcome the conventional diffraction limit. It has a similar enhancement mechanism as SERS and a critical structure in TERS is also a plasmonic nanocavity that consists of the plasmonic SPM tip and the surface, namely the SPM junction. The SPM junction is illuminated by a focused laser during TERS measurement to yield the enhanced local field inside the junction. Enhanced Raman signal from the junction is collected at each point as the tip scans over the surface. The spatial resolution is mainly determined by the tip size that can

be even sub-nanometer as mentioned in the introduction. We performed the TERS measurement using our home-designed LT-photon-SPM setup that is introduced in the section 2.4.

2.3.4 Selection rule of TERS

The classical description of Raman scattering in equation (2.22) derives a strict selection rule for Raman scattering: $\left(\frac{\partial \alpha}{\partial q}\right)_0 \neq 0$. According to this condition, Raman active modes of simple molecules can be easily determined. For example, a stretching mode of diatomic molecules is Raman active, bending mode of a linear ABA style molecule is Raman inactive [99].

As show in equation (2.24) the light-matter interaction term is $-\boldsymbol{PE}$. In the conventional Raman scattering, the light wavelength is much larger than the size of a scattering object like a molecule, thus $\boldsymbol{E}$ is simplified as a uniform field in space. The optical transition matrix is $\boldsymbol{E}\int \varphi_f(t)^* \boldsymbol{P} \varphi_i(t) d\boldsymbol{r}$. The polarizability tensor in equation (2.28) is obtained by this simplification. Considering a locally confined field within the junction in TERS, the size of the field becomes comparable to a molecule. In this situation, $\boldsymbol{E}$ cannot be treated as a uniform field anymore and a field gradient will play a role. Then the $\boldsymbol{E}$ should be included in the integration of optical transition matrix $\int \varphi_f(t)^* \boldsymbol{PE} \varphi_i(t) d\boldsymbol{r}$, this results in differently perturbed time-dependent wave function in equation (2.25) and final polarizability tensor. Due to the field confinement, the silent modes in conventional Raman scattering may become active in TERS [100, 101, 102, 103]. Field perpendicular to the surface direction is strongly enhanced in the junction, so that the TERS signals of vibrations perpendicular to the surface can be selectively enhanced [48, 104], which is also the case in our observation as discussed in Chapter 5.

2.4 Photon SPM

2.4.1 Introduction

Photon-SPM is a promising approach to investigate light–matter interactions at nanoscale and many impressive experiments have been demonstrated as discussed in the introduction. Because there was no standard commercial photon-SPM setup at the time I started my PhD project, we have designed and built a customized LT-photon-SPM in cooperation with

UNISOKU, Japan. In this chapter, technical challenges and several strategies combine SPM with optics are discussed.

2.4.2 Technical challenges of photon-SPM

Since optical signal from the SPM junction is in general very weak, a high numerical aperture (NA) optics for photon collection is required. But, at the same time, a convenient alignment procedure of the optics should also be considered while keeping the performance of low-temperature SPM. A couple of instrumental designs that fulfill these requirements have been conceived. Several construction strategies of photon-SPM are explored and introduced in next section, configuration details of our setup is also described latter.

Beam alignment is the most crucial procedure in photon-SPM and the beam needs to be accurately focused on the SPM junction. The spot size of a focused beam is a few micrometers and the SPM junction is at the size of nanometers, which makes the focusing be difficult. In addition, it becomes an even more difficult task to perform the alignment in an UHV chamber, especially for the photon-SPM which is equipped with a parabolic or ellipsoidal mirror compared to lens systems. Nevertheless, we have chosen a parabolic mirror in our setup to obtain better optical performance and optimized our alignment procedure that worked properly. We also found that the plasmon assisted tunneling process can be nicely used to check the final alignment quality (Chapter 3).

Even the UHV chamber would aggravate the difficulty of beam alignment, but UHV condition is necessary for many measurements. One important application of the photon-SPM is TERS. To perform TERS measurements at the single-molecule level, a well-defined environment is necessary and contamination of the tip would also make a problem. A tip apex should be reactive due to the high reactivity of metal cluster, which makes it easily contaminated in ambient. An UHV environment provides atomically clean systems to avoid the contaminations. The first attempt of UHV-TERS was published in 2007 by Pettinger group in the Fritz-Haber Institute [105]. They obtained TERS signal for single dye molecule with spatial resolution of 15 nm and also simultaneously recorded the STM image [105]. Up to now, only several groups have reported UHV-TERS measurements [106, 107, 48, 108] and it is still a technical challenge to construct the proper setup for TERS experiments under UHV conditions.

Stability is also a crucial problem for TERS measurements particularly at room temperature. Highly stable condition is also required in SPM measurements in which atomic scale change in the junction would induce a huge disturbance. Stability of the junction becomes even worse under illumination of focused laser beam in TERS measurements. The signal shows fluctuations as reported in many TERS experiments at room temperature [109, 110, 111]. Therefore, low temperature is required to guarantee good measurement condition, our setup can be cooled by liquid N_2 (~80 K) or He (~5 K).

Moreover, laser source is challenged for some optic measurements. The chemical resonance situation is needed to be satisfied in TERS measurements, which requires the laser photon energy matches with the optic transitions of measured sample. This requirement is somewhat challenged that a broad range wavelength tunable laser source is expected to measuring different samples.

2.4.3 Strategy of SPM combined with optics

Strategies of a photon-SPM design can be mainly classified into three types according to the cofiguration of optics as schematically shown in **Figure 2.6**. **Figure 2.6a** is the combination of optical fiber or fiber bundle [112, 113], in which an optical fiber is placed close to the SPM junction. A reasonable NA can be obtained with this approach. However, a drawback is difficulties in optical alignment and one should also take care a lot the transfer of sample in UHV not to collide with the fiber. In practice, only a low photon collection efficiency was obtained due to the inaccuracies in the alignment of the fiber [113]. A lens system (**Figure 2.6b**) can attain a suitable NA (~0.5 [108, 48]) that is enough to collect relatively strong optical signal from the junction. It is also much easier to align the optics than the fiber or parabolic/ellipsoidal mirror system. This setup has been examined in several different groups [26, 27, 114, 115,39] and is currently the most common strategy. **Figure 2.6c** shows a combination with a parabolic or ellipsoidal mirror. A large NA can be obtained with the parabolic/ellipsoidal mirror setup [116, 105], which can also avoid spherical and chromatic aberration. Therefore, combination with the mirror setup is the ideal strategy in theory. But it is a challenging task to do alignment that the photon collection efficiency is very sensitive to the deviation from the perfect aligning. In our test measurements, the Raman signal totally disappeared even the parabolic mirror axis only tilted ~0.05° from the incident laser beam.

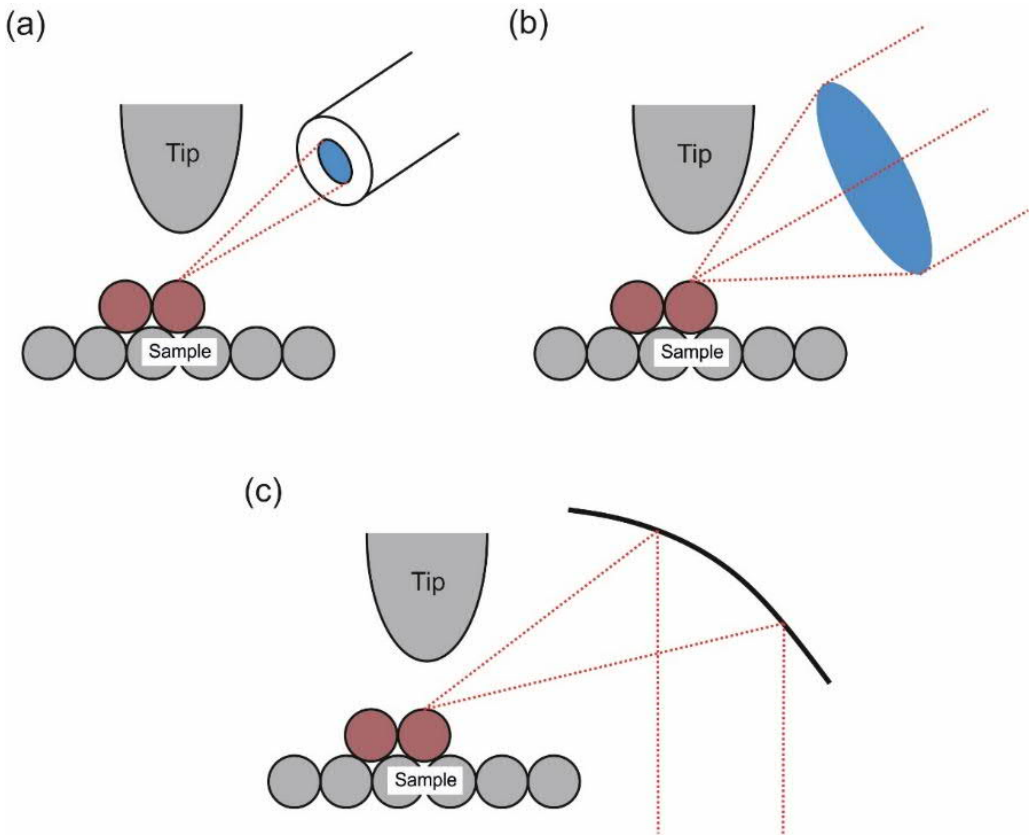

Figure 2.6. Schematic for three different strategies of SPM combined with optical setup: (a) optical fiber or fiber bundle, (b) lens, (c) parabolic or ellipsoidal mirror.

To attain a better optical performance, we adopted the strategy combined with a parabolic mirror as schematically show in **Figure 2.7**. We mount a parabolic mirror on the SPM stage that can be cooled down. The STM tip is fixed in a hole on the tip holder by a clamping mechanism. To ensure that the focus spot is always on the junction during the measurement, the tip is fixed and scanning is performed by moving the sample. A collimated beam goes through the hole of the tip holder (marked in **Figure 2.7**) and incidents to the parabolic mirror to focus on the SPM junction. Photon emitted from the junction is also collected by the parabolic mirror as a collimated beam. The position of the parabolic mirror is controlled precisely by piezo motors. It has five-axis movement (three linear and two rotational motions) as marked by arrows in **Figure 2.7**. All the *in-situ* optical components are built on the SPM stage which can be cooled down by the cryostat.

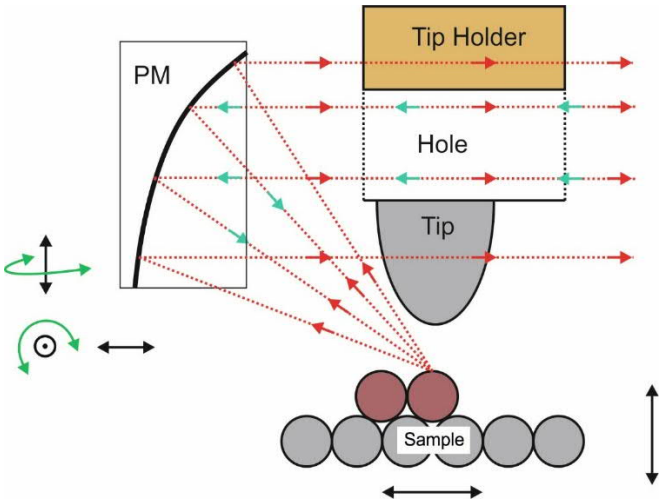

Figure 2.7. Schematic of our optical SPM. Degree of freedom of the sample and parabolic mirror is marked by arrows.

2.4.4 Customized optical SPM system

All sample preparation and characterization are performed under UHV conditions. The UHV system consists of the preparation and measurement chambers as shown in **Figure 2.8**. Two chambers are separated by a gate valve to avoid the contamination of measurement chamber from sample preparation. A small load-lock is connected with the preparation chamber, which allows the transfer in and out samples and tips to the ambient without braking the vacuum of the preparation and measurement chambers. All samples and tips are transfer with transfer rods and can be stored in both preparation and measurement chambers. A mechanical pumps (turbo pump and membrane pump) are connected with the load-lock. An isolated chamber for the ZnO preparation can be connected with the preparation chamber. Samples can be annealed on the manipulator stage in the preparation chamber. It has two heating modes, direct current and electron emission. All the heating are performed with the electron emission mode in this thesis. The sample temperature is measured by a pyrometer outside the chamber. A cryostat is located at the bottom of measurement chamber that can keep the SPM stage at ~80 K for about 5 days after filling (liquid nitrogen). A small reservoir of the cryogen is located under the SPM stage. The SPM stage is protected by three shields as shown in the right enlarged image of **Figure 2.8**. Liquid nitrogen (or liquid helium) in the cryostat is pumped up into the small reservoir. Ion pumps (black cuboids in **Figure 2.8**) are connected under the measurement and preparation chamber, which keep a base pressure ~10^{-10} mbar for both chambers.

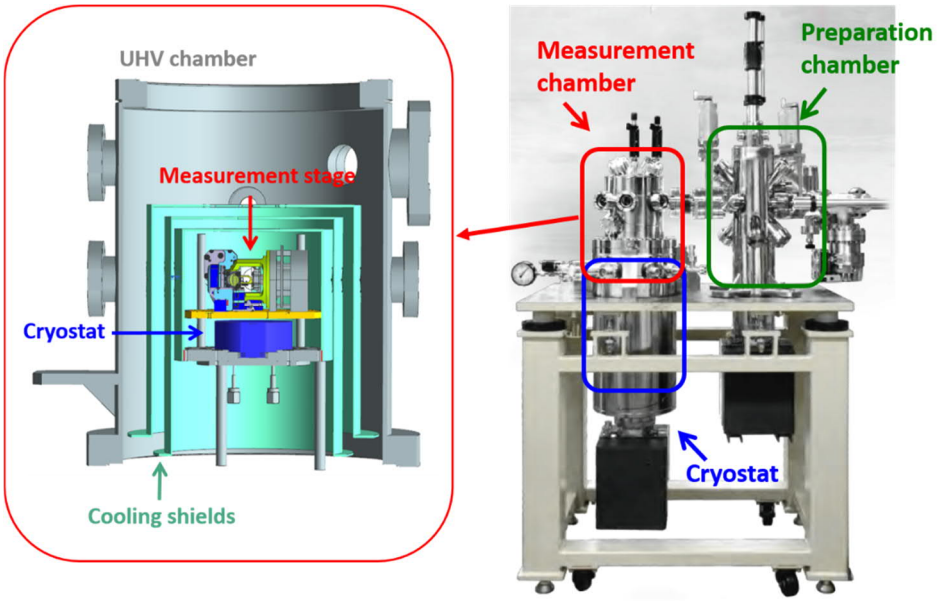

Figure 2.8. Low-temperature SPM system (USM-1400, UNISOKU). Left figure is the drawing of cross sectional view of the SPM unit in the measurement chamber.

Figure 2.9 is a picture of the SPM stage from the top. The main components are labeled, which are the piezo motors with the SPM scan piezo tube (label 1), the piezo motors for parabolic mirror (label 3), the piezo motors for lens movement (label 7). To collect the refection beam, a lens (label 6) is also added except the parabolic mirror. It is fixed on the combined piezo motor system has three dimensional linear movement, which allows to focus the lens on the SPM junction. A collimated laser beam can be focused either through the parabolic mirror and collected by lens after reflected by the sample, or vice versa, as schematically shown by the red dashed line. Many copper wires that are thermal conductive are added to improving the cooling efficiency. The SPM stage is vibrational isolated from the chamber by spring suspending (label 8). Focus length of the parabolic mirror is 8.85 mm and the NA for the collection is 0.61. Focus length of the lens is 3 cm and the NA is ~ 0.2.

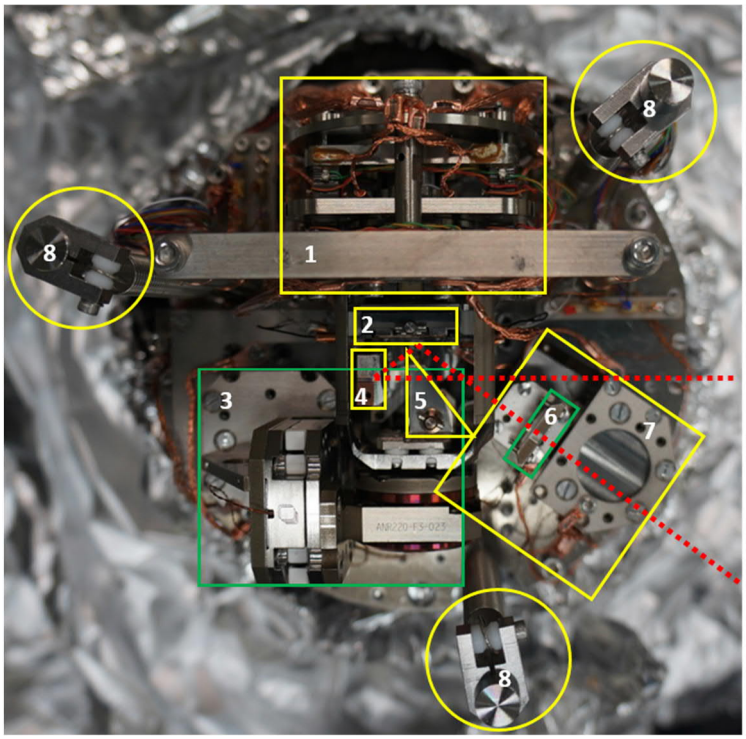

Figure 2.9. Top view of the SPM stage. The main parts are labeled 1: scan piezo, 2: sample, 3: piezo motor for parabolic mirror, 4: parabolic mirror, 5: tip holder, 6: lens, 7: piezo motor for lens, 8: suspension spring. The red dashed line is the laser beam path.

Figure 2.10 displays a side view of the SPM stage from the perspective of the incoming/outgoing beam direction to the parabolic mirror (projection along x-axis). As mentioned above the tip holder has a track-shaped hole in order to pass through the incoming beam. A beam waist diameter up to ~2.5 mm is available to focus with the parabolic mirror. The smallest focused spot is estimated to be diameter of ~3 μm at a laser wavelength of ~600 nm according to the formula

$$D = \frac{4\lambda f}{\pi d}, \qquad (2.30)$$

where λ is the wavelength, f the focus length of the parabolic mirror, d the incident beam diameter. Since the outcome collection beam would partially blocked by the tip holder, the net NA is smaller than 0.61. The reflection and diffraction image from a sample surface and the SPM junction can be observed through the lens, which can be used for the beam alignment. It is also possible to focus or collect the light with the lens.

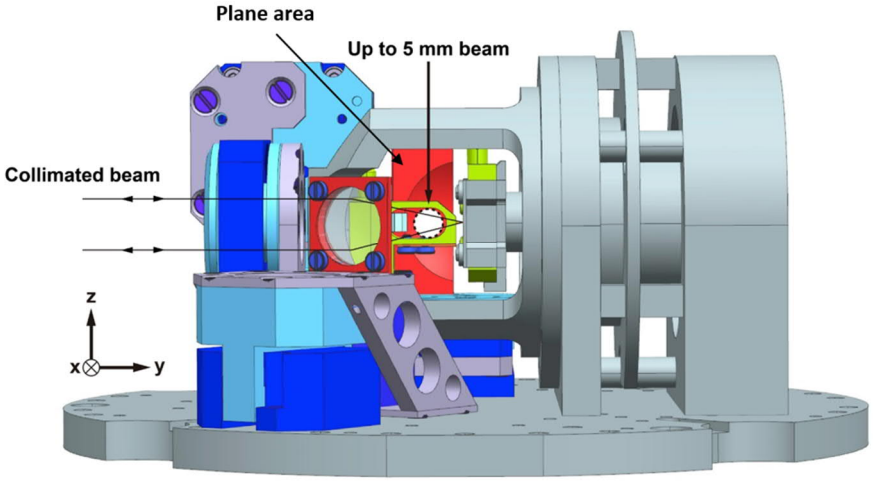

Figure 2.10. Drawing of the side view of the SPM stage.

2.4.5 Optical alignment

Accurate alignment is essential for any optical measurement. A major challenge is how to align the incoming collimated beam to the parabolic in a reproducible manner and in a reasonable timescale. The axis of the incoming beam has to be exactly parallel to the axis of the parabolic mirror. The plane area (indicated in **Figure 2.10**) of the parabolic mirror is made perpendicular to the axis of parabolic mirror with very high accuracy. During alignment the incoming beam is first extended on the plane area and the backward reflection is used for the tilt correction of the parabolic mirror. The beam is translated to the parabolic area by linear moving stage outside.

As mentioned before, it is not a trivial task to focus a several μm focus spot on the SPM junction in a highly-accurate and reproducible manner. For optical alignment, it is important to have a good reference and indicator to guide or judge the focus quality. In our setup, reflection (shadow) pattern observed through the lens and visualization of the SPM junction can be used to guide the movement of the parabolic mirror. STM-induced luminescence on a clean metal surface was used to judge the quality of alignment [117]. Surface plasmon in the STM junction can be excited by inelastic electron tunneling at a bias voltage larger than 2 V. **Figure 2.10** is an image of the STM junction with luminescence. A bright spot from the junction can be observed with a CCD camera outside the UHV chamber when a good alignment is achieved. In addition, the plasmon-assisted tunneling process (discussed in chapter 4) can also be used to

verify the alignment quality. This phenomenon can occur only when the incident beam is precisely focused on the junction.

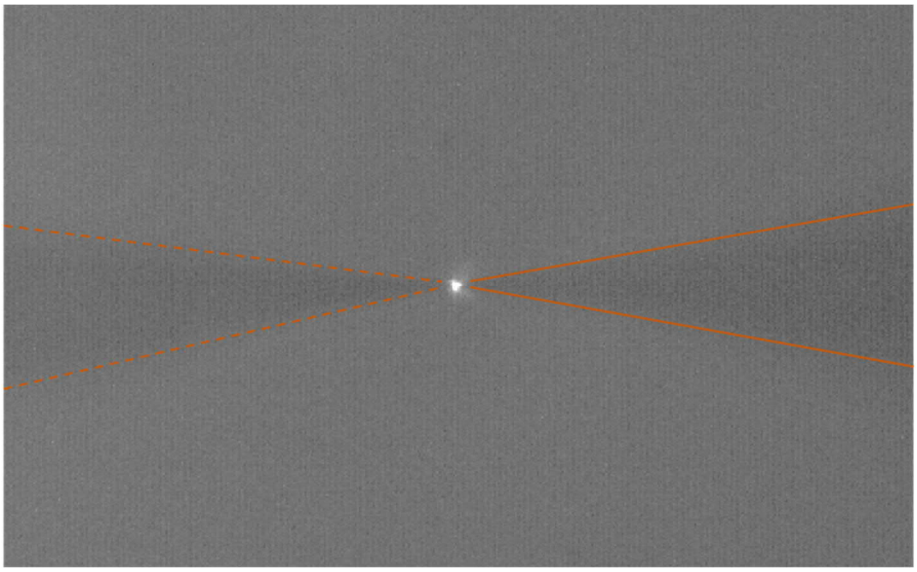

Figure 2.10. Image on a CCD camera of the STM junction with electron luminescence (the bright point). The junction is Au tip-Au(111) surface. Bias V = 2.5 V, current I = 50 nA. The right side triangle shape shadow (emphasized by the solid orange lines) is the Au tip and the left one (emphasized by the dashed orange lines) is image of the tip reflected from the Au surface.

2.5 Preparation of ultra-thin ZnO layers on Ag(111)

We grew ZnO layers epitaxially on a Ag(111) surface. The Ag(111) surface was cleaned by repeated cycles of argon ion sputtering and annealing up to 670 K. The ZnO layers were prepared in a separated chamber (**Figure 2.11**) with the reactive deposition method [118]. The base pressure of the chamber was below 5×10^{-10} mbar. Zn was deposited onto a room temperature Ag(111) surface in the presence of O_2 ambient and ZnO layers was obtained by post-annealing at 670 K under UHV condition. A Zn rod (99.9997% purity, from Alfa Aesar) was heated in a Knudsen cell at ~490 K and pressure of O_2 was keep at 1×10^{-5} mbar during the deposition. This relatively high O_2 partial pressure was used to avoid the possible alloying between Zn and Ag. The heating temperature of Zn was measured by a thermocouple at the

bottom of the Knudsen cell. The distance between the Zn source and Ag(111) surface was ~15 cm.

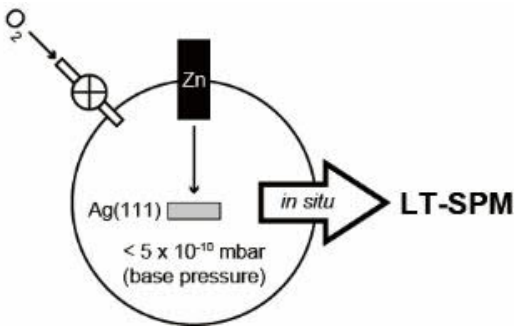

Figure 2.11. Schematic of ZnO preparation chamber.

3 Plasmon assisted electron tunneling

3.1 Introduction

Plasmon-driven processes offer diverse applications in nanoscience and nanotechnology and have attracted increasing attention [119]. Plasmonic nanocavities can confine light into nanometric volumes and enhance the electric field strongly. However, it is still challenging to understand the near-field properties and near-field-driven processes in such nanocavities. When the size of the nanocavity is at several nanometers order or even smaller, quantum mechanical effects such as quantum tunneling, nonlocal screening play important roles to determine the plasmonic properties [120]. The size and morphology of a nanocavity have to be accurately determined that sophisticated experiments under well-define conditions are necessary to elucidate the underlying physics. A theoretical framework exceed the classic description that includes quantum effects is necessary [121].

It is also of fundamental importance to realize the ultrasensitive spectroscopy at the nanoscale down to the single-molecule level [122, 48, 123, 124], and even with ultrahigh temporal resolution [125, 126, 127, 128, 129, 130, 131, 132]. As discussed in the introduction, photon-SPM can observe nanoscale structures and their plasmon response simultaneously. It also has the advantage to well define the nanocavity. It allows to control the nanoscale gap distance in the junction with accuracy of sub-angstrom and can also provide the morphology information of the sample. The photon-SPM provides a unique opportunity to examine plasmon-induced processes in nanocavities [133]. Resonant electron transfer in plasmonic nanocavities, which relates to interplay between plasmon response and electron transfer, is important in various applications such as photovoltaics, photocatalysis, and fast electronics [134]. There are previous reports about light-assisted electron tunneling into a molecular resonance in an STM junction [135, 136], and this process could be enhanced by the plasmon excitation.

In this chapter, plasmon-assisted resonant tunneling in the STM junction is described. Electron tunneling from the tip to FERs over a Ag(111) surface is induced by CW laser excitation. The process results in peak shifts in the FER spectrum. The experiments with different tip materials, different tip geometries, and different laser polarizations clearly indicate that the plasmon excitation play a crucial role.

3.2 FER spectra under illumination

Figure 3.1 shows the FER spectra measured over the Ag(111) surface with and without illumination of 633 nm ($h\nu$=1.96 eV). The peaks correspond to the FERs that have been studied previously without illumination [137,138]. The measured FER peaks are largely shifted to lower energies under illumination. The shift of the first FER peak is nearly equal to the incident photon energy. We use n and n' (=1, 2, 3…) to indicate the FER peaks measured without and with illumination, respectively. The spectra were measured in the constant current mode, which allows a wide voltage range measuring but results in the continuous tip–surface displacement (dash curves in **Figure 4.1a**). **Figure 4.1b** shows the FER spectra measured under different power illumination. The illuminated power density varies from 0 to 0.528 mW/μm^2. The n'=1 peak at 2.2 V grows up as the incident power increases, while the n=1 peak at 4.2 V diminished.

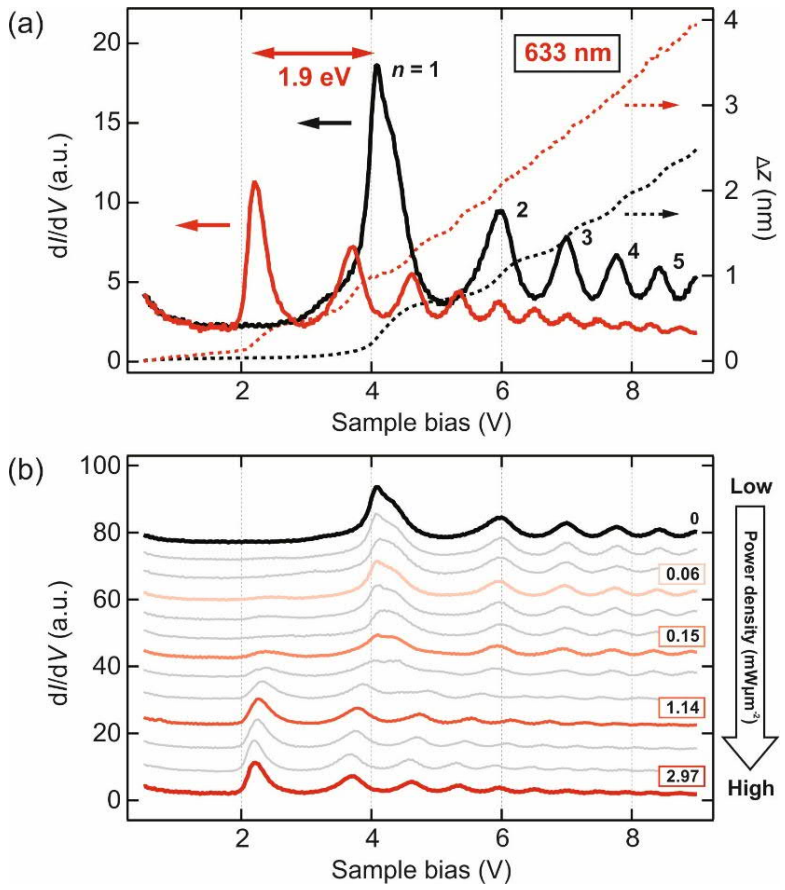

Figure 3.1. (a) FER spectra measured over the Ag(111) surface with and without illumination. The solid black curve is the spectrum without illumination and the

solid red curve is under illumination of 633 nm ($h\nu$ = 1.96 eV). The power density of illumination is 0.528 mW/μm^2. The spectra were measured in the constant current mode at 0.1nA and the tip-surface displacement (dashed curves, right axis) was also recorded simultaneously. (b) FER spectra measured under different power illumination. The spectra are offset vertically for clarity.

Figures 3.2a and **b** are the FER spectra measured with and without illumination of 446 nm ($h\nu$=2.8 eV) and 532 nm ($h\nu$=2.3 eV), respectively. As shown in **Figure 3.2a**, the n=1 peak downshifts by ~2.8 V under the 446 nm illumination.

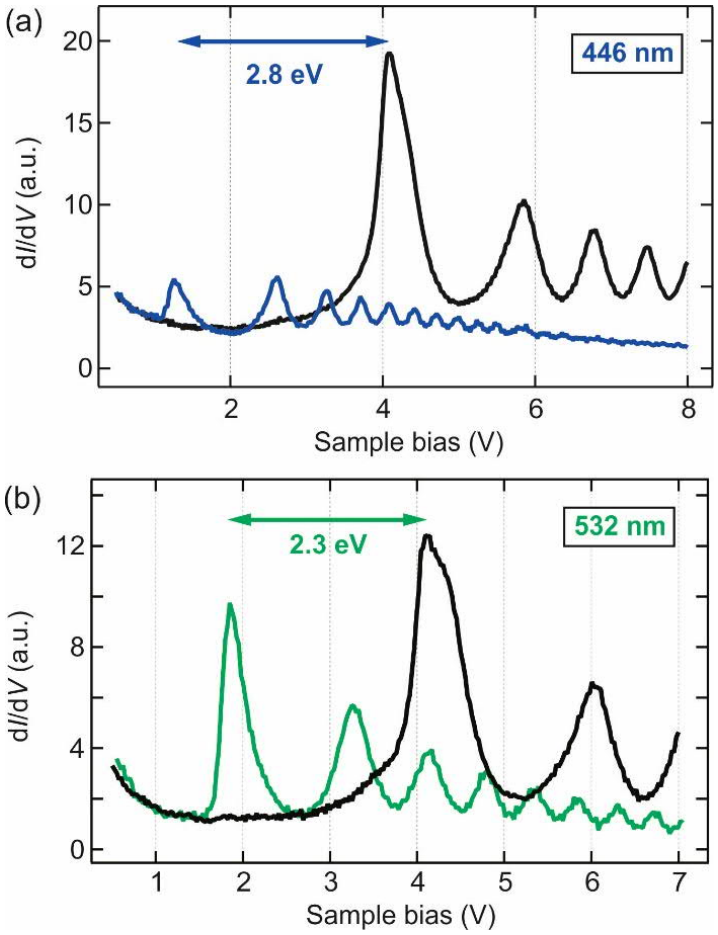

Figure 3.2. FER spectra measured over Ag(111) surface with and without illumination. (a) The black curve is without illumination and the blue one is under illumination of 446 nm ($h\nu$ = 2.8 eV). (b) The black one is without illumination and the green one is under illumination of 532 nm ($h\nu$ = 2.3 eV).

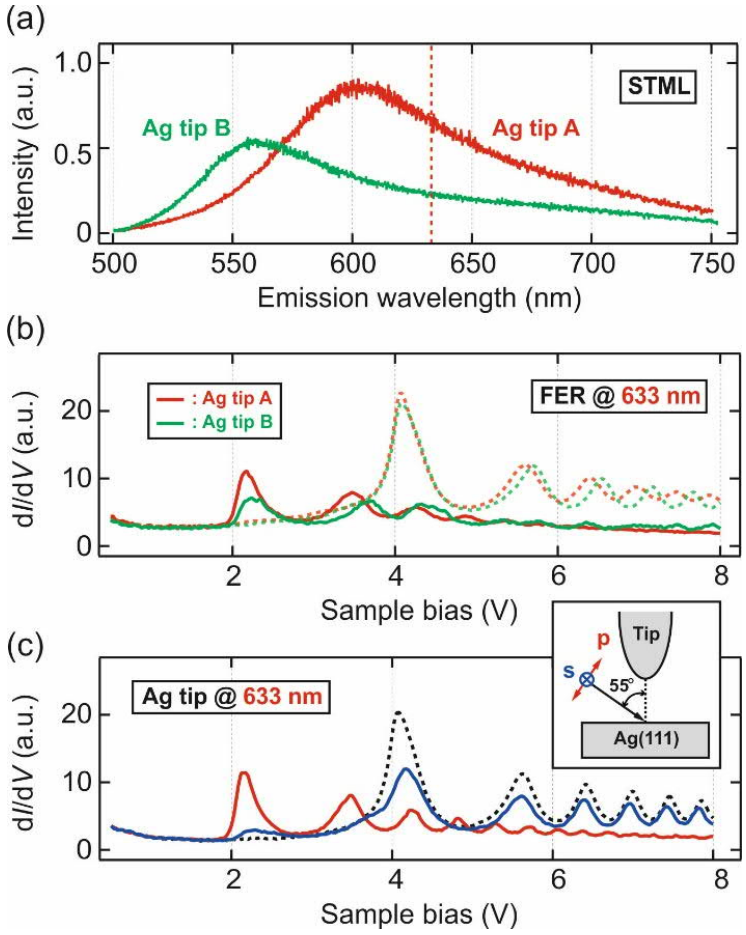

Figure 3.3. (a) STML spectra measured under two different tip conditions. The red vertical line marks the wavelength of 633 nm. (b) FER spectra measured over Ag(111) surface with and without illumination under the two tip conditions in (a). The spectra were measured under 633 nm illumination and the power density of illumination is 0.188 mW/μm^2. (c) FER spectra measured over Ag(111) under 633 nm illumination of s- and p-polarized beam. The power density is 0.089 mW/μm^2.

It was found that the plasmonic properties of the STM junction correlate with the FER changes under illumination. **Figure 3.3a** shows STML spectra of the Ag tip–Ag(111) junction under two different tip conditions. The Ag tip was poked into the clean Ag(111) surface to modify the tip condition. The FER spectra measured under the two tip conditions are shown in **Figure 3.3b**, which includes the illuminated by 633 nm and non-illuminated case. The plasmonic property of STM junction is sensitive to the tip condition [139]. At the illumination wavelength of 633 nm, the STML intensity of tip A is stronger than tip B. The FER spectrum also shows larger changes under illumination measured with tip A, as shown in **Figure 3.3b**

that the intensity of *n*'=1 peak is larger. It was also found that polarization of the incident beam strongly affects the FER spectra. The illumination-induced effect is much stronger for p-polarized beam. As shown in **Figure 3.3c**, the intensity of *n*'=1 peak of illuminated with p-polarized beam is much larger than the s-polarized one. In contrary to the Ag tip, the plasmon-induced process is absent in the FER spectrum measured with an Au tip under 532 nm illumination as shown in **Figure 3.4**. This can be explained by a weak plasmon coupling of the Au tip at 532 nm excitation. The above results clearly indicate that the plasmon excitation in the junction governs the observed change of the FER spectra under illumination.

Size of the focus spot is estimated to be a few μm that is much larger than the very tip apex. Therefore, the excitation of the surface plasmon is not localized only in the junction and SPP launched on the tip shaft may also contribute to the field enhancement. The SPP can focus to the tip apex to generate a giant local field [140, 141]. The threshold power density at which the plasmon-assisted tunneling occurs is higher for the higher-order FERs as can be seen in **Figure 3.1b**. This could be explained by the fact that the tip–surface distance is continuously increased during the FER measurement, which becomes larger that the voltage of the higher-order peaks. This results in a wider barrier for the electron transfer and also reduced field enhancement.

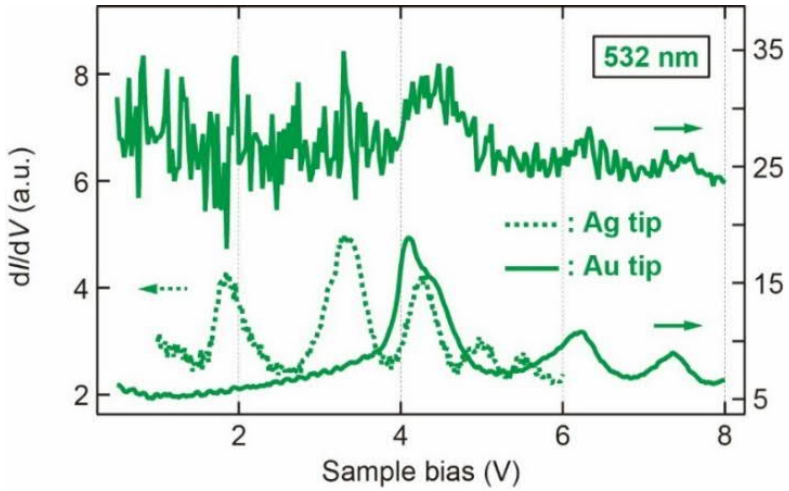

Figure 3.4. FER spectra measured over an Au tip-Ag(111) junction with 532 nm illumination (solid curves). The top spectrum is recorded at an incident power density of 0.892 mW/μm^2 and the bottom one is 0.1 mW/μm^2. The dashed curve is FER spectrum measured with Ag tip under illumination power density of 0.1 mW/μm^2.

It is straightforward to assign the *n*'=1 peak to the downshift of *n*=1 peak because the energy difference is equal to the incident photon energy. We assigned the higher-order peaks by measuring the conductance map in which the FER intensity is recorded at a specific bias voltage with and without illumination. The measurement was performed with an Au tip under illumination at 633 nm. **Figure 3.5a** is the single-point FER spectra measured over clean Ag(111). Local structure of defects of the surface modulate the local potential that would modify the FER [142, 143, 144, 145]. **Figure 3.5b** shows the measurement area that includes a small island (defect). The conductance maps at the bias voltage of the *n*=2, 3, 4 FER peaks without illumination are displayed in **Figures 3.5c**, **d**, **e**. The corresponding peaks are marked with c, d, e in **Figure 3.5a**. The unique features in the conductance map are observed for each peak. Although the geometry of the nano-structure determines the interference pattern [145, 146], a quantitative analysis is not possible due to the ill-defined structure of the island. Conductance maps of *n*= 2, 3, 4 FER peaks measured under illumination are shown in **Figure 3.5f**, **g**, **h**. The corresponding peaks are also marked with f, g, h in **Figure 3.5a**, respectively. The observed interference patterns of f, g, h are very similar to that of c, d, e. Therefore, it can be concluded that the peaks in the FER spectra with illumination are shifted from the original one without illumination.

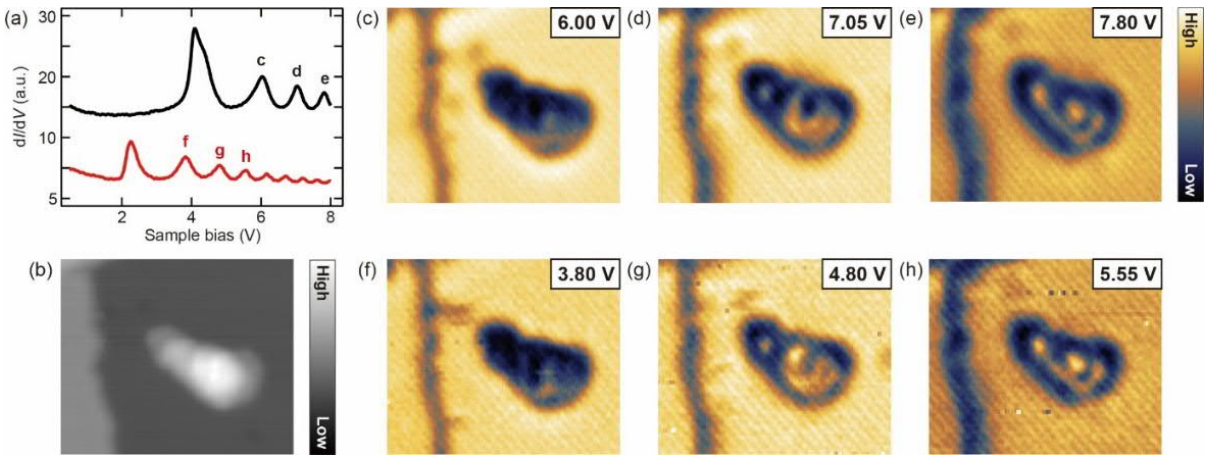

Figure 3.5. (a) FER spectra measured over the Ag(111) surface at 78 K with and without illumination. The laser wavelength is 633 nm and the power density is 0.237 mW/μm^2. The spectrum without illumination is vertically offset for clarity. (b) STM image of the measurement area with a small island (defect) and a single

atomic step on the surface. (c)-(e) FER mapping at the peak c, d, e indicated in (a). (f)-(h) FER mapping at the peak f, g, h indicated in (a).

3.3 Plasmon assisted tunneling

The schematic energy diagram of the STM junction is shown in **Figure 3.6**, which also depicts the junction potential and the electron wave functions. Here we consider a single particle picture using a simple one-dimensional model [147]. The junction potential is determined by the image potential and the applied bias between the tip and the surface. FERs are the standing wave states of electrons in front of the surface. During the measurement without illumination, electrons tunnel from the tip to the FER directly when the bias voltage matches the resonance levels, resulting in the peaks in the FER spectra. The plasmon-assisted transfer process becomes possible under illumination that electrons at the Fermi level of the tip can be excited. The electrons transfer from the tip to FER when the bias is $V_{n'}$=1,2,3… under illumination.

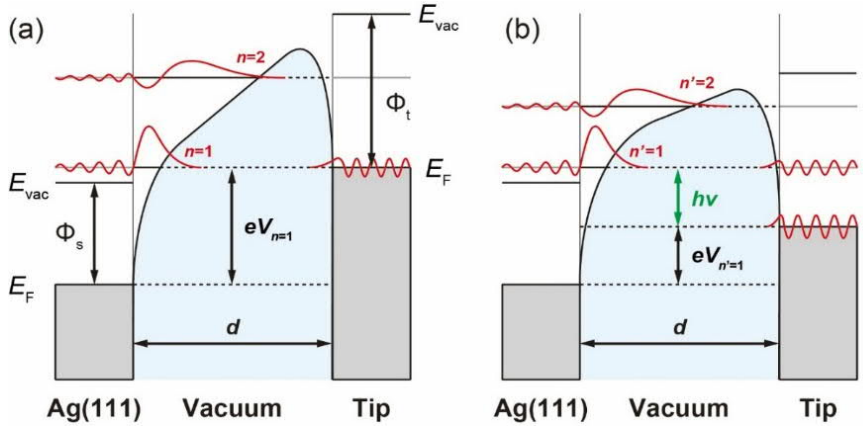

Figure 3.6. (a) and (b) Schematic energy diagram of the FER measurement without and with illumination, respectively. The blue shaded area is the potential in the vacuum gap. E_f is Fermi level, Evac is vacuum level, $\Phi_s(t)$ is work function of the surface (tip), V_s is sample bias, d is gap distance. n is index of the FERs, red curves are the schematic wave functions, hv is incident photon energy.

The coexistent of direct tunneling and plasmon-assisted tunneling process was also observed at intermediate incident power densities (e.g. 0.006 mW/μm^2) in **Figure 3.1b**, in

which both n=1 and n'=1 peaks appear in the FER spectrum. However, the direct tunneling process becomes negligible under high fluence because the plasmon-assisted process makes the tip–surface distance larger, which suppresses the normal STM tunneling from the Fermi level of the tip. For example, the distance difference reaches ~1.5 nm in the measurement in **Figure 3.1b**. The relative contribution from the direct tunneling and plasmon-assisted process can be tuned by varying the tip–surface distance. **Figure 3.7** shows the FER spectra measured under 532 nm illumination with an Ag tip at different tip-surface distance. The distance is controlled by the set current which is indicated in the figure. The peaks of $n' > 2$ show a blue-shift as the tip-surface distance decreases. The n=1 peak is discernible at small tip–surface distance with a set current above 20 nA.

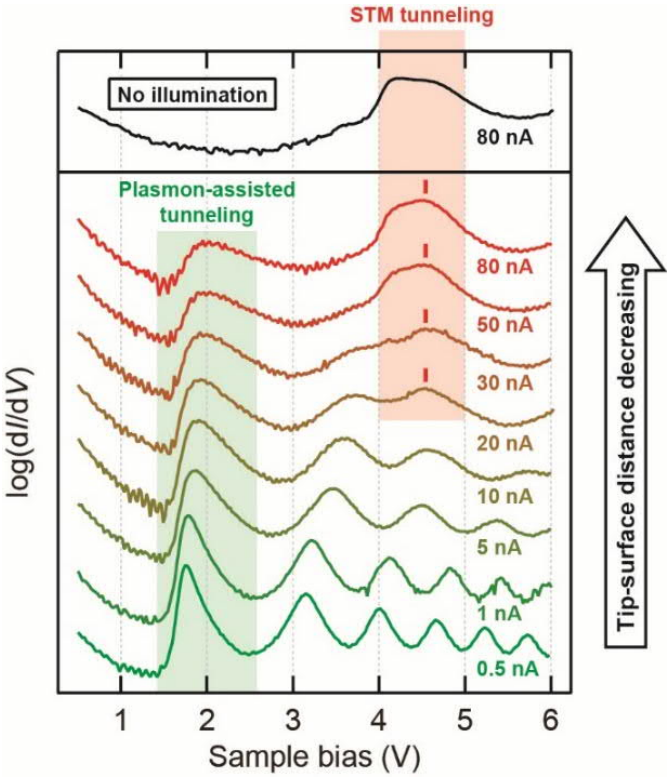

Figure 3.7. FER spectra measured over Ag(111) under illumination for different tip–sample distance, which is defined by the set current indicated in the figure. The laser wavelength is 532 nm and power density is 0.828 mWμm-2. The black bars indicate the second peak positions of plasmon-assisted tunneling process. The red bars indicate the first peak positions of direct tunneling process. The spectra are offset vertically for clarity. The top panel is the FER spectrum measured at the set current of 80 nA without illumination.

Recently it has been demonstrated that near-field properties in sub-nanometric cavities are significantly affected by quantum mechanical effects [148, 149, 150, 151, 152]. Electron tunneling in a sub-nanometer cavity will quench the field enhancement, and the theoretical studies have predicted that it happens at a gap distance of a few Å. Since the tip did not crash after approach 5 Å from tip surface distance with a set point of V_s = 1 V and I_t = 80 nA (closed tip surface distance in **Figure 3.7**), the tip-sample distance should be larger than the threshold gap distance of the field enhancement quenching. However, a substantial field enhancement still occurs even at the significant tunneling regime, which is implied by the results of **Figure 3.7**.

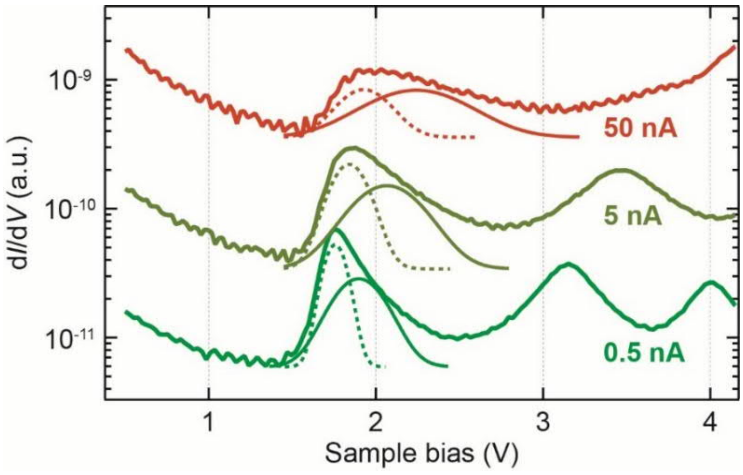

Figure 3.8. Fitting analysis of FER spectra in **Figure 3.7**.

As discussed in section 3.2, the *n*=1 peak includes two components, one is the first order FER and the other is from the edge of the bulk state of Ag [138] and this is also involved in the *n*'=1 peak. The *n*(*n*')=1 peak becomes broader and more skewed at smaller tip sample distance (**Figure 3.7**). **Figure 3.8** displays the fitting results of the *n*'=1 peak for three spectra in **Figure 3.7**. The component resulting from the bulk band edge remains almost the same position but the FER shows a slight blue-shift. This behavior of the two peaks is explained by a larger Stark effect for the FER than that for the bulk state because it is more localized above the surface, thus would be influenced stronger by the electric field in the junction. Additionally,

hybridization between the FER and the bulk states of surface or tip would also make it broader at smaller tip-surface distances [153].

3.4 Plasmon-assisted tunneling over 2-ML ZnO/Ag(111)

As discussed in next chapter, the work function of the ZnO layers is different from the Ag(111) surface. The plasmon-assisted tunneling was also examined over the ZnO layers. **Figure 3.9** is the FER spectra measured over 2-ML ZnO with and without illumination. In common with the case over Ag(111), the FER peaks also downshift. The first FER peak shifted ~2.3 eV that is again almost identical with the incident photon energy. The interface state (second peak in the spectrum) also appears in the FER spectrum measured under illumination. But the shifted energy is larger than 2.3 eV, which should due to the Stark effect.

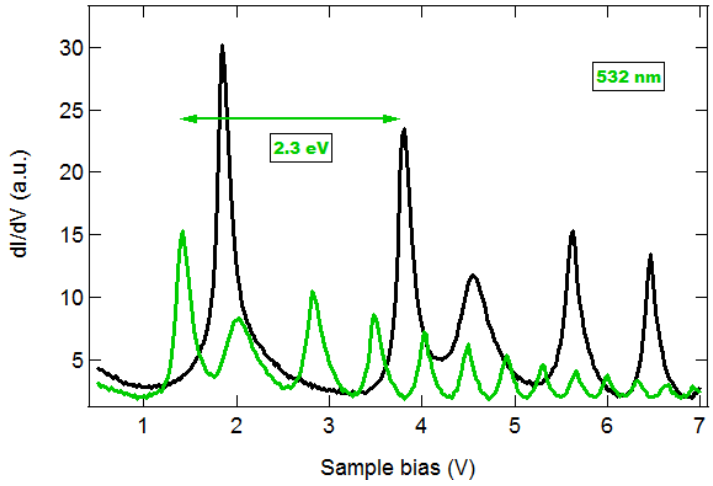

Figure 3.9. FER spectra measured over 2-ML ZnO surface with 532 nm illumination (green curve, $h\nu$ = 2.3 eV) and without illumination (black curve).

3.5 Conclusion

A novel electron transfer process in the plasmonic gap was revealed: the plasmon-assisted resonant tunneling from the STM tip to FERs over Ag(111) surface. The process is induced by CW laser excitation and is manifested as a drastic peak shift in FER spectrum. Three different wavelength lasers were used and the shift of the first FER peak is always equal the incident

photon energy. The STS maps identified the shifted peaks of higher order FERs. The incident laser power dependence and tip height dependence measurement show the tunable of preferred tunneling processes of direct tunneling or plasmon assisted tunneling. The plasmon excitation was influenced by the tip material, tip geometry and laser polarization. The similar plasmon-assisted tunneling process also observed over 2-ML ZnO films. STM can control the gap with sub-angstrom accuracy, combining STM with local optical excitation and detection has the advantage to study the near field property of sub-nanometer gaps, in which quantum effects play a crucial role and pure classical electrodynamics theory failed [154]. Resonant electron tunneling occurs via the FERs in the junction which serves as a simple model to examine near-field electron transfer in the plasmonic gap.

4 Local characterization of ultrathin ZnO layers on Ag(111) by SPM

4.1 Local geometric and electronic structure of the ultrathin ZnO layers on Ag(111)

4.1.1 Introduction

ZnO is a prominent material for a variety of applications such as photovoltaics, light emitting devices with the help of semiconducting and optical properties [155]. ZnO based system is also of an important catalyst used in methanol synthesis [156]. The bulk ZnO has three types of crystal structure, namely wurtzite, zinc blende, and rocksalt. In the (0001)-oriented wurtzite structure, the O and Zn planes are alternately stacked, resulting in a polar (0001) surface [157]. This is a classical polar oxide surface that leads to instability due to divergence of the surface dipole [158]. This type of surface is stabilized through several mechanisms including surface reconstruction, formation of ion vacancy, and hydroxylation [159], whereas it has been found that the ultra-thin (0001)-oriented ZnO films adapt a different mechanism. Tusche *et al.* found that the ultrathin ZnO films on Ag(111) are relaxed to form a flat structure like hexagonal-boron nitride (*h*-BN), but transferred to a bulk wurtzite structure from ~4 ML thickness [160]. In this respect, the (0001)-surface of ZnO attracted research interest from a basic science and potential application views.

In the reactive deposition method, the ZnO(0001) layers on Ag(111) initially grows as 2-ML island [118], which is also consistent with the DFT calculations that 1-ML ZnO is less stable[161]. The termination of the ZnO layers was examined by infrared reflection absorption spectroscopy (IRAS) which is one of the most sensitive methods to identify the surface hydroxyl species. In the ZnO(0001)/Ag(111) prepared by the reactive deposition method, the IRAS shows no hydroxyl formation on the surface [162]. This observation is consistent with the dipole compensation mechanism of the ZnO layer, in which the 2-ML ZnO layer relaxed to the *h*-BN-like flat structure.

In this chapter, the characterization of the ultrathin ZnO layers epitaxially grown on Ag(111) by STM/AFM is described. The local geometric and electronic structure of 2-, 3- and 4-ML ZnO layers is investigated by a combination of STM, AFM, and STS measurements. It

is found that the geometric and electronic structure depends on the layer thickness and the conduction band minimum downshifts with increasing the layer thickness. The local work functions are also investigated by FERs and CPD measurements. The work function dramatically drops by 1.2 eV from 2- to 3-ML ZnO due to the structural change from the flat geometry to the wurtzite-like buckled structure. The STS mapping reveals the spatial variations of the conduction band minimum and the change in the local work function at nanometer scale.

4.1.2 STM imaging and band structures

Figure 4.1a is an overview STM image of the ZnO layer on the Ag(111) surface with coverage of ~60%, obtained at 5 K, which involves the clean Ag(111) surface, 2- and 3-ML ZnO layers. The 4-ML ZnO islands were also rarely formed. **Figures 4.1b** and **c** are the enlarged STM image of 2- and 3-ML ZnO scanned with high (V_s=1 V) and low (V_s=0.1 V) bias voltages, respectively. The ZnO layers exhibit a Moiré pattern resulting from the ZnO(0001)-(7×7)/Ag(111)-(8×8) coincidence structure [118]. The Moiré pattern appears very uniform in 2-ML ZnO but is less ordered in 3-ML ZnO. The disordered feature of 3-ML ZnO is also discernible in the low bias STM image (**Figure 4.1c**). This difference is attributed to the dislocation defects as will discuss in section 4.2.4.

The periodicity of the Moiré pattern along the high symmetry axes of the Ag(111) surface is ~23 Å as show in **Figures 4.2a** and **c**. The apparent heights of the ZnO layers relative to the Ag(111) surface is measured in the STM images to be 3.8(±0.3), 5.8(±0.3), and 8.2(±0.3) Å for 2-, 3-, and 4-ML ZnO, respectively, as show in **Figure 4.2c** and **d**. The apparent height difference of ~2.0 Å is close to the interlayer distance of ZnO, which is 2.3(±0.1) Å for the 2-ML ZnO measured by surface x-ray diffraction [160]. Similar heights are also observed in the ZnO layers on Au(111) surface [163]. However, it should be noted that the apparent heights of the STM image depend largely on the scanning bias. The height of the ZnO layers relative to the Ag surface becomes ~6 Å for 2-ML ZnO at scanning bias of 1.8V and ~9 Å for 3-ML ZnO at scanning bias of 1.4 V [118]. The Moiré pattern in 4-ML ZnO is even less ordered, suggesting a disordered structure. The similar appearance is also observed for 4-ML ZnO on Au(111) [163].

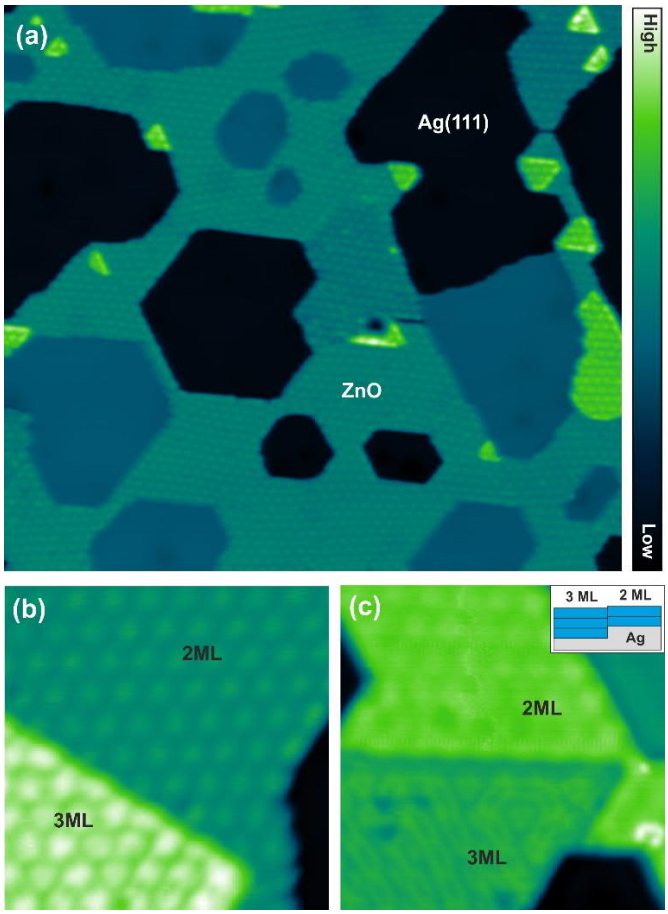

Figure 4.1. (a) Overview STM image of ultra-thin ZnO layers expitaxially grown on Ag(111) (5 K, V_s=1 V, I_t=0.1 nA, 1.2×1.2 um^2). (b) Enlarged STM image of ZnO layers scanned with higher bias voltage (5 K, V_s=1 V, I_t=0.1 nA, 20×20 nm^2). (c) Enlarged STM image of ZnO layer scanned with lower bias voltage (5 K, V_s=0.1 V, I_t=50 pA, 20×20 nm^2). The 3-ML ZnO layer is formed at a lower Ag terrace as show in the inset schematic.

The local electronic structure of the ZnO layers was measured by STS in the constant height mode. The conductance (dI/dV) spectra recorded over Ag(111), 2-, 3-, and 4-ML ZnO layers are displayed in **Figure 4.3**. The surface state of Ag(111) is observed as a step at about -70mV as shown in the inset of **Figure 4.3** [164, 165], indicating that the surface is atomically clean. The conduction band minimum appears as a step-like increase in the STS spectra, which downshifts with increasing the layer thickness and found to be ~1.9 V, ~1.6 V, and ~1.5 V for 2-, 3-, and 4-ML ZnO, respectively. The band gap of a free standing 2-ML ZnO layer is calculated to be ~5.1 eV by theoretical calculations using GW approach [166]. Considering the measured conduction band minimum is 1.5~2 V in the STS spectra, the valence band maximum

is expected to appear around -4 V. However, there is no obvious resonance from 0 to -4 V in the STS spectra. But it is also difficult to identify the ZnO state unambiguously because it may be strongly hybridized with the *d*-band of the Ag substrate.

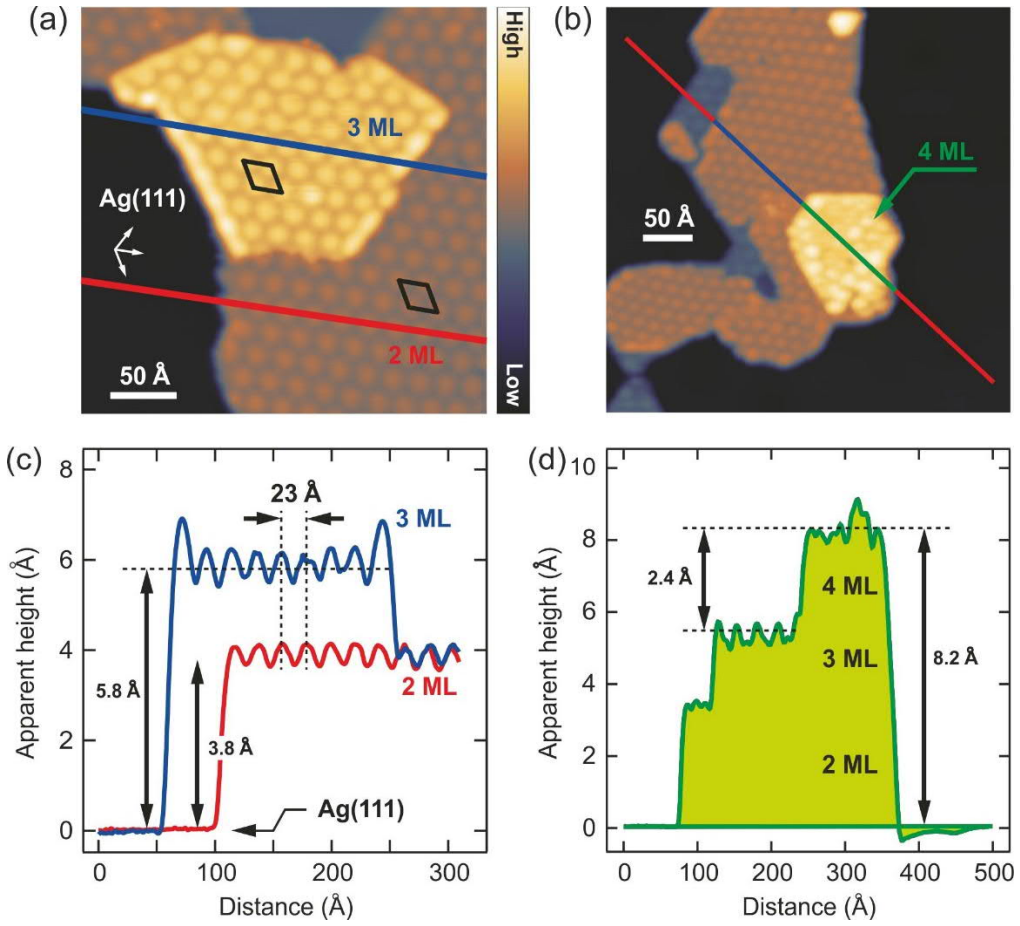

Figure 4.2. (a) STM images of 2- and 3-ML ZnO layers on Ag(111) (5 K, *V*s=1 V, I_t=0.1 nA, 30×30 nm2). The three arrows mark the high-symmetry orientations of the Ag(111) surface. The black rhomboids indicate the unit cell of the ZnO(0001)-(7×7)/Ag(111)-(8×8) coincidence structure. (b) STM image of 2-, 3-, and 4ML-ZnO layers on Ag(111) (5 K, *V*s=1 V, I_t=0.1 nA, 40×40 nm2). (c) Line profiles of the ZnO layers. The red and blue lines are for 2- and 3ML-ZnO, respectively. The measured lines are indicated in (a). (e) Line profile across the 2-, 3-, and 4-ML ZnO layers in (d).

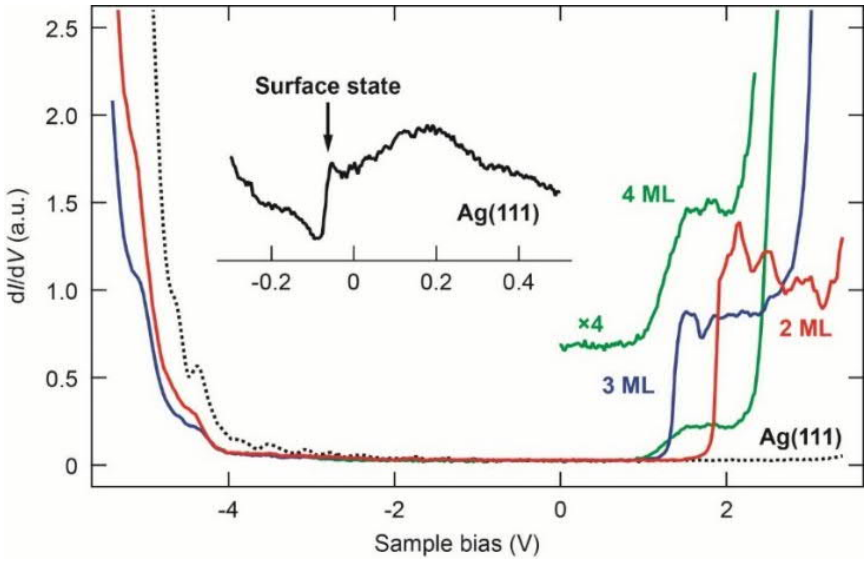

Figure 4.3. STS spectra of the ZnO layers on Ag(111) measured in the constant height mode at 5 K. The black, red, blue and green curves are measured over Ag(1 1 1), 2-, 3-, and 4ML-ZnO, respectively. The tip-surface distance was fixed at a set point of V_s=1 V and I_t=0.3 nA. The solid black curve shows the surface state of Ag(111), which measured at a set point of V_s=0.5 V, I_t=10 nA.

4.1.3 Local work function measurement

The local work functions of ZnO/Ag(111) were investigated by measuring the FER spectra. In contrast to the STS measurement in the constant height mode (**Figure 4.3**), the FER spectra are measured in the constant current mode. In the latter case, the STM feedback is turned on to keep the tunneling current constant during the measurement. Therefore, the tip–sample distance is displaced during the bias sweep as shown in **Figure 4.4a** (red dash curve). This mode can avoid the saturation of the tunneling current at a high bias voltage and allows to record the STS spectrum in a wider voltage range than that of the constant height mode measurement. The FER spectra measured over Ag(111), 2-, 3-, and 4-ML ZnO are shown in **Figure 4.4a**. All spectra show no influence from the Moiré pattern, *e.g.*, spectra are the same for bright or dark area. This is in contrast to the FER spectra measured over 1-ML NaCl on Ag(100), which exhibits significantly different spectra depending on the position the Moiré pattern [167]. The different behaviors are attributed to the extent of the charge density modulated by a Moiré pattern. The Moiré contrast in the NaCl is more pronounced and the STM appearance height of that

corrugation is ~2 Å in NaCl, which is larger than ZnO on Ag(111) (~0.3 Å). Therefore, the charge density modulation may be rather small for the ZnO layers on Ag(111).

The measured FER spectra are fitted fairly well with a series of Voigt functions with a linear background. The precise peak positions are extracted from the multiple peak fitting. The first peak in the FER spectrum of Ag(111) involves two components. The smaller component at lower energy is assigned to the edge of the bulk state [168]. A similar feature has also been observed on Cu(111) and Au(111) [169, 170]. The bulk state edge near the first FER state is observed by inverse photoemission spectroscopy for Au(111) surface [171]. The first peak in the conductance spectra of the ZnO layers corresponds to the conduction band minimum, which is observed in the constant height mode measurement as a stepwise feature in **Figure 4.3**. The other peaks at higher voltages correspond to the FER states. These are standing wave states located in the vacuum gap between STM tip and the surface [172]. Besides the conduction band and the FER states, there is an additional state near the vacuum level of the Ag(111) surface at ~4.5 V for the ZnO layers and its intensity becomes lower in the thicker layers. This peak is assigned to the interface state between ZnO and the Ag(111) surface. Because a wider barrier is expected between the interface state and tip over a thicker ZnO layer, the intensity of the interface state becomes lower. On the other hand, the FER has a higher tunneling probability than the interface state (the interface state is buried under ZnO layer, resulting in a wider tunneling barrier from the tip. A similar interface state has been report in rare gas/metal interfaces [173,174] and MgO/Ag(100) interface [175].

A simplified 1-D model of a tunneling junction has been used to analyze the measured FER spectra [176,177]. The model is shown in the inset of **Figure 4.4b**, in which the potential in the junction comprises the superposition of the image potential and the electrostatic potential formed by the applied bias voltage between the tip and the sample. The image potential becomes negligible at high order FERs, then the junction potential can be approximated by a triangular potential [178], thus

$$eV_n = \phi_n + \left(\frac{3\pi\hbar e}{2\sqrt{2m}} En\right)^{2/3} \qquad (4.1)$$

where e is the elementary charge, V_n the applied bias of n's order FER, E the electric field of the tunneling junction from the applied bias. Since the lower-order FERs are influenced by the image potential, this approximation is no longer precise. Therefore, we included only the higher-order FERs ($n \geq 3$) into the estimation of the local work function using Eq. (4.1) [170].

The obtained work functions are 4.2 (± 0.2) eV for Ag(111), 4.0 (± 0.2) for 2-ML ZnO, 2.8 (± 0.2) for both 3- and 4-ML ZnO layer. The work function for Ag(111) is lower than the value from the photoemission spectroscopy measurement (4.74 eV) [179]. This deviation is most probably ascribed to the oversimplified 1-D model. In this model the sample surface is represent by an infinite high potential and penetration of the FER waves into the sample surface is also not considered.

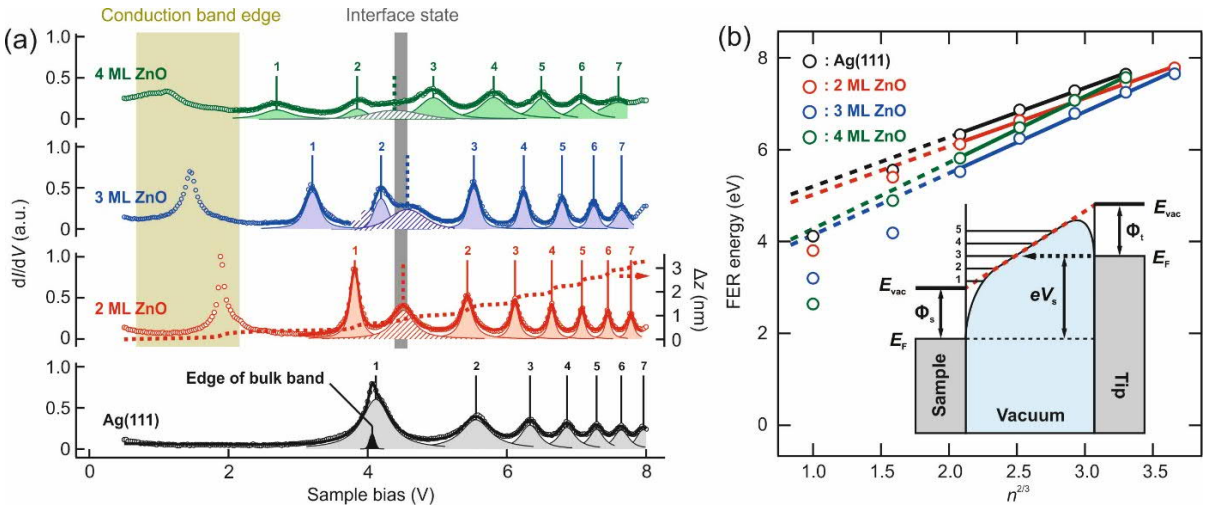

Figure 4.4. (a) FER spectra measured for ZnO/Ag(111) in the constant current mode over ZnO/Ag(111). The black, red, blue and green curves are measured over Ag(111), 2-, 3-, and 4-ML ZnO, respectively. The STM feedback loop was kept to yield I_t=5 nA during the measurement, which results in the displacement of tip–surface distance during the measurement. The red dashed curve is the displacement of tip–surface distance recorded for 2-ML ZnO. The open circles are the measurement data and solid curves are the best fitted results with multiple Voigt functions with a linear background. The shaded curves are the individual fitted peaks. The FER levels (n) are marked with numbers over the peaks. (b) Local work function analysis. The open circles are the fitted peak positions *vs.* $n^{2/3}$ and the lines are fitting result by equation (4.1) (the solid lines are the fitting with data of $n > 2$, the dashed lines are the extrapolation). The potential is schematically show in the inset. E_f, E_{vac} and $\Phi_s(t)$ are the Fermi level, vacuum level and work function of sample (tip), respectively.

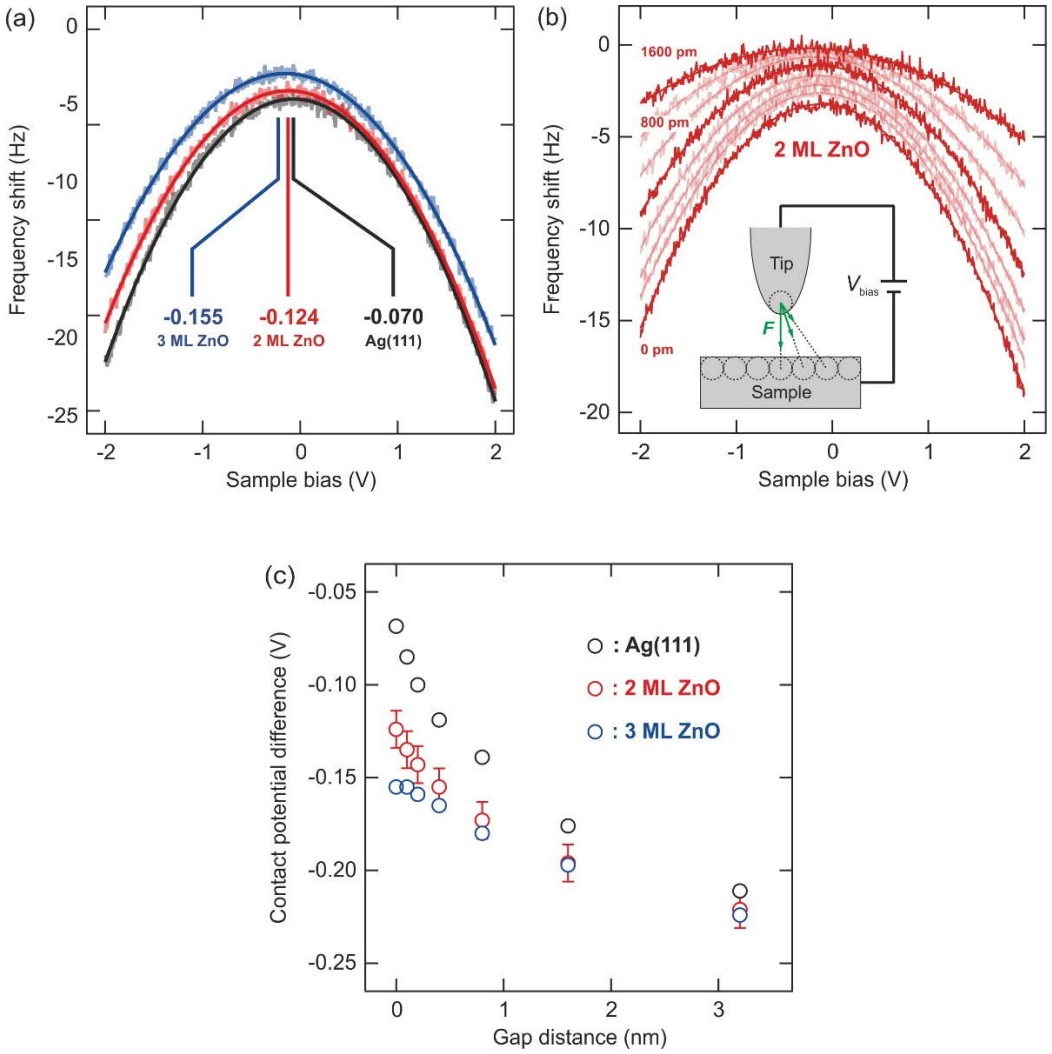

Figure 4.5. (a) CPD measurement for ZnO/Ag(111). The black, red, blue curves are measured over Ag(1 1 1), 2- and 3-ML ZnO respectively. The tip–surface distance was fixed with set point V_s=2 V, I_t=1.5 nA. The CPD was measured to be −0.070, −0.124, and −0.155 V for Ag(1 1 1), 2-, and 3-ML ZnO, respectively. (b) Measured frequency shift *vs.* bias sweep with different tip-surface distance over 2-ML ZnO. The zero-point in the horizontal axis corresponds to the STM set point of V_s=2 V, I_t=1.5 nA. The electrostatic force between tip and sample is schematically shown in the inset. (d) CPD measured with different tip-surface distance over Ag(111), 2- and 3-ML ZnO.

It is interesting that the work function decreased only by 0.2 eV from Ag(111) to 2-ML ZnO, but it decreases by 1.2 eV over 3-ML ZnO. This is in contrast to the case of MgO and NaCl layers on Ag(100) where the local work function changes do not depend on the layer

thickness [176, 180]. The dramatic change from 2- to 3-ML ZnO layer should relate to the structure change, which will also be discussed in section 4.2. DFT simulations also proposed a structure change for the 3-ML island from the *h*-BN-like structure of 2-ML ZnO [181].

In general, the work function reduction results from three different contributions when the surface is covered by dielectrics. One is the charge transfer from the adsorbed layer to the substrate. Second is the "pillow effect" that reduces the electron density spilling out from the substrate surface [182]. Third is the surface dipole formation due to the structure change. A relaxation of interface could modify the interface dipole and a polar adsorbate could also change the surface dipole. The charge transfer is unlikely between ZnO layer and Ag(111) because the Fermi level of Ag(111) is located in the band gap of ZnO layer (**Figure 4.3**). The structure relaxation of the ZnO layer would influence parameters of the latter two mechanisms. Therefore, the structure change from 2- to 3-ML ZnO will result in a dramatic work function change. For example, DFT simulations pointed out the important role of structure relaxation on the work function of 1-ML MgO layer on Ag(100) [182].

The reduction of the work function over the ZnO layers was also examined by the CPD using AFM. **Figure 4.5a** shows the frequency shift curves measured over Ag(111), 2-, and 3-ML ZnO, which were fitted with a parabolic curve to obtain the CPD. The result shows that the work function is reduced on ZnO layers as compared to Ag(111). The trend is similar as the results of the FER measurements, but the amount are much smaller. In the CPD measurement, the electrostatic force results not only from the sample just underneath the tip, but also from the sample around that [180]. Therefore, in the measurement over ZnO layer, the surrounding Ag(111) surface also contributes to the electrostatic force, which will make the measured CPD is smaller than the real one. This effect is also shown in the CPD measurement with different tip sample distances. **Figure 4.5b** shows the CPD measurement of different tip sample distance over 2-ML ZnO. The CPD is larger with the tip sample distance decreased. The CPDs measured at different tip sample distance for Ag(111), 2- and 3-ML ZnO are show in **Figure 4.5c**. The work function reduction is obvious at small tip sample distance measurement.

4.1.4 Conductance maps

Figure 4.6 displays the STS maps at a different bias voltage. **Figure 4.6a** is the topographic STM image of the measured area which includes Ag(111), 2-, 3-, and 4-ML ZnO layers.

Figures 4.6b and **c** are the conductance maps measured at the bias voltage of the conduction band minimum for 3- (1.45 V) and 2-ML ZnO (1.95 V), respectively, where the intensity variation of the STS signal can be observed. Comparing with the extended layers, the intensity of small islands in the first FER resonance map is significantly weaker. This may be explained by the confinement effect and the first FER peaks upshifts by ~50 meV in the FER spectra. **Figure 4.6e** shows two FER spectra measured over 2-ML ZnO. The red curve was measured over the intact position, whereas the black one was measured over a defect position. The peaks of the conduction band and the first FER of the black curve exhibit a downshift. It is interesting that there is no defect visible in the topographic image, suggesting that the defect may be buried inside the layer or in the Ag surface. **Figure 4.6g** is the conductance map of 4.3 V, which shows the distribution of the first FER of Ag(111) and the second FER of 3-ML ZnO. **Figure 4.6h** is the conductance map of the interface state, so that it distributed over the all ZnO layers and the intensity is weaker at thicker layer area as discussed before.

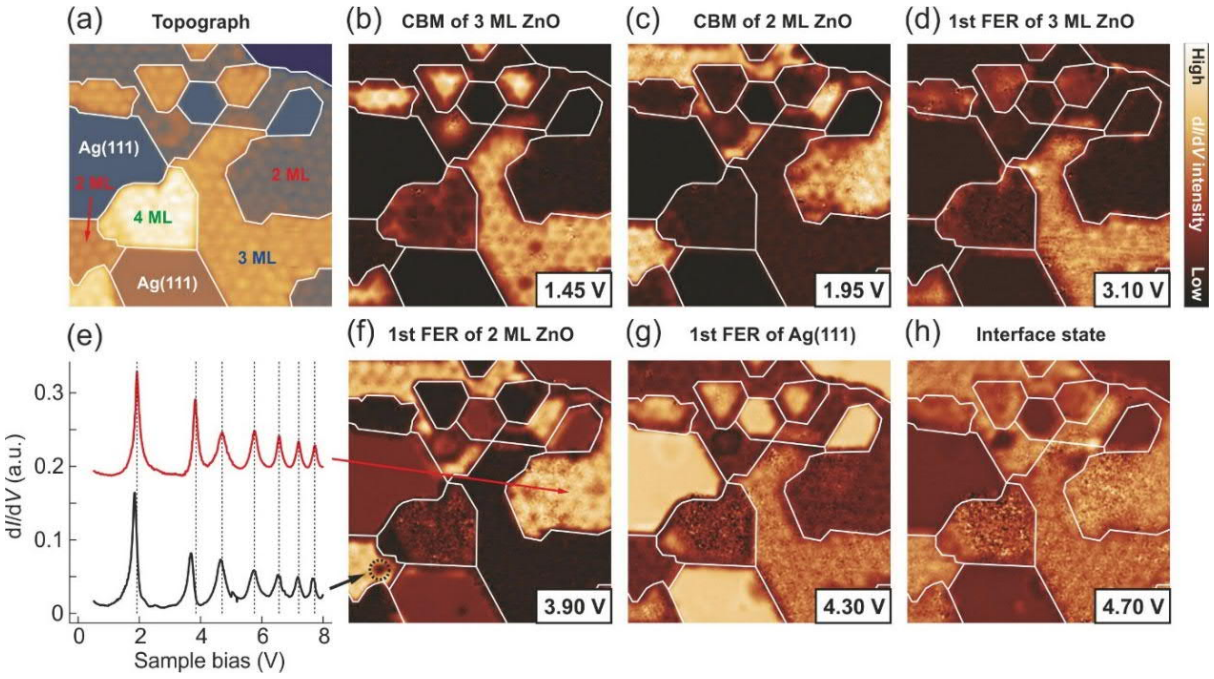

Figure 4.6. (a) STM image (5 K, V_s=1.45 V, I_t=1 nA, 35×35 nm2) for the dI/dV mapping. The boundaries between different regions are indicated with the white lines. (b), (c) are dI/dV mappings for the conduction band minimum (CBM) of 3- and 2-ML ZnO, respectively. (d) dI/dV mappings with bias of first FER of 3-ML ZnO. (e) FER spectra measured over an intact (red) and defect (black) site on 2-ML ZnO. The measured position is marked with arrows in (f) and the defect site is

indicated with black dashed circles. (f) (g) d*I*/d*V* mapping with bias of the first FER of 2-ML ZnO and Ag(111) respectively. (h) d*I*/d*V* mapping for the interface state between Ag(111) and ZnO layers. The bias voltages of the d*I*/d*V* map are indicated at the bottom right of the respect images.

4.1.5 Conclusions

We investigated the electronic structure and work function of 2-4 ML ZnO(0001) layers on Ag(111) by STM and AFM at 5 K. It was found that the conduction band minimum of ZnO layers monotonically downshifts with increasing the thickness. The work function is slightly reduced from Ag(111) to 2-ML ZnO layer, but dramatically reduced for 3-ML ZnO, which implies the structure change between 2- and 3-ML ZnO layer. This structure change will modify the interaction between ZnO layer and Ag(111), which results in the dramatic work function reduction. The trend of work function reduction is also proved by the CPD measurement by AFM. But the estimated work function change from CPD measurement is much smaller than that form the FER measurement, which is may be ascribed to the spatial averaging effect. The conductance maps display the distributions of conduction bands and FERs, which visualized the possible defect buried inside the sample and the local work function variation at nanometer scales.

4.2 STHM imaging for ZnO layers on Ag(111)

4.2.1 Introduction

As a powerful tool for surface science study, SPM is wildly used for oxide surface characterization. As demonstrated in section 4.1, we used it to characterize the local geometric and electronic structure and local work function of the ultrathin ZnO layers. The spatial resolution of SPM can be enhanced with functionalized SPM tip and a carbon monoxide (CO) adsorbed on the tip apex is one of the most common way. The spatial resolution of STM [183], AFM [184, 185, 186] and also molecular orbital imaging [187] can be enhanced with the CO functionalized tip. It has also been found that molecular hydrogen (H_2) trapped inside the STM junction can enhance the spatial resolution to resolve submolecular structures of planar organic molecules [81]. It is named as scanning tunneling “hydrogen” microscopy (STHM). The

enhanced imaging capability is attributed to the Pauli repulsion in the junction with the tip at a short distance to the surface [188, 82, 189]. However, a similar enhancement effect was also reported at a larger tip–sample distance where the Pauli repulsion can be ignored [190]. The nanoscale junction with H_2 inside has also been studied as a simple model of molecular junctions. It was studied by STM [191, 192, 193], AFM [194], and mechanical break junction [195, 196, 197]. However, the accurate structure of the H_2 junction is difficult to characterize and the resolution enhancing mechanism of STHM is yet imperfectly understood. The STHM was reported to image planar organic molecule in most cases. Here we apply this technique to imaging ultrathin ZnO layers. From the enhanced resolution imaging, the defective feature of 3-ML ZnO was resolved. In addition, the conductance and mechanical properties of the H_2 junction were investigated. The measured conductance and force curve exhibit kink-like features at the same tip–sample distances, which are absent in the H_2 free junction. We reveal that the junction contains multiple H_2 molecules and a simplified model with two H_2 in the junction can reproduce qualitatively the measured conductance and force curve as well as enhanced resolution imaging.

4.2.2 STHM imaging of ZnO layers, conductance and mechanical properties of the junction

Figure 4.7a is an STHM image obtained after dosing 22 Langmiur (L) H_2 gas. The morphology of the ZnO layer is not affected and the Moiré pattern is still visible. However, the lateral resolution is significantly enhanced with H_2. The presence of H_2 in the STM junction is manifested as the dips in the conductance spectra as show in **Figure 4.7b**. The three spectra were measured with the same tip conditions after dosing H_2. A similar spectral feature has been reported before and the dips have been attributed to the bi-stable motion of the H_2 molecule inside the tunneling junction induced by vibrational excitation [191, 198, 199, 200]. At relatively low exposure of the H_2 gas, the molecules prefer to adsorb onto the ZnO layers (**Figure 4.8a**). H_2 also adsorbs onto the Ag(111) surface at the edge positions as shown in **Figure 4.8b**.

Figures 4.9a and **b** are enlarged STHM images of 2-ML ZnO layer obtained in the constant current and constant height mode, respectively, for the same area under the identical tip conditions. The constant height mode imaging is more stable and exhibits a higher resolution than the constant current mode. The lattice constant determined from the high resolution image

is ~0.32 nm, which matches well the value from the surface x-ray diffraction (SXRD) measurement (0.3303(2) nm [160]). The atom positions can be clearly distinguished in the high resolution image, but the O and Zn atoms cannot be identified.

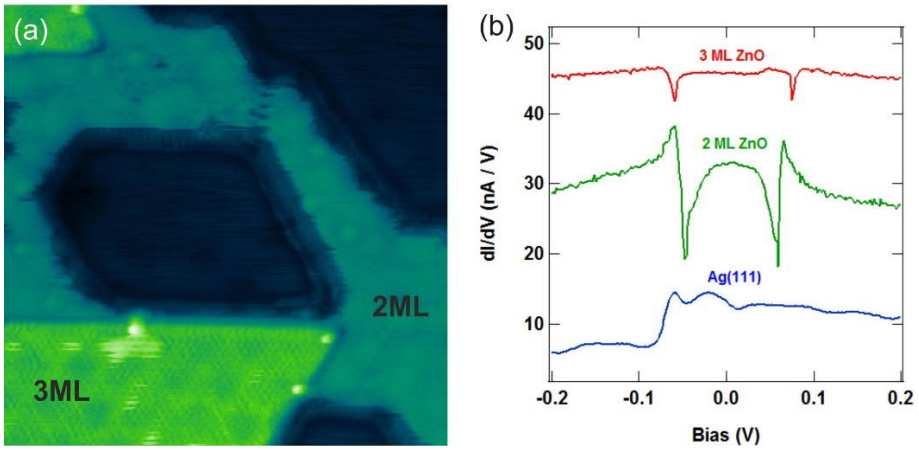

Figure 4.7. (a) STHM image after dosing 22-L H_2 (5 K, V_s = 0.1 V, I_t = 0.1 nA, 20 × 20 nm^2). (b) dI/dV spectra measured with a PtIr tip of the same condition over Ag(111), 2- and 3-ML ZnO after dosing the H_2 gas. The tip height was fixed with set point 1 V, 1 nA.

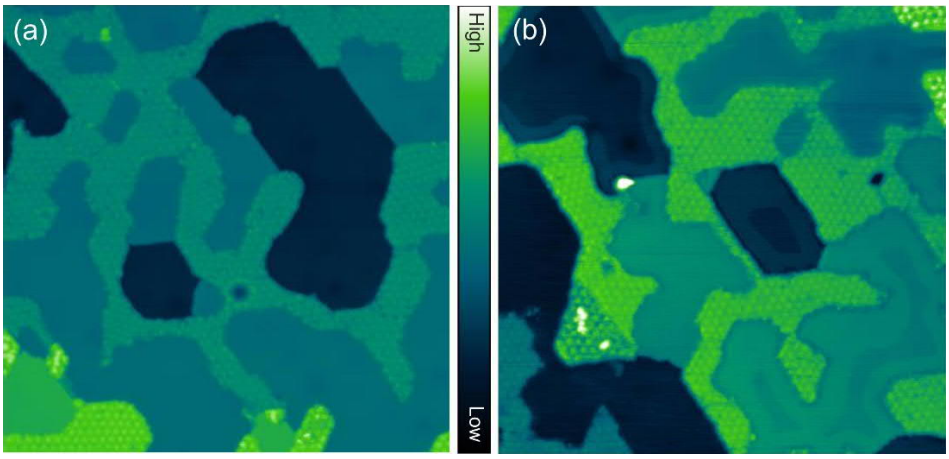

Figure 4.8. (a), (b) STM images after dosing 9 and 40.5-L H_2 respectively at 13 K (V_s = 0.1 V, I_t = 0.1 nA, 0.1 × 0.1 um^2).

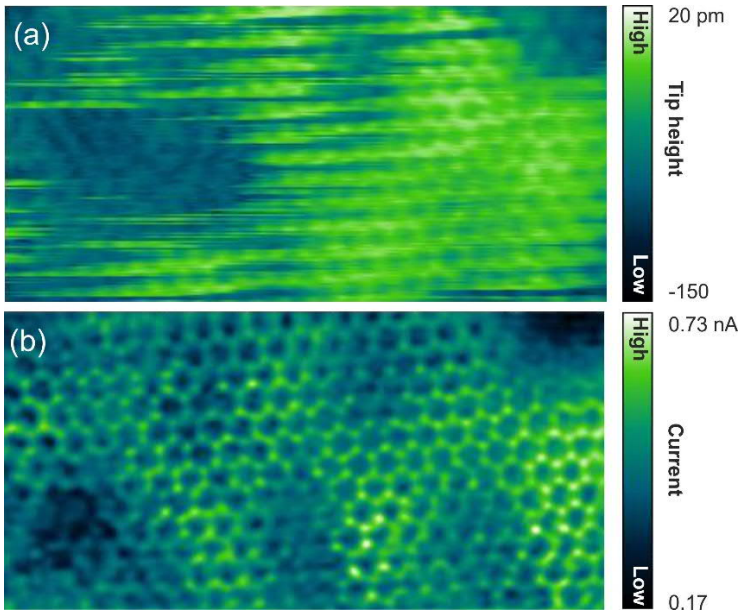

Figure 4.9. (a), (b) The STHM images of 2-ML ZnO layers scanned with constant current (5 K, V_s = 0.1 V, I_t = 0.46 nA, 3.5 ×7nm^2) and constant height (5 K, V_s = 0.1 V, 3.5 ×7nm^2) mode with the same tip condition.

We found that the enhanced resolution image can be obtained only in a narrow range of the tip-sample distance. **Figure 4.10a** is the conductance curve ($G(z)$) as a function of the tip-sample distance measured over 2-ML ZnO layer with and without H_2. In contrast to the curve without H_2, there are three kink-like features in the curve for the H_2 junction, which are marked by black arrows. **Figures 4.10b-f** are the STHM images scanned with different tunneling currents. The corresponding tip-sample distances are marked by open circles in **Figure 4.10a**. The highest resolution (**Figure 4.10c**) is obtained at a relative large tip–sample distance of the second kink-like feature position in $G(z)$ curve. The tips made of different materials (W, PtIr and Au) exhibit the same behavior. The distance between the kinks Δd_{kink} is always ~0.3 nm, which is not influenced by tip conditions as also shown later in the AFM measurement.

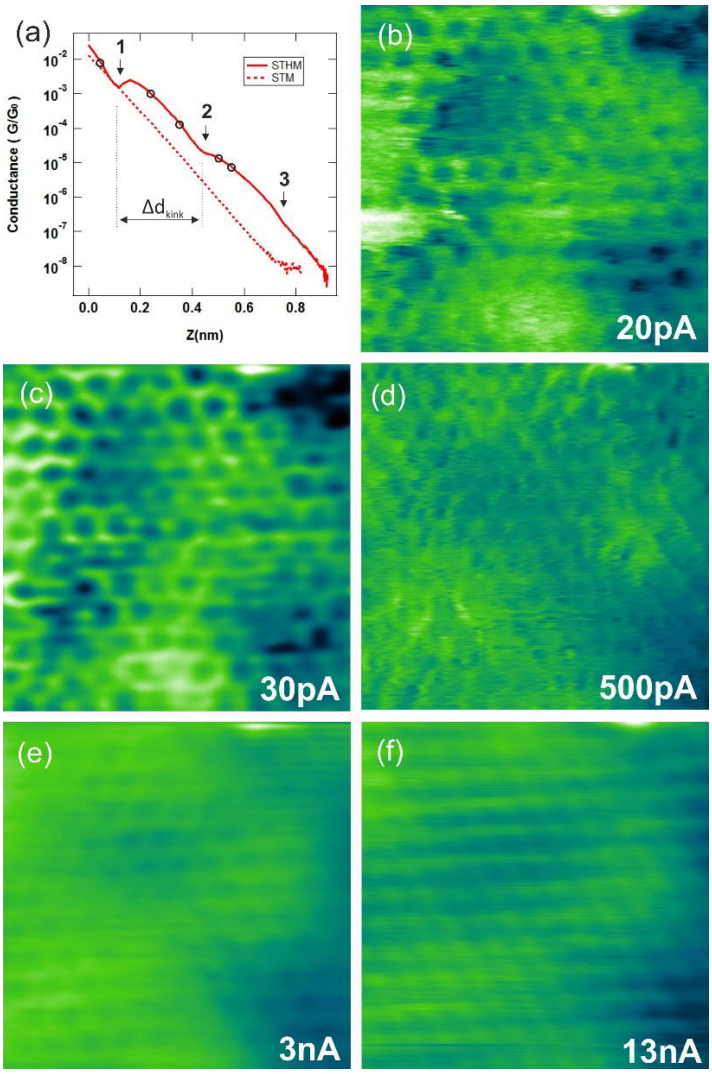

Figure 4.10. (a) Conductance *vs.* tip–surface distance displacement curves measured over 2-ML ZnO before (dashed curve, zero displacement set point: V_s = 30 mV, I_t = 30 nA) and after (solid curve, zero displacement set point: V_s = 30 mV, I_t = 60 nA) dosing H_2. $G_0 = 2e^2/h$ is the quantum conductance. The kink-like features are indicated with arrows. (b)-(f) STM images of 2ML-ZnO scanned with different tip–surface distance after dosing H_2 and the tip–surface distances are determined by the set currents as indicated in the right down corner (5 K, V_s = 30 mV, 3.5 × 3.5 nm^2). The measurement are performed with the same condition of a PtIr tip.

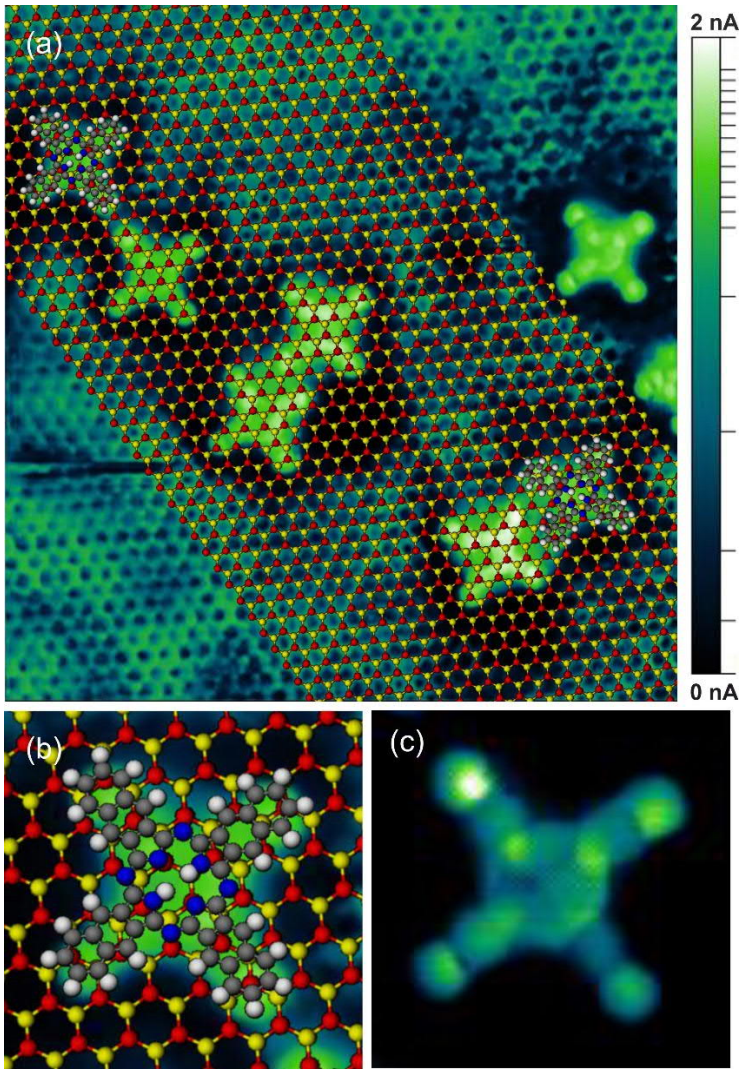

Figure 4.11. (a) STHM image of 2-ML ZnO and adsorbed NPc molecules scanned in the constant height mode (5 K, V_s=50 mV, 11×11 nm^2). The *h*-BN-like structure model of 2-ML ZnO and NPc molecules in the gas phase is superimposed (red: Zn, yellow: oxygen). (b) Enlarged structure model of adsorbed NPc. (c) Enlarged STHM image of the NPc molecule in (a).

Figure 4.11a is the STHM image of naphthalocyanine (NPc) molecules on the ZnO layer. This enhanced resolution image was obtained in the constant height mode. The adsorption site of the NPc molecules can be determined by superimposing the model of ZnO layer and NPc molecules. The obtained adsorption geometry is shown in **Figure 4.11b**. From the high resolution image of the ZnO layer, the O and Zn atom cannot be identified directly. But it can be speculated from the adsorption geometry of NPc. The N atoms in phthalocyanines probably prefer to interact with cation atoms. For example, in the adsorption of phthalocyanine on NaCl

layer, the imine N atoms bonded to the Na atoms [201]. With this consideration, we suggest that the imine N atoms in NPc interact with the underneath Zn atoms. The obtained high resolution image of NPc is similar as the STHM image of organic molecule reported before. It appears darker at the atom positions [188]. But it is bright at the atom positions in the ZnO layers in STHM image as obviously seen in **Figure 4.9**.

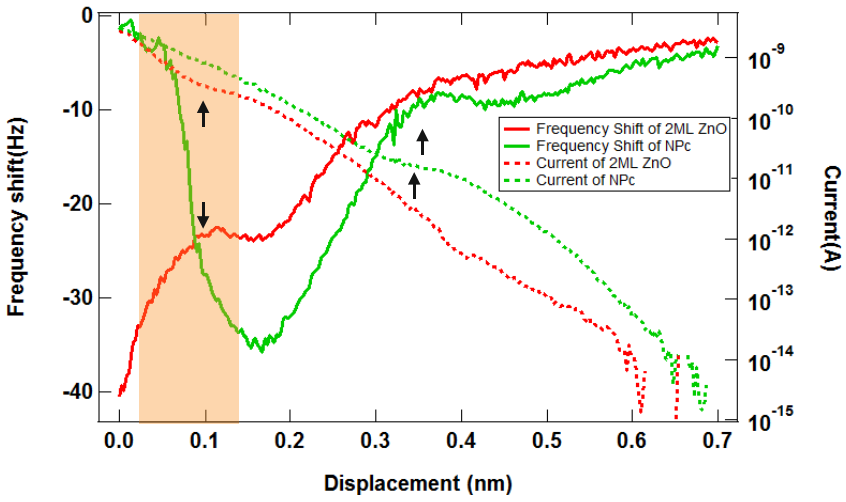

Figure 4.12. $\Delta f(z)$ (solid lines) and $I(z)$ (dashed lines) recorded simultaneously over 2-ML ZnO (red curves) and the adsorbed NPc molecule (green curves) under the same tip conditions. The data are obtained by qPlus sensor with a W tip. A small bias voltage of V_s=10 mV is applied between the tip and the sample during the measuring. The kink-like features in the $I(z)$ and $\Delta f(z)$ curve are marked with arrows. The orange region marks the distances (between the tip and 2ML ZnO) that the spatial resolution is enhanced for ZnO layer.

We also measured the mechanical property of the STHM junction over NPc molecule and the ZnO layer by AFM. **Figure 4.12** is the frequency curve $\Delta f(z)$ shows the measured frequency shift at a different tip sample distance, where the red and green curves are measured over 2-ML ZnO and NPc, respectively, under the same tip conditions. A small bias voltage of 10 mV was applied between the tip and the sample during the AFM measurement and the tunneling current $I(z)$ was recorded simultaneously. The kink-like features appeared in both $\Delta f(z)$ and $I(z)$ at the same tip–sample distance as indicated by arrows in **Figure 4.12**. The kinks result from a structure change inside the junction which causes a variation in the force and conductance

simultaneously [188]. The orange color marks the specific tip–sample distance where the high resolution image can be obtained. The $\Delta f(z)$ curve of NPc shows a strong repulsion in this regime and the enhanced resolution image of NPc was also obtained. This is consistent with the previous studies in which a Pauli repulsion is responsible for the STHM imaging of organic molecules [188, 82]. However, the orange regime is still attractive for ZnO layer, implying a different imaging mechanism.

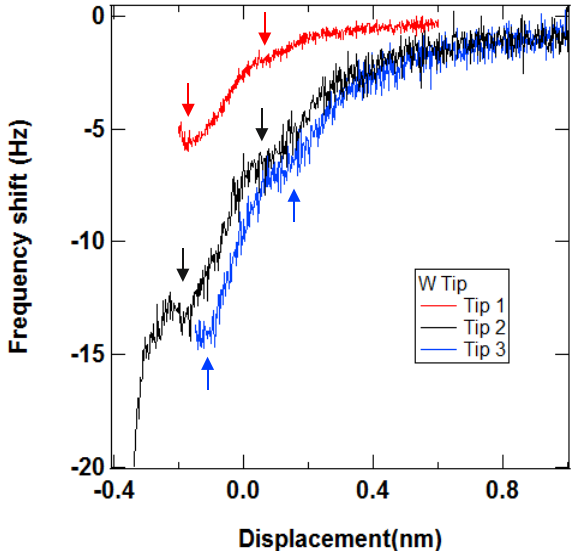

Figure 4.13. Frequency shift curves measured with three different W tips for 2-ML ZnO. No bias voltage is applied between the tip and sample during the measurement. The kink-like features are indicated with arrows. The different tip conditions were obtained by touching of the tip apex and Ag surface or voltage pulse applied between the tip and sample.

Figure 4.13 shows the $\Delta f(z)$ curve of the STHM junction measured over 2-ML ZnO under different tip conditions. The distances between the kinks are always observed to be ~0.3 nm. A similar STHM image of the ZnO layer was obtained with a bias voltage below and above the dip voltage in the conductance spectra. The rotational or vibrational mode of H_2 in the STHM junction will be excited with a bias voltage above the dip voltage. Also, provided the adsorption geometry of H_2 on different tip apex will also be different, the H_2 orientation of STHM should play a minor role.

4.2.3 Simulation of the junction with two H_2 inside

We consider a simple model with two H_2 trapped inside the STM junction to simulate the imaging mechanism and the kink-like feature in $I(z)$ and $\Delta f(z)$ curves over the ZnO layer. The model is illustrated in **Figure 4.14a**. One H_2 is adsorbed on the tip apex and the second H_2 is adsorbed on ZnO layer underneath the tip. One H_2 is expected to be squeezed outside the junction when the tip-sample distance becomes to smaller as shown in **Figure 4.14b**, which results in a kink in $I(z)$ and $\Delta f(z)$. The second H_2 will be squeezed out too with even smaller tip sample distance (**Figure 4.14c**), resulting in the second kink. The distance difference Δd in **Figure 4.14b** and **c** should be around the equilibrium distance between H_2 that is ~0.3 nm [202]. Δd is the Δd_{kink} in conductance curve in **Figure 4.10a**. A similar kink-like feature is observed in the STM junction that contains one or two Xe atoms. The observed kink distance Δd_{kink} is ~0.45 nm due to the larger size of Xe atom [203].

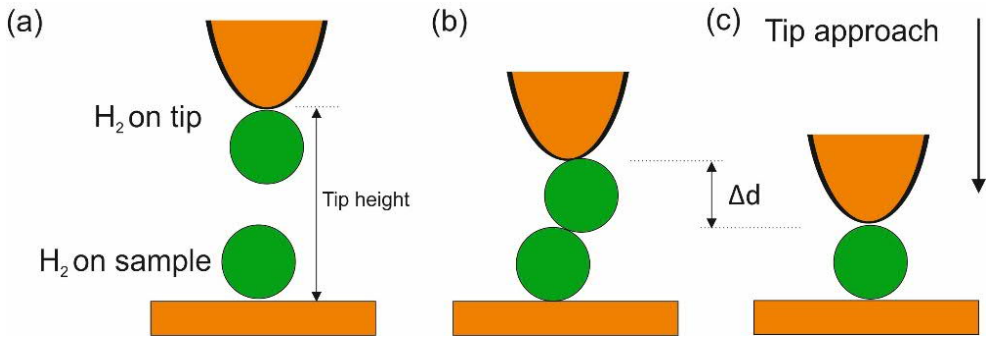

Figure 4.14. (a)-(c) Schematic models of the STM junction with two H_2 molecules at different tip sample distances.

We simulated the conductance curve, force curve and STHM imaging as demonstrated in *Phys. Rev* B **90**, 085421 (2014), but with two H_2 molecules inside the STM junction as described above. An *h*-BN-like flat structure of single layer ZnO was used to model the ZnO layer. The lattice parameter is 3.2 Å determined from the high-resolution STHM image. The tip apex and H_2 both represent by spherical atoms. Interaction of this tip-H_2-ZnO junction are described the pairwise Lennard-Jones (LJ) potentials. The H_2 adsorbed on the tip also interacts with the tip base that is represented by a lateral harmonic force of stiffness k = 0.5 N/m. The total interaction energy is the sum of all pairwise LJ potentials and the harmonic interaction energy. The two H_2

positions are optimized to minimize the total interaction energy at each simulation step. The accuracy of energy minimization is 10^{-6} eV.

Since there is no obvious contrast for O and Zn at most time, the same parameters are used for O and Zn. The interaction energy between atoms i and j: $E_{ij} = \frac{B_{ij}}{r^{12}} - \frac{A_{ij}}{r^6}$, where $B_{ij} = 2\varepsilon_{ij} r_{ij}^6$, $A_{ij} = \varepsilon_{ij} r_{ij}^{12}$, $r_{ij} = r_i + r_j$, $\varepsilon_{ij} = \sqrt{\varepsilon_i \varepsilon_j}$. The interaction parameters are listed in the table.

	εi (meV)	ri (Å)
H_2	0.680	1.487
O/Zn	3.729	1.908
Tip apex	1000	2

Table of the parameters of the LJ potentials used in the calculations.

A one-dimensional, three-barrier model was used to simulate the conductance of the junction as illustrated in **Figure 4.15**. The H_2 molecules are regarded as a potential well. According to the Wentzel-Kramers-Brillouin (WKB) approximation, the conductance is described by the product of the tunneling probability $T \propto T_1 T_2 T_3$, where T_1, T_2, and T_3 are the tunneling probability between tip and H_2 on the tip, between two H_2, between ZnO surface and H_2 on ZnO, respectively. These tunneling probabilities exponentially decay with increasing the corresponded gap distance, thus $T_n \propto \exp(-\beta_n d_n)$, ($n$ = 1, 2, 3), where β_n are the decay constants determined by the barrier shape, d_1 is the distance between the tip atom and the H_2 on the tip, d_2 is the distance between two H_2, d_3 is the distance between H_2 on ZnO and the ZnO surface. We use β_n = 1 Å^{-1} in the simulation because the practical barrier shape cannot be determined and only the relative conductance change is concerned here.

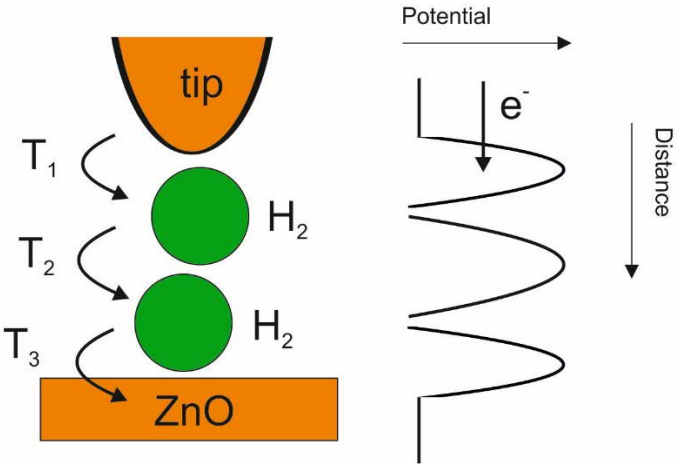

Figure 4.15. Schematic of the STM junction with two H_2 inside. The schematic potential is also depicted.

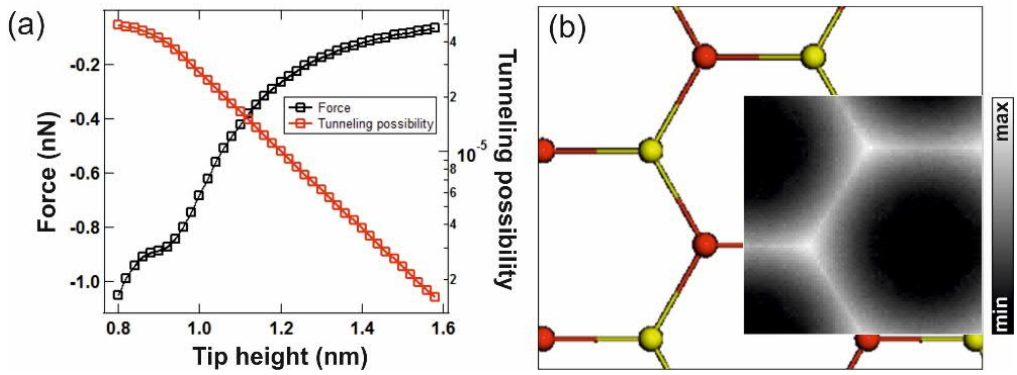

Figure 4.16. (a) Simulation of the vertical force for the tip (perpendicular to the ZnO surface) and the total tunneling probability (T) at different tip-ZnO distances. During the simulation the tip is located above the central position of Zn-O bond. (e) Simulated STHM image of T_1 map of the ZnO film, which is superposed on the ZnO model structure. It is simulated with constant tip ZnO distance of 0.93 nm.

The kink-like features of $I(z)$ and $\Delta f(z)$ are reproduced in the simulation as shown in **Figure 4.16**, which result from the relaxation of the two H_2 around a tip height of 0.9 nm. This height is the sum of three equilibrium distances of d_n at which the interactions in the junction start to displace the H_2. The STHM image is also simulated by scanning the tip laterally over the model ZnO surface. The simulated map of T_1 is superposed on the ZnO structure in **Figure 4.16b**, which exhibits the similar contrast as experiment and the atom positions appear as a protrusion.

Figure 4.17 shows the 3D images of the simulated tunneling maps of T_1, T_2, T_3 and T. T_2 and T maps have an opposite contrast to T_1 and T_2 in which appears protrusion at hollow sites. This result suggests that the tunneling probability is dominated by T_1 and/or T_3 reproduces the similar contrast with experiment. The total tunneling probability is sensitive to the value of β_n and thus the simulated images, while we used β_n = 1 Å^{-1} in the simulation as mentioned above. A stronger interaction between the H_2 and the metal tip or the ZnO layer is expected, which leads to a narrower barrier between them than that between two H_2. The narrower barrier is more sensitive to the subtle displacement of the H_2. Also, there should be multiple H_2 on ZnO underneath the tip and electron tunneling would happen between H_2 on the tip apex and multiple H_2 on ZnO, which smears out the contrast of T_2.

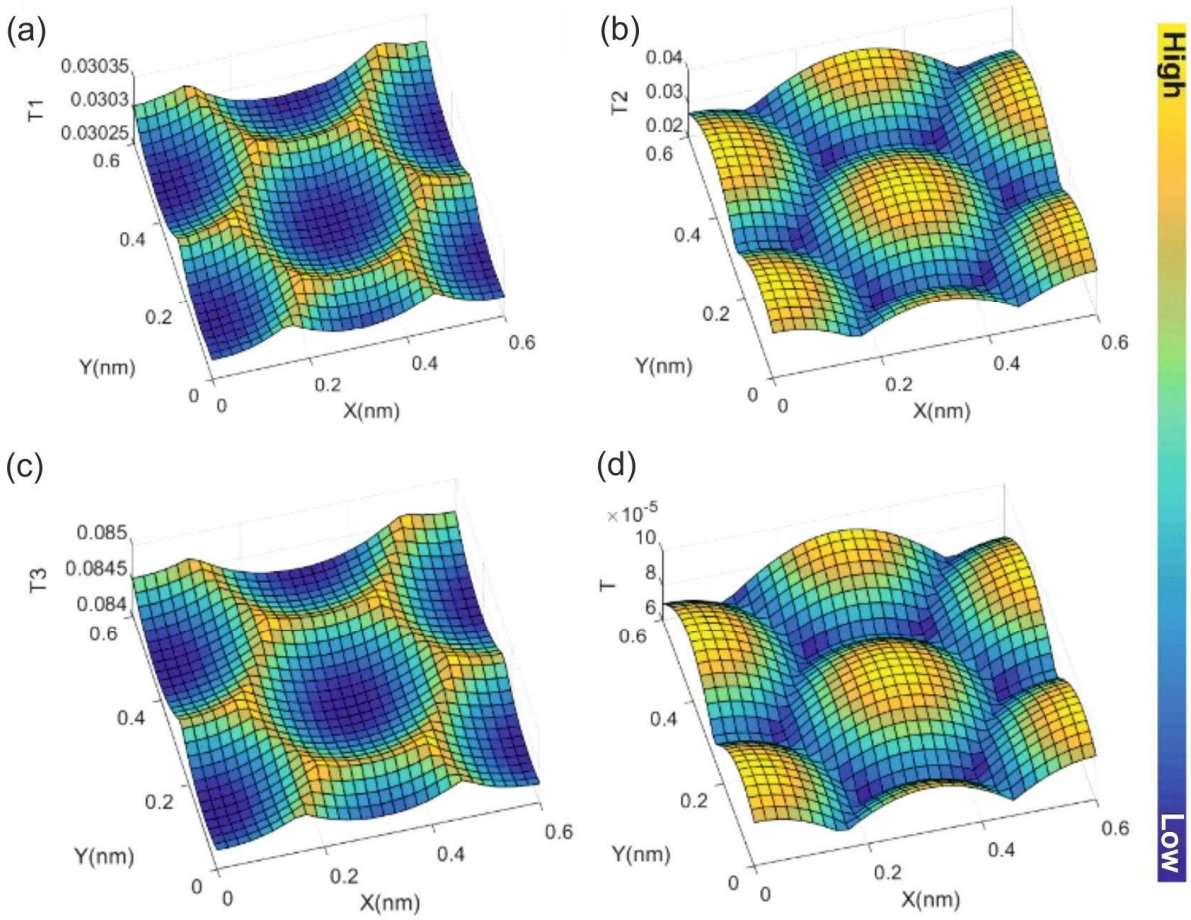

Figure 4.17. (a)-(d) Simulated maps of T_1, T_2, T_3, and T, respectively. As discussed in the main text that the contrast is largely affected by the values of βn, which was fixed β_n = 1 Å in the simulation.

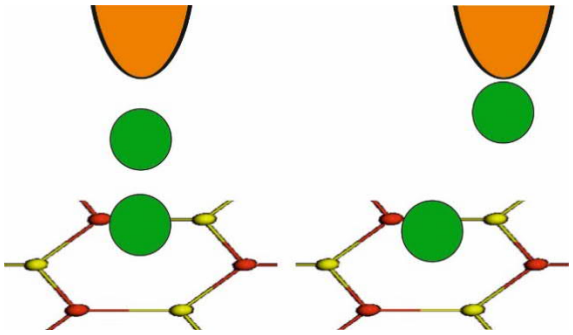

Figure 4.18. Schematic of the STM junction with two H_2 inside of tip located over the hollow (left image) or atom (right image) positions. The H_2 on the tip and ZnO surface are move closer to the tip apex and ZnO, respectively.

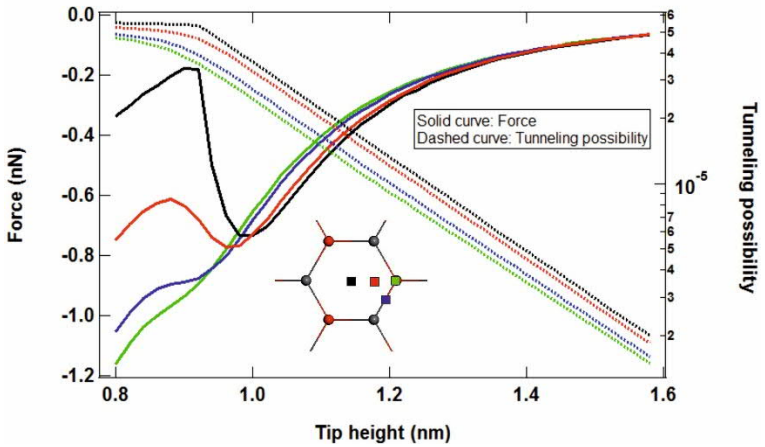

Figure 4.19. Simulated vertical force for the tip (perpendicular to the ZnO surface) and the total tunneling probability (T) at different tip-ZnO distances and at different lateral tip positions. The color squares mark the corresponded tip positions in the inset.

The displacement of the H_2 inside the junction results in the contrast of T_n maps. In the model, the H_2 molecule on ZnO prefers to adsorb on the hollow site, which is similar as H_2 on graphene [204, 205]. In this situation, the distance between two H_2 is larger when the tip is located above the atom position of ZnO as illustrated in **Figure 4.18**. Thus, the attractive force between them would become weaker, forcing the H_2 on tip apex to move closer to the tip, and eventually leading to the increase of the tunneling probability between them, *i.e.*, the protrusion appearance of T_1 at atom positions. The scanning process at a tip height around the kink

positions accompanied with the relaxation of two H_2, which modifies the tunneling probability, thus resulting in the enhanced resolution imaging. One H_2 will be squeezed outside the junction when the tip height is smaller than the kink position, then the enhancement effect disappears. On the other hand, the interaction between two H_2 is too weak to induce the relaxation of two H_2 at a tip height larger than the kink position, then the enhancement effect will also disappear. The simulated force curves reveal the site dependence as shown in **Figure 4.19**, although it is not observed in experiment. The experimental images (**Figure 4.9**) also do not show a sharp protrusion as simulated. These deviations should be reasonable for this simplified model.

4.2.4 Defective feature of 3-ML ZnO layer

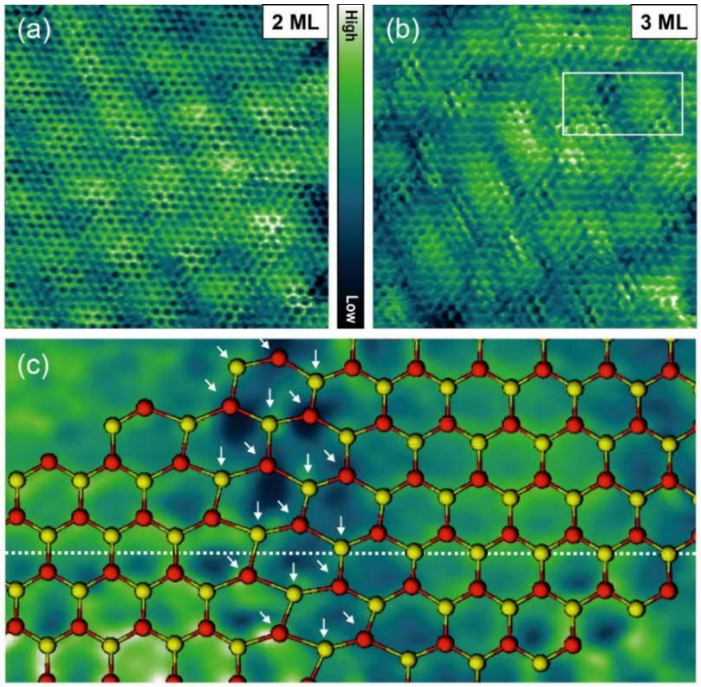

Figure 4.20. (a), (b) STHM images of 2- (5 K, V_s = 0.05 V, I_t = 0.05 nA, 10 × 10 nm^2) and 3-ML ZnO (5 K, V_s = 0.03 V, I_t = 0.03 nA, 10 × 10 nm^2) layer scanned in the constant current mode. (c) Enlarged STHM image of 3-ML ZnO (white box in (b)) which is superimposed with the structure model. The disordered atom positions are marked with arrows and the lattice displacement is emphasized with whited dash line.

The atomic resolution images of STHM reveal a quite uniform structure for 2-ML ZnO (**Figure 4.20a**) but a less ordered structure for 3-ML ZnO (**Figure 4.20b**). **Figure 4.20c** is the enlarged STHM image of 3-ML ZnO that shows dislocation defects with a lattice distortion of ~0.8 Å. The possible distorted honeycomb structure is marked with arrows. The strain resulting from the lattice mismatch of the ZnO layers with the substrate could cause the dislocations [206]. However, considering that there is no dislocation defect in 2-ML ZnO, despite the 2- and 3-ML ZnO have the same lattice parameters, the possibility of the lattice mismatch can be ruled out. As discussed in section 4.1.3, the work function measurement implies a structure change between 2- and 3-ML ZnO. The measured dislocation area may be due to the structure change, for example changed from *h*-BN-like flat structure to a wurtzite-like structure.

4.2.5 Conclusion

The enhanced resolution image of 2- and 3-ML ZnO layers on Ag(111) was obtained by STHM. With a combined STM and AFM measurements, the electronic and mechanical properties of the junction with H_2 inside were also characterized in detail. The conductance and force curves show kink-like features, which are absent in the H_2-free junction. The enhanced resolution imaging was obtained with a relatively large tip sample distance around the specific kink. The junction with multiple H_2 was suggested and a simplified model with two H_2 was used to simulate the experimental observations, which reproduced the kink-like features in conductance and force curves. The contrast of enhanced resolution image is also reproduced, the enhancing mechanism is found due to the relaxation of two trapped H_2 during the scanning process. The dislocation defects of 3-ML ZnO layers was resolved. The results demonstrated that the STHM will be a powerful tool to obtain atomic resolution images for the extended dielectric layers.

5 TERS measurement of ultrathin ZnO layers on Ag(111)

5.1 Introduction

TERS is a powerful analytical tool in nanoscience and nanotechnology and its spatial resolution has recently demonstrated down to sub-nanometer [207, 48]. It also provides a new promising way to deepen our understanding of nanoscale physics and chemistry. We employed TERS to characterize the ZnO layers on Ag(111) surface with our photon-SPM setup. Moreover, as discussed in the introduction of this thesis, there are still outstanding questions to be explored in TERS. Studying a well-defined and a stable system will help to reveal more details of TERS mechanisms. The ZnO layers on Ag(111) surface characterized well by SPM (chapter 3) serves as a good model.

Strong TERS signal of 2-ML ZnO layer on Ag(111) surface was obtained with the spatial resolution of TERS smaller than 1 nm. The enhancement mechanism includes both chemical and physical enhancement mechanisms, revealed by the combined STS, STML and TERS measurements. Different domains of 2-ML ZnO layer were also characterized and the bond strength difference between domains are revealed.

5.2 TERS over ultrathin ZnO layers

Strong TERS signal was obtained for 2-ML ZnO layer measured with He-Ne laser (633 nm) as shown in **Figure 5.1a**. The spectra exhibit characteristic vibrational peaks ranging from 300 to 400 cm^{-1}. The power dependence measurement (the inset of Figure 5.1a) shows a linear dependence, indicating a spontaneous Raman scattering process. The inset of **Figure 5.1a** shows the laser fluence (F) dependence of the TERS intensity (I_R) at 345 cm^{-1}. The data are fitted by the power law dependence $I \propto P^N$, and $N = 0.99 \pm 0.01$ is obtained.

The DFT simulations for free 1-ML ZnO show three branches of optic phonon that correspond to the 2 atoms per unit cell [208]. Two of them are in plane modes that have highest energy at Γ-point and the other is out plane mode. Due to the relative strong interaction between the ZnO layers, the phonon branches split from the 1-ML ZnO [209]. There are nine branches optic phonon for 2-ML ZnO layers correspond to the 4 atoms per unit cell. Compare to a free standing ZnO layer, the symmetry of 2-ML ZnO is reduced after adsorbed on Ag(111), so that

more than nine branches of phonon would potentially appear. Which would result in additional peaks in the Raman spectrum. The spectra can be fitted fairly well with Lorentzian functions with a cubic curve background as shown in **Figure 5.1b**. The intense peaks at 321 cm^{-1}, 326 cm^{-1}, 373 cm^{-1} would attributed to the out plane vibrational modes that is perpendicular to the surface, which have the atoms displace parallel to the enhanced field direction, so that can be strongly enhanced [48]. There are also weak peaks around ~250 cm^{-1} and ~550 cm^{-1} that should belong to the in plane modes. The observation is consistent with the tendency of simulation result, that the out plane phonon have relative modest energy compare to other modes [208, 209, 210]. Anyhow, the exact vibrational energy observed experimentally would be different from the simulated amount for free standing ZnO layers. Theoretical simulation shows that the Ag(111) substrate influences the structure of ZnO layers compare to free standing ZnO layers [161], so that influence to the vibrational energy would also be expected that will be discussed more in section 5.4.

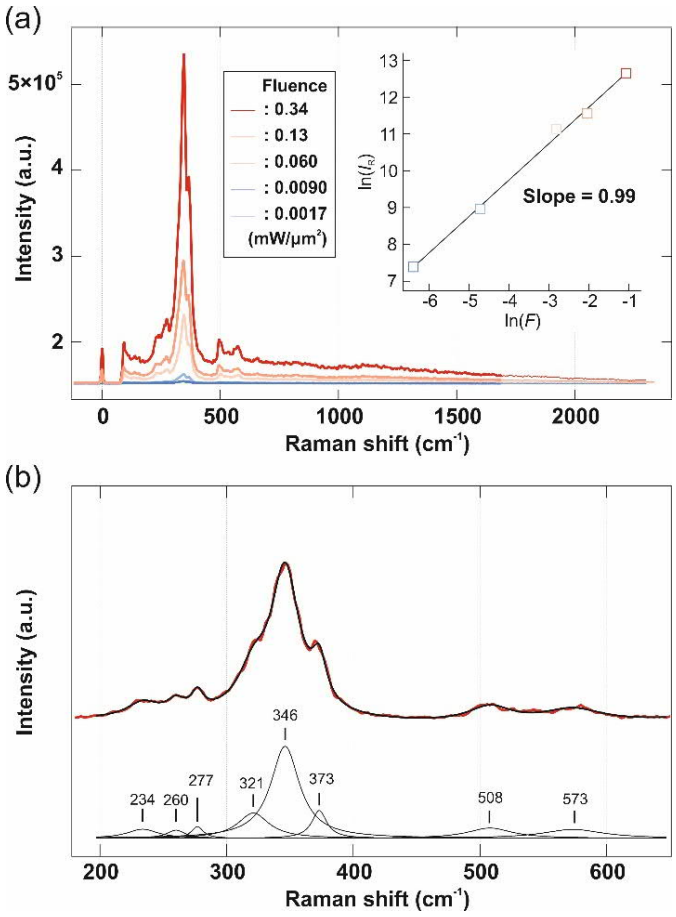

Figure 5.1. (a) TERS spectra of 2-ML ZnO obtained with an Au tip at a different fluence. The tip surface distance was kept with STM feedback loop (V_{bias} = 1 V and

I_t = 1 nA). The laser wavelength was 633 nm. The inset shows the laser fluence (F) dependence of the TERS intensity (IR) at 345 cm^{-1}. The data are fitted by the power raw dependence $I \propto P^N$, and N = 0.99 ± 0.01 is obtained. (b) Multiple peak fitting for TERS spectrum of 2-ML ZnO with Lorentzain peaks. The positions are marked above the fitted peaks.

TERS signal of 3-ML ZnO layer measured with laser wavelength at 633 nm was very weak as compare to the signal of 2-ML ZnO (**Figure 5.2a**). The spectra were recorded under the same measurement conditions (the same tip and the alignment). This strong excitation wavelength dependence can be attributed to the chemical resonance effect, as further discussed in next section. On the other hand, the strong TERS signal of 3-ML ZnO in **Figure 5.2a** can be obtained with laser wavelength 780 nm, which shows obviously different from the spectrum of 2-ML ZnO. The difference here is consistent with the observation of the local work function measurement and atomic resolution imaging as discussed in chapter 4, which all indicate a phase transition between 2- and 3-ML ZnO layers.

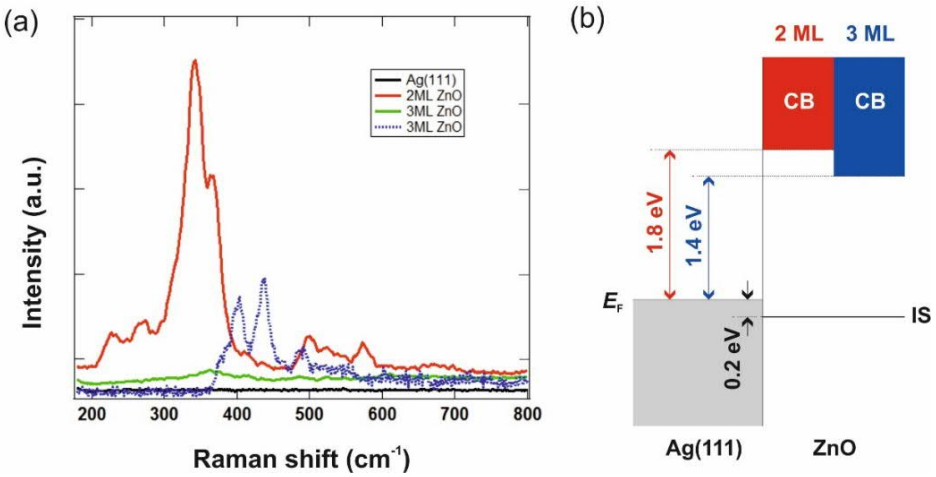

Figure 5.2. (a) TERS spectrum measured over Ag, 2-ML and 3-ML ZnO, respectively. The solid spectra are measured with laser wavelength 633 nm and the dashed one is measured with laser wavelength 780 nm. The cut off at ~370 cm^{-1} in the dashed spectrum is due to the cut off of bandpass filter in the measurement. The tip surface distance was kept with the STM feedback with setpoint 1 V, 1 nA. (b) Energy diagram of the ZnO/Ag(111) system.

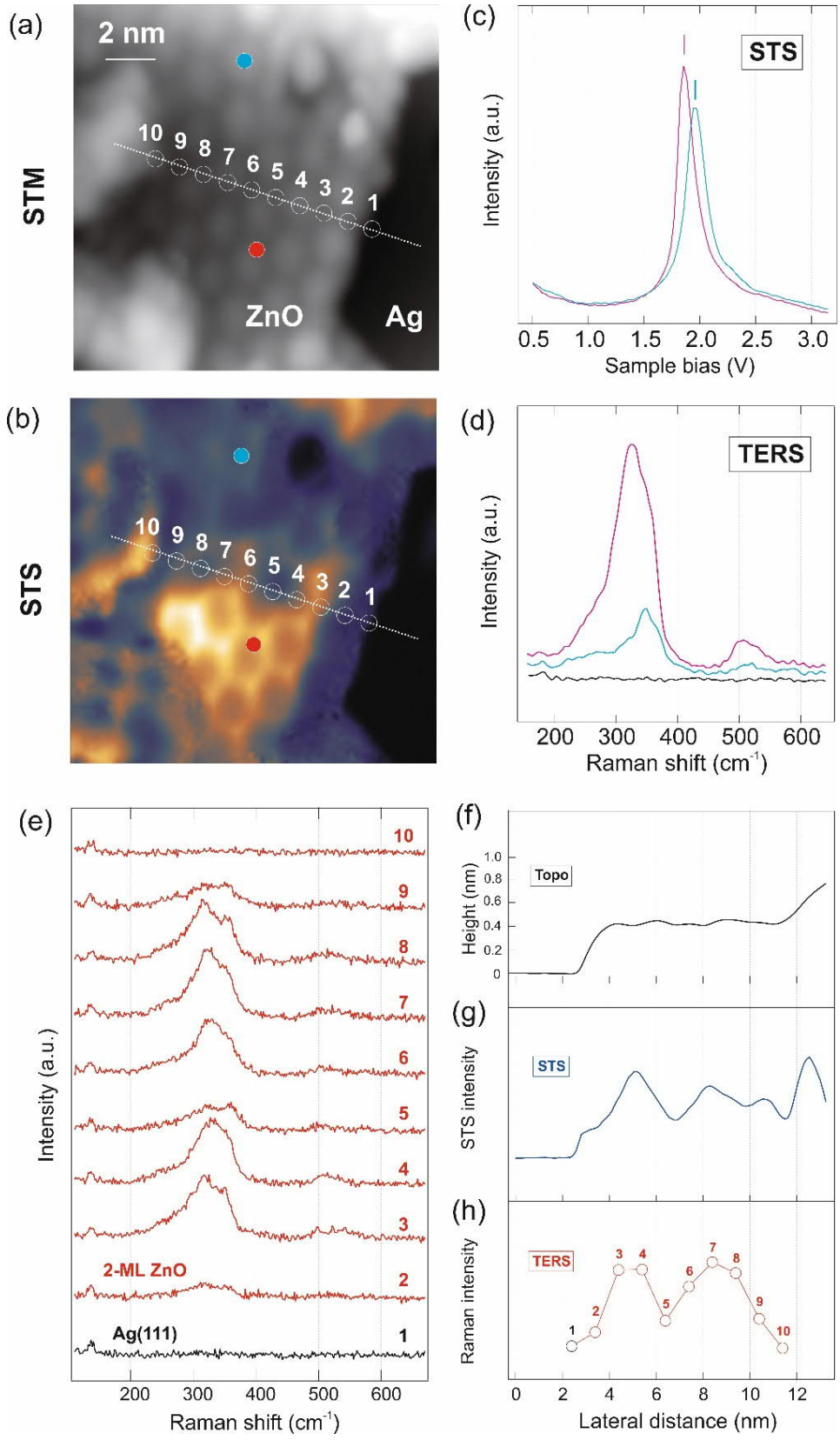

Figure 5.3. (a) (b) STM image and STS map measured simultaneously over 2-ML ZnO. (V_{bias} = 1.8 V and I_t = 1 nA) (c) STS spectrum measured with constant current

(I_t = 500 pA) mode over the two different ZnO positions. The red (blue) one was measured over red (blue) circle position in (a) and (b). (d) TERS spectrum measured over two different positions of 2-ML ZnO. The red (blue) curve is measured over red (blue) circle position in (a) and (b). The black curve is measured over Ag(111) with the same tip. (e) TERS spectrum measured at different positions that are marked by the numbers in (a) and (b). The tip heights are kept with the same STM feedback parameters (V_{bias} = 1V, I_t = 1nA). (f) Profiles of the topographic height along the white line in image (a). (g) Profiles of the STS map along the white line in image (b). (h) Intensity profiles at 325 cm^{-1} of the TERS spectrum in (e).

Figure 5.2b is schematic energy diagram of the ZnO/Ag(111) system determined from the STS measurement in section 4.2. The onset of empty states are ~1.8 eV and ~1.4 eV above the Fermi energy for 2- and 3-ML ZnO layers, respectively. The interface state is ~0.2 eV below the Fermi level. Optical excitation from the interface state to the conduction band minimum of 2-ML ZnO layer would be expected for 633-nm excitation since the photon energy of 1.96 eV nicely matches the energy difference. But this resonant condition is not satisfied for 3-ML ZnO layer due to the lower conduction band minimum. Therefore, the TERS signal is much stronger for 2-ML ZnO than 3-ML with with 633-nm excitation. While the resonant condition is satisfied by changing laser wavelength to 780 nm that leads to the strong TERS signal for 3-ML ZnO. This chemical enhancement mechanism can also explain the absence of TERS signal for both 2- and 3-ML ZnO layers with 532-nm excitation.

5.3 Enhancement mechanism of TERS

Figures 5.3a and **5.3b** are the STM image and the STS map recorded simultaneously with $V_s = 1.8\ V$ (corresponding to the conduction band minimum of 2-ML ZnO layer). The clean Ag(111) surface and the 2-ML ZnO layer with defects are involved in the images. The LDOS of 2-ML ZnO layer are modulated possibly due to the size effect that the possible surrounded defects would confine the electrons [211, 212, 213]. The STS map shows an obvious contrast that the measured LDOS at the lower-half area is larger than the upper-half area, although the STM image do not show obvious differences in both areas. However, the STS spectra measured over two points in these areas revealed the slight shift of the conduction band minimum as shown in

Figure 5.3c. The TERS intensity is much stronger at the region where the LDOS is higher (**Figure 5.3d**). The correlation between the local electronic state and TERS intensity further proves the chemical enhancement mechanism.

Figure 5.3e is TERS spectra measured along the white dashed line in STM (STS) image of **Figure 5.3a** (**b**), where the numbers mark the measured positions. **Figures 5.3f** and **g** are the line profile of the topographic and STS data, respectively. **Figure 5.3h** is the TERS intensity profile of the Raman shift at 350 cm^{-1}. The STS and TERS profiles show significant modulation, albeit the topographic height is relatively featureless. The modulation also shows correlation that a higher LDOS result in a larger TERS signal. The spatial resolution can be estimated to be smaller than 1 nm.

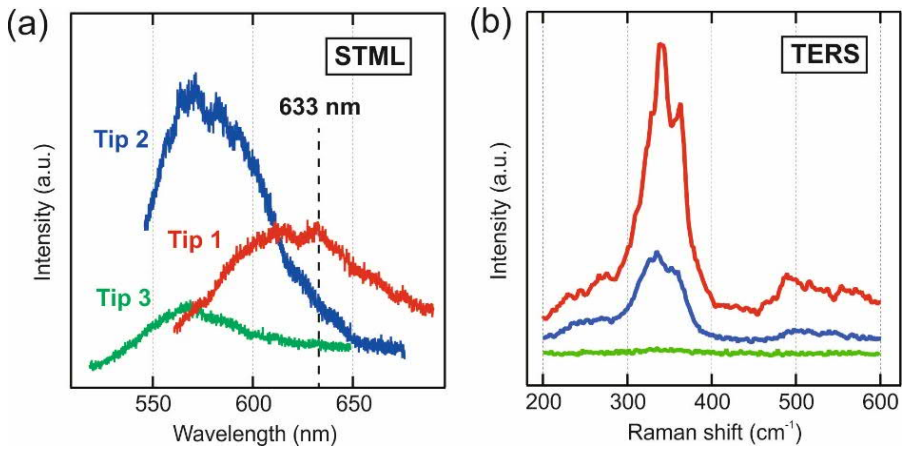

Figure 5.4. (a) STML spectra obtained with an Au tip of three different conditions (see main text). The spectra were recorded on the Ag(111) surface at V_{bias} = 2.5 V and I_t = 1 nA. (b) TERS spectra obtained under the three different tip conditions in (a). The tip-surface distance was kept with the feedback loop at V_{bias} = 1 V and I_t = 1 nA. The excitation wavelength was 633 nm with an incident power density of 0.34 mW/μm^2.

The electromagnetic enhancement (physical resonance mechanism) requires spectral matching of the incident and scattering light with LSPR in the junction. Therefore, TERS signals are, in general, very sensitive to the tip conditions. The STM-induced luminescence (STML), resulting from inelastic scattering of tunneling electrons [214], can be used to characterize the plasmon properties in the junction. **Figure 5.4** shows the correlation between

the STML and TERS intensity. **Figure 5.4a** displays the STML spectra obtained under three different tip conditions. The tip conditions can be modified by applying a voltage pulse between the tip and sample or colliding tip to the clean surface in a controlled manner. Although the STM images obtained with these tips were similar, the STML signals that show LSPR in the junction are very different. This observation is consistent with the previous studies showing that the STML spectra are sensitive to the tip shape [215]. **Figure 5.4b** is the TERS spectra measured under these three different conditions over 2-ML ZnO layer, otherwise the same measurement parameters (the same position, power of incident laser, and alignment). Similar to the previous study [48], the TERS intensity is related to the plasmonic intensity around 630 nm. The tip with higher STML intensity there lead to a higher TERS signal.

5.4 Interaction between ZnO layer and Ag(111)

With the high resolution TERS, the correlation between the geometry, electronic structure, and the vibrational property of 2-ML ZnO layers can be studied. In **Figure 5.5a**, three different domains with different adsorption geometries relative to the underneath Ag(111) surface are observed and the Moiré patterns exhibit different orientations. **Figures 5.5b** and **c** show the STS and TERS spectra, respectively, for these three domains. The domain of orientation (ii) in **Figure 5.5a** is the ZnO(0001)-(7×7)/Ag(111)-(8×8) coincidence structure that is the major orientation. The orientation (i) and (iii) is rotated 15° and 25° from it.

As discussed in **Figure 5.3**, the TERS intensity is influenced by the position of the conduction band minimum. It was found that the intensity is stronger when the conduction band minimum becomes closer to the Fermi level of the Ag substrate. The shift of the FER peaks indicates a change in the local work function as discussed in Chapter 4. We also expect that the shift of the conduction band minimum is associated with the local work function change because it shifts together with the FER in the STS spectra. As discussed in section 4.1, there are three reasons that would result in the change of the work function. The work function reduction here could be explained by the partial charge transfer from 2-ML ZnO layer to the Ag(111) substrate. Although there is no direct evidence showing the charge transfer and covalent bond formation between the ZnO layer and the Ag(111) substrate in DFT simulation [216] the hybridization between their electronic bands could still occur when both momentum and energy are matched. The partial charge transfer will also reduce the bond strength of ZnO layer [217].

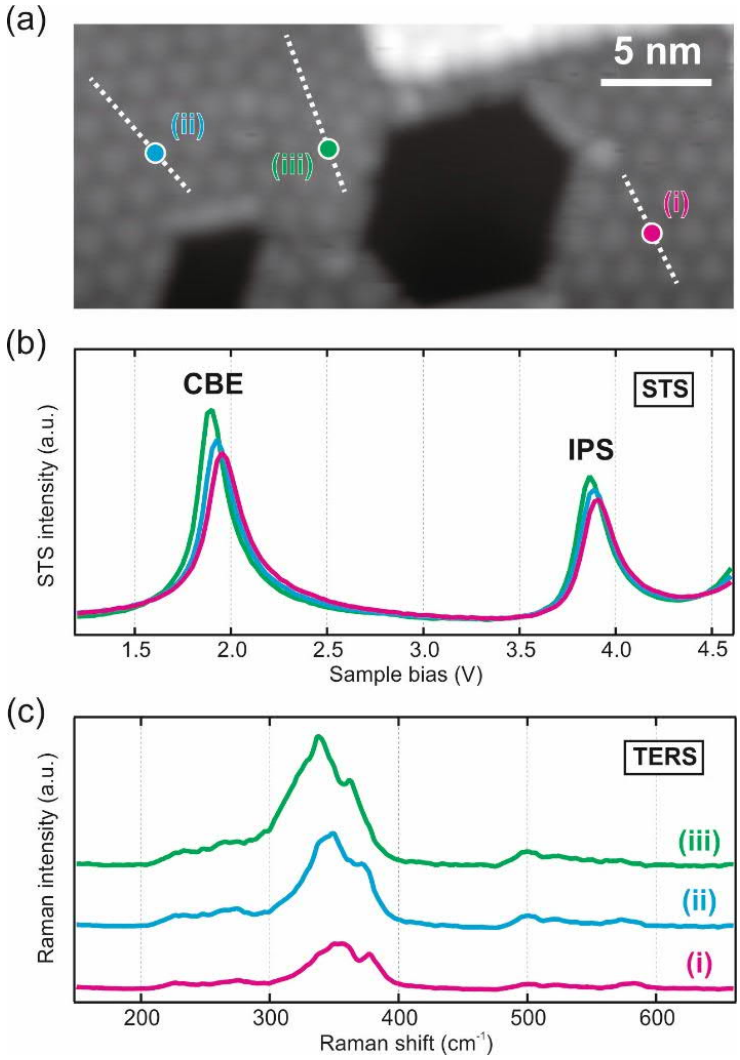

Figure 5.5. (a) STM image of 2-ML ZnO contained three different domains. The white dash lines indicate different orientations of a Moiré pattern. (b) and (c) Constant current (I_t = 1 nA) STS spectra and TERS spectra of three different domains. The measured positions are marked with circles in (a), which have the same color as the spectra. The excitation wavelength was 633 nm at an incident power density of 0.39 mW/μm^2 .

5.3 Conclusions

TERS was measured for 2- and 3-ML ZnO layers on Ag(111). The position dependent measurement of TER spectra shows a spatial resolution smaller than 1 nm. The incident laser power dependence clearly indicates that TER process occurs via a spontaneous Raman process. In TER spectra, characteristic peaks of the ultrathin ZnO layers and the vibrational energy of

the TO and LO modes were found to be significantly red-shifted as compared to those in the bulk. Interactions between 2-ML ZnO layer and Ag(111) substrate are discussed according to the measured STS and TERS spectra.

The origin of the enhancement mechanism was clearly demonstrated and involve both chemical and physical enhancement process. It was found that the excitation wavelength needs to be resonant with both the electronic resonance of the ZnO/Ag(111) complex and LSPR of the junction. Strong TERS signals were observed for 2- and 3-ML ZnO for excitation wavelength of 633- and 780-nm, respectively, which match the electronic resonance between the conduction band minimum of the ZnO layers and the interface state close to the Fermi level. Furthermore, by combining TERS with STS measurements, it was revealed that the TERS intensity is strongly influenced by the local changes of electronic structure, being in good agreement with a chemical enhancement mechanism. The physical enhancement mechanism was also examined by comparing STML spectra to TERS intensity for different tip conditions.

6 Summary and outlook

As discussed in the introduction, photon-SPM is a promising approach to study light–matter interactions at the nanometer scale, which is interesting for fundamental science and may potentially leads to new technologies. This thesis describes the development and capabilities of a low-temperature photon-SPM which combines a parabolic mirror and a lens on a cold SPM stage. The *in-situ* optics can be precisely aligned by multi-axis motion using piezo motors. Our setup offers high-quality and convenient aligning procedure to perform highly reliable and reproducible experiments. As a demonstration of nanoscale microspectroscopy, TERS was applied to investigate the ultrathin ZnO layers epitaxially grown on Ag(111) surface, which serves as a well defined model system.

The low-temperature photon-SPM also provides a unique opportunity to study near-field-driven processes in a nanoscale cavity. We demonstrated plasmon-assisted resonant electron tunneling from a plasmonic tip to FERs over both Ag(111) and ZnO layers by CW laser excitation. A pronounced downshift equal to the incident photon energy was found for the first peak in FER spectra under illumination. Higher order peaks in FER spectra are also downshifted under illumination, which are proved in combination with the STS mapping. The combined STML spectra, laser polarization and tip material dependence measurements clearly show that the process is associated with LSPR excitation in the junction. In the laser power and tip–surface distance dependent measurements, the preference of the two tunneling processes (direct and plasmon assisted) can be tuned. This FERs in a STM junction provide a simple model to examine resonant electron transfer in a plasmonic nanocavity. The observed plasmon assisted tunneling process also provide a very useful criteria for the alignment quality of the setup.

Local structural modifications play a critical role for material properties. As the properties of ultrathin oxide films vary depending on the number of layers, the ZnO layers should be characterized locally as a function of thickness. The local electronic structure and work function of 2-4 ML ZnO layers were investigated by a combination of STM and AFM at 5 K. The conduction band minimums were found monotonically downshift as well as the local work function monotonically decreased with increasing the thickness. This trend of local work function reduction is also verified by the CPD measurement. The local work function is largely reduced from 2- to 3-ML ZnO layers, which suggests a structural change from a *h*-BN-like flat geometry to a bulk-like Wurtzite structure. This structure change is expected to modify the

interaction between ZnO layers and Ag(111) substrate, leading to the dramtic work function change. The structure change is also implied by atomic resolution STHM imaging in which 3-ML ZnO layers exhibit dislocation defects. The interaction between ZnO layers and the Ag(111) substrate also leads to a slightly different orientation of the ZnO layer relative to the Ag surface. It was shown that such a subtle difference can have a substantial impact in TERS scattering mediated by a slight shift of the conduction band minimum of the ZnO layer. Spatial variation at the nanometer scale for the conduction band minimum and the local work function change were also visualized by the STS mapping for the ZnO layers on the Ag(111) surface. A possible defect buried inside the sample was also visualized in the STS map. These local measurements deepen our understanding of the ZnO layers on Ag(111) substrate.

So far, the STHM has been used to imaging planar organic molecules at most case, we extend it to imaging the two dimensional material ZnO layers in this thesis. Atomic resolution images of 2- and 3-ML ZnO layers were obtained, which could never been resolved in normal STM. In previous studies, single H_2 was trapped inside the STM junction whereby Pauli repulsion leads to enhanced spatial resolution. But in our case, the enhanced resolution was obtained at a large and specific tip surface distance where Pauli repulsion is negligible. The tip–surface distance dependent conductance curves and frequency shift curves both show kink like features at the same tip surface distance, which are absent in a junction without H_2. The best resolution was obtained at this specific tip–surface distance of the kink-like feature. For a junction containing multiple H_2 it was proposed that the kink-like feature in the conductance curves and frequency shift curves arise from sequentially squeezing H_2 outside the junction. Simulations for a simplified model containing two H_2 reproduce the experimental observation qualitatively. In this simulation, the spatial enhancement correlates with the relaxation of the two H_2 around equilibrium distances. This new STHM process demonstrate that STHM will be a powerful tool to resolve atomic resolution for two dimensional extended structures.

As a powerful analytical tool in nanoscience and nanotechnology, TERS has attracted increasing attention. Low-temperature photon-SPM is ideal for TERS measurements. We observe a strong TERS signal for 2-ML ZnO layers with a spatial resolution smaller than 1 nm. A spontaneous Raman scattering was indicated from the incident laser power dependent measuring, which suggest that the high resolution results directly from a highly localized field in the junction. The observation of strong TERS signals for 2- and 3-ML ZnO at 633- and 780-nm excitation, respectively, is consistent with a chemical enhancement mechanism, whereby the photon energies match well with the excitation energy from interface state to the conduction

band minimum. The TERS signal is therefore also sensitive to the position of the conduction band minimum. Combined measurements of STML and TERS spectra also proved the crucial role of the physical enhancement mechanism that the incident photon energy needs to match LSPR in the junction. These observations help extending TERS measurements to other samples, also providing plasmonic information on nanocavities.

Summary the discussion above, also together with previous studies, this thesis demonstrates the promising capabilities of photon-SPM to investigate light-matter interaction at nanoscale. Typical measurements of photon-SPM like STML and TERS would potentially extended to other samples, which would deepen our understanding of materials, chemical reactions at molecular scale. As STM is an ideal tool to study the transmission behavior of atomic sized contacts [218], photon-SPM can be used to characterizing structure of the contacts by Raman scattering spectroscopy and studying the transmission behavior under illumination. The photon-SPM allows precise control of the size of a nanocavity (tip surface distance) in the tunneling regime, where quantum effect play a crucial role for the near field properties [219]. Detailed studies of the quantum plasmonics are in reach with photon-SPM. Moreover, combining photon-SPM with ultra-short laser pulses make time-resolved local optical spectroscopy feasible, i.e. ultrafast dynamical could be resolved at the nanometer scale. This is a long standing dream of physical chemistry.

Bibliography

[1] W. E. Moerner, Nobel lecture: Single-molecule spectroscopy, imaging, and photocontrol: foundations for super-resolution microscopy. Rev. Mod. Phys. **87**, 1183−1212 (2015).

[2] G. Lozano, D. Louwers, J. S. R. K. Rodriguez, S. Murai, O. T. A. Jansen, M. A. Verschuuren, J. G. Rivas, Plasmonics for solid-state lighting: enhanced excitation and directional emission of highly efficient light sources. Light. Sci. Appl. **2**, e66 (2013).

[3] J. Wallentin, *et al*. InP nanowire array solar cells achieving 13.8% efficiency by exceeding the ray optics limit. Science **339**, 1057–1060 (2013).

[4] J. N. Anker, *et al*. Biosensing with plasmonic nanosensors. Nature Mater. **7**, 442453 (2008).

[5] H. A. Atwater, A. Polman, Plasmonics for improved photovoltaic devices. Nature Mater. **9**, 205–213 (2010).

[6] S. Linic, P. Christopher, D. B. Ingram, Plasmonic-metal nanostructures for efficient conversion of solar to chemical energy. Nat. Mater. **10**, 911–921 (2011).

[7] V. Giannini, A. I. Fernández-Domínguez, S. C. Heck, S. A. Maier, Plasmonic nanoantennas: fundamentals and their use in controlling the radiative properties of nanoemitters. Chem. Rev. **111**, 3888–3912 (2011).

[8] S. Nie, S. R. Emory, Probing single molecules and single nanoparticles by surface-enhanced Raman scattering. *Science* **275**, 1102–1106 (1997).

[9] M. Fleischman, P. J. Hendra, A. J. McQuillan. Raman spectra of pyridine adsorbed at a silver electrode. Chem. Phys. Lett. **26**, 123 (1974).

[10] D. L. Jeanmaire, R. P. Van Duyne. Surface raman spectroelectrochemistry: Part I. Heterocyclic, aromatic, and aliphatic amines adsorbed on the anodized silver electrode J. Electroanal. Chem. **84**, 1 (1977).

[11] M. G. Albrecht, J. A. Creighton. Anomalously intense Raman spectra of pyridine at a silver electrode. J. Am. Chem. Soc. **99**, 5215 (1977).

[12] M. Moskovits. Surface roughness and the enhanced intensity of Raman scattering by molecules adsorbed on metals. J. Chem. Phys. **69**, 4159 (1978).

[13] M. S. Anderson, Locally enhanced Raman spectroscopy with an atomic force microscope. Appl. Phys. Lett. **76**, 3130−3132 (2000).

[14] N. Hayazawa, Y. Inouye, Z. Sekkat, S. Kawata, Near-field optics and surface plasmon polaritons. Opt. Commun. **183**, 333−336 (2000).

[15] Pettinger, B., Picardi, G., Schuster, R., Ertl, G. Surface enhanced Raman spectroscopy: towards single Moleculer spectroscopy. Electrochemistry **68**, 942−949 (2000).

[16] R. M. Stockle, Y. D. Suh, V. Deckert, R. Zenobi, Nanoscale chemical analysis by tip-enhanced Raman spectroscopy. Chem. Phys. Lett. **318**, 131−136 (2000).

[17] Binnig G., Rohrer H., Gerber C., Weibel E. Surface studies by scanning tunneling microscopy Phys. Rev. Lett. **49** 57–61 (1982).

[18] G. Binnig, C. F. Quate, Atomic force microscope Phys. Rev. Lett. **56**, 930-3 (1986).

[19] R. J. Hamers, R. M. Tromp, J. E. Demuth, Surface electronic structure of Si (111)-(7×7) Resolved in Real Space. Phys. Rev. Lett. **56**, 1972-1975 (1986).

[20] R. M. Feenstra, Scanning tunneling spectroscopy. Surface Science, **299-300**, 965-979 (1994).

[21] B. C. Stipe, M. A. Rezaei, W. Ho. Single-molecule vibrational spectroscopy and microscopy. Science, **280**, 1732–1735, (1998).

[22] Y. Sainoo et al., Excitation of molecular vibrational modes with inelastic scanning tunneling microscopy processes: examination through action spectra of cis-2-Butene on Pd(110). Phys. Rev. Lett. **95**, 246102 (2005).

[23] S. Kitamura, M. Iwatsuki, High-resolution imaging of contact potential difference with ultrahigh-vacuum noncontact atomic force microscopy. Appl. Phys. Lett. **72**, 3154–3156 (1998).

[24] D. M. Eigler, E. K. Schweizer, Positioning single atoms with a scanning tunnelling microscope. Nature, **344,** 524–526, 1990.

[25] M. F. Crommie, C. P. Lutz, D. M. Eigler, Confinement of electrons to quantum corrals on a metal surface. Science, **262**, 218–220, 1993.

[26] C. Zhang, L. Chen, R. Zhang, Z. C. Dong, Scanning tunneling microscope based nanoscale optical imaging of molecules on surfaces. Jpn. J. Appl. Phys. **54**, 08LA01 (2015).

[27] K. Kuhnke, C. Große, P. Merino, K. Kern. Atomic-scale imaging and spectroscopy of electroluminescence at molecular interfaces. Chem. Rev. **117**, 5174 (2017).

[28] X. H. Qiu, G. V. Nazin, W. Ho, Vibrationally resolved fluorescence excited with submolecular precision. Science **299**, 542−546 (2003).

[29] H. Imada, K. Miwa, M. Imai-Imada, S. Kawahara, K. Kimura, Y. Kim, Single-molecule investigation of energy dynamics in a coupled plasmon-exciton system. Phys. Rev. Lett. **119**, 013901 (2017).

[30] B. Doppagne, M. C. Chong, E. Lorchat, S. Berciaud, M. Romeo, H. Bulou, A. Boeglin, F. Scheurer, G. Schull, Vibronic Spectroscopy with submolecular resolution from STM-induced electroluminescence. Phys. Rev. Lett. **118**, 127401 (2017).

[31] Y. Zhang, Y. Luo, Y. Zhang, Y.-J. Yu, Y.-M. Kuang, L. Zhang, Q.-S. Meng, Y. Luo, J.-L. Yang, Z.-C. Dong, Visualizing coherent intermolecular dipole−dipole coupling in real space. Nature **531**, 623−627 (2016).

[32] H. Imada, K. Miwa, M. Imai-Imada, S. Kawahara, K. Kimura, Y. Kim, Real-space investigation of energy transfer in heterogeneous molecular dimers. Nature **538**, 364–367 (2016).

[33] S. Raza, S. Kadkhodazadeh, T. Christensen, M. Di Vece, M. Wubs, N. A. Mortensen, and N. Stenger, Multipole plasmons and their disappearance in few-nanometre silver nanoparticles. Nat. Commun. **6**, 8788 (2015)

[34] M. L. Brongersma, N. J. Halas, and P. Nordlander, Plasmon-induced hot carrier science and technology, Nat. Nanotechnol.**10** , 25 (2015).

[35] Stöckle, R. M., Suh, Y. D., Deckert, V. & Zenobi, R.Nanoscale chemical analysis by tip-enhanced Raman spectroscopy. Chem. Phys. Lett. **318**, 131–136 (2000).

[36] M. S. Anderson, Locally enhanced Raman spectroscopy with an atomic force microscope. Appl. Phys. Lett. **76**, 3130–3132 (2000).

[37] N. Hayazawa, Y. Inouye, Z. Sekkat, S. Kawata, Metallized tip amplification of near-field Raman scattering. Opt. Commun. **183**, 333–336 (2000).

[38] B. Pettinger, Single-molecule surface- and tip-enhanced Raman spectroscopy. *Mol. Phys.* **108** 2039–59 (2010).

[39] X. Wang, S.-C. Huang, T.-X. Huang, H.-S. Su, J.-H. Zhong, Z.-C. Zeng, M.-H. Li, B. Ren, Tip-enhanced Raman spectroscopy for surfaces and interfaces. Chem. Soc. Rev. **46**, 4020–4041 (2017).

[40] S.-Y. Ding, J. Yi, J.-F. Li, B. Ren, D.-Y. Wu, R. Panneerselvam, Z.-Q. Tian, Nanostructure-based plasmon-enhanced Raman spectroscopy for surface analysis of materials. Nat. Rev. Mater. **1**, 16021 (2016).

[41] Z. L. Zhang, S. X. Sheng, R. M. Wang, M. T. Sun, Tip-enhanced Raman spectroscopy. Anal. Chem. **88**, 9328–9346 (2016).

[42] N. Anderson, A. Hartschuh, S. Cronin, L. Novotny, Nanoscale vibrational analysis of single-walled carbon nanotubes. J. Am. Chem. Soc. **127**, 2533–2537 (2005).

[43] T. Ichimura, *et al.* Subnanometric near-field Raman investigation in vicinity of a metallic nanostructure. Phys. Rev. Lett. **102**, 186101 (2009).

[44] J. Steidtner, B. Pettinger, Tip-Enhanced Raman Spectroscopy and Microscopy on Single Dye Molecules with 15 nm Resolution. Phys. Rev. Lett. **100**, 236101 (2008).

[45] J. Stadler, T. Schmid, R. Zenobi, Nanoscale chemical imaging using topillumination tip-enhanced Raman spectroscopy. Nano Lett. **10**, 4514–4520 (2010).

[46] T. Yano, P. Verma, Y. Saito, T. Ichimura, S. Kawata, Pressure-assisted tipenhanced Raman imaging at a resolution of a few nanometres. Nature Photon. **3**, 473–477 (2009).

[4747] R. Treffer, X. M. Lin, E. Bailo, T. Deckert-Gaudig, V. Deckert, Distinction of nucleobases-a tip-enhanced Raman approach. Beilstein J. Nanotechnol **2**, 628–637 (2011).

[48] R. Zhang, Y. Zhang, Z. C. Dong, S. Jiang, C. Zhang, L. G. Chen, L. Zhang, Y. Liao, J. Aizpurua, Y. Luo, J. L. Yang, J. G. Hou, Chemical mapping of a single molecule by plasmon-enhanced Raman scattering. *Nature* **498**, 82-86 (2013).

[49] W. Zhu, R. Esteban, A. G. Borisov, J. J. Baumberg, P. Nordlander, H. J. Lezec, J. Aizpurua, K. B. Crozier, Quantum mechanical effects in plasmonic structures with subnanometre gaps Nat. Commun. **7**, 11495 (2016)

[50] F. Benz, M. K. Schmidt, A. Dreismann, R. Chikkaraddy, Y. Zhang, A. Demetriadou, C. Carnegie, H. Ohadi, B. de Nijs, R. Esteban, J. Aizpurua, J. J. Baumberg, Single-molecule optomechanics in "picocavities". Science **354** 726–729 (2016).

[51] M. Barbry, P. Koval, F. Marchesin, R. Esteban, A.G. Borisov, J. Aizpurua, D. San chez-Portal, Atomistic near-field nanoplasmonics: reaching atomic-scale resolution in nanooptics. Nano Lett. **15**, 3410−3419 (2015).

[52] M. Takase, H. Ajiki, Y. Mizumoto, K. Komeda, M. Nara, H. Nabika, S. Yasuda, H. Ishihara, K. Murakoshi, Selection-rule breakdown in plasmon-enduced electronic excitation of an isolated single-walled carbon nanotube. Nat. Photonics **7**, 550–554 (2013)

[53] D. V. Chulhai, L. Jensen, Determining molecular orientation with surface-enhanced Raman scattering using inhomogenous electric fields J. Phys. Chem. C **117**, 19622–19631 (2013)

[54] M. Moskovits, J. S. Suh, Surface selection rules for surface-enhanced Raman spectroscopy: calculations and application to the surface-enhanced Raman spectrum of phthalazine on silver. *J. Phys. Chem.* **88**, 5526 (1984).

[55] M. Vickie, *et al.* Selection rules for surface Raman spectroscopy: Experimental results. J. Chem. Phys. **84**, 2933 (1986)

[56] M. Moskovits, Surface selection rules. J. Chem. Phys. **77**, 4408 (1982)

[57] C. C. Neacsu, J. Dreyer, N. Behr, M. B. Raschke, Scanning-probe Raman spectroscopy with single-molecule sensitivity. Phys. Rev. B **73**, 193406 (2006).

[58] M. D. Sonntag, J. M. Klingsporn, L. K. Garibay, J. M. Roberts, J. A. Dieringer, T. Seideman, K. A. Scheidt, L. Jensen, G. C. Schatz, R. P. Van Duyne, Single-molecule tip-enhanced Raman spectroscopy. J. Phys. Chem. C **116**, 478-483 (2012).

[59] Dong, Z. C. et al. Generation of molecular hot electroluminescence by resonant nano-cavity plasmons. Nature Photon. **4**, 50–54 (2010).

[60] X. Li, D. Xiao, Z. Zhang, Landau damping of quantum plasmons in metal nanostructures. *New J. Phys.* **15**, 023011 (2013).

[61] M. L. Brongersma, N. J. Halas, P. Nordlander, Plasmon-induced hot carrier science and technology. Nat. Nanotechnol. **10**, 25–34 (2015).

[62] S. Linic, U. Aslam, C. Boerigter, M. Morabito, Photochemical transformations on plasmonic metal nanoparticles. Nat. Mater. **14**, 567–576 (2015).

[63] G. Baffou, R. Quidant, Nanoplasmonics for chemistry. Chem. Soc. Rev. 43 3898–907

[64] Zhang, Y.; He, S.; Guo, W.; Hu, Y.; Huang, J.; Mulcahy, J. R.; Wei, W. D. Surface-plasmon-driven hot electron photochemistry. Chem. Rev. **118**, 2927 (2018).

[65] D. B. Ingram, S. Linic, Water splitting on composite plasmonic-metal/semiconductor photoelectrodes: evidence for selective plasmon-induced formation of charge carriers near the semiconductor surface. *J. Am. Chem. Soc.* **133**, 5202-5205 (2011).

[66] P. Christopher, H. Xin, S. Linic, Visible-light-enhanced catalytic oxidation reactions on plasmonic silver nanostructures. *Nat. Chem.* **3**, 467–472 (2011).

[67] S. Linic, U. Aslam, C. Boerigter, M. Morabito, Photochemical transformations on plasmonic metal nanoparticles. *Nat. Mater.* **14**, 567-576 (2015).

[68] Z. W. Liu, W. B. Hou, P. Pavaskar, M. Aykol, S. B. Cronin, Plasmon resonant enhancement of photocatalytic water splitting under visible illumination. Nano Lett. **11**, 1111–1116 (2011).

[69] S. Mukherjee, *et al.* Hot-electron-induced dissociation of H_2 on gold nanoparticles supported on SiO2. J. Am. Chem. Soc. **136**, 64–67 (2014)

[70] U. Aslam, V. G. Rao, S. Chavez, S. Linic, Catalytic conversion of solar to chemical energy on plasmonic metal nanostructures. Nat. Catal. **1**, 656-665 (2018).

[71] H.-J. Freund, G. Pacchioni, Oxide ultra-thin films on metals: new materials for the design of supported metal catalysts. Chem. Soc. Rev. **37** 2224 (2008).

[72] K. Nomura, H. Ohta, K. Ueda, T. Kamiya, M. Hirano, H. Hosono, Thin-film transistor fabricated in single-crystalline transparent oxide semiconductor. Science **300** 1269 (2003).

[73] P. Mitra, A.-P. Chatterjee, H.-S. Maiti, ZnO thin film sensor. Mater. Lett. **35** 33 (1998).

[74] H. J. Freund, The surface science of catalysis and more, using ultrathin oxide films as templates: a perspective. J. Am. Chem. Soc. **138**, 8985 (2016).

[75] S. Shaikhutdinov, H.-J. Freund, Ultrathin Oxide Films on Metal Supports: Structure-Reactivity Relations. Annu. Rev. Phys. Chem. **63** 619 (2012).

[76] S. Schauermann, N. Nilius, S. Shaikhutdinov, H.-J. Freund, Nanoparticles for heterogeneous catalysis: new mechanistic insights. Acc. Chem. Res. **46** 1673 (2013).

[77] H.-J. Freund, Metal-supported ultrathin oxide film systems as designable catalysts and catalyst supports. Surf. Sci. **601** 1438 (2007).

[78] M. Bäumer, H.-J. Freund. Metal deposits on well-ordered oxide films. Prog. Surf. Sci. **61** (1999)

[79] Ü. Özgür, Ya. I. Alivov, C. Liu, A. Teke, M. A. Reshchikov, S. Doğan, V. Avrutin, S. -J. Cho, and H. Morkoç, A comprehensive review of ZnO materials and devices. J. Appl. Phys. 98, 041301 (2005).

[80] U. Diebold, The surface science of titanium dioxide. Surf. Sci. Rep. **48**, 53–229 (2003).

[81] R. Temirov, S. Soubatch, O. Neucheva, A. C. Lassise, and F. S. Tautz, A novel method achieving ultra-high geometrical resolution in scanning tunnelling microscopy. New J. Phys. 10, 053012 (2008).

[82] G. Hapala, C. Kichin, F. Wagner, S. Tautz, R. Temirov, P. Jelínek, Mechanism of high-resolution STM/AFM imaging with functionalized tips. Phys. Rev. B **90**, 085421 (2014).

[83] G. Binnig, H. Rohrer, Ch. Gerber, E. Weibel. Surface studies by scanning tunneling microscopy. Phys. Rev. Lett., **49**, 57–61, 1982.

[84] J. Bardeen, Tunnelling from a Many-Particle Point of View. Phys. Rev. Lett. 6, 57 (1961).

[85] J. Tersoff and D.R. Hamann, Theory and application for the scanning tunneling microscope. Phys. Rev. Lett. **50**, 1998 (1983).

[86] J. Tersoff and D.R. Hamann, Theory of the scanning tunneling microscope. Phys. Rev. B **31**, 805 (1985).

[87] G. Binnig, C. F. Quate, and Ch. Gerber. Atomic force microscope. Phys. Rev. Lett. **56**, 930–933 (1986).

[88] S. Morita, F.-J. Giessibl, R. Wiesendanger. Noncontact atomic force microscopy: Volume 2, pages 121–142. Springer Berlin Heidelberg, Berlin, Heidelberg, (2009).

[89] F.-J. Giessibl, German Patent p. DE 196 33 546 (1996)

[90] F.-J. Giessibl. Forces and frequency shifts in atomic-resolution dynamic-force microscopy. Phys. Rev. B, **56**, 16010–16015, 1997.

[91] J.-E. Sader, S.-P. Jarvis. Accurate formulas for interaction force and energy in frequency modulation force spectroscopy. App. Phys. Lett., **84**, 10, (2004).

[92] D. A. Long, Introductory Raman spectroscopy. academic press, amsterdam, second edition, (2003).

[93] G. Placzek, Rayleigh-streuung und Raman-effekt, in: E. Marx, Handbuch der Radiologie, Akademische Verlagsgesellschaft, Leipzig, Vol. 6, Part 2 (1934).

[94] C. Eric, *et al.* Direct measurement of resonance Raman spectra and cross sections by a polarization difference technique. Analytical chemistry, **84**, 5074–9, (2012).

[95] S.-Y. Ding, et al. Nanostructure-based plasmon-enhanced Raman spectroscopy for surface analysis of materials. Nat. Rev. Mater. **1**, 16021 (2016).

[96] N. Hayazawa, Y. Inouye,, Z. Sekkat, S. Kawata, Metallized tip amplification of near-field Raman scattering. Opt. Commun. 183, 333–336 (2000).

[97] M. S. Anderson, Locally enhanced Raman spectroscopy with an atomic force microscope. Appl. Phys. Lett. **76**, 3130–3132 (2000).

[98] R. M. Stöckle, Y. D. Suh, V. Deckert, R. Zenobi, Nanoscale chemical analysis by tip-enhanced Raman spectroscopy. Chem. Phys. Lett. **318**, 131–136 (2000).

[99] D. A. Long, The Raman Effect: A unified treatment of the theory of raman scattering by molecules; Wiley: Chichester, U.K., (2002).

[100] M. Moskovits, Surface-enhanced spectroscopy. Rev. Mod. Phys. **57**, 783−826 (1985).

[101] C. C. Neacsu, S. Berweger, M. B. Raschke, Tip-enhanced raman imaging and nanospectroscopy: sensitivity, symmetry, and selection rules. NanoBiotechnology **3**, 172– 196 (2007).

[102] J. K. Sass, H. Neff, M. Moskovits, S. Holloway, Electric Field Gradient Effects on the Spectroscopy of Adsorbed Molecules J. Phys. Chem. **85**, 621– 623 (1981).

[103] E. Poliani, M. R. Wagner, A. Vierck, F. Herziger, C. Nenstiel, F. Gannott, Breakdown of far-field Raman selection rules by light–plasmon coupling demonstrated by tip-enhanced Raman scattering. J. Phys. Chem. Lett. **8** 5462–71 (2017).

[104] S. Sheng, *et al.* Vibrational properties of a monolayer silicene sheet studied by tip-enhanced Raman spectroscopy. Phys. Rev. Lett. **119**, 196803 (2017).

[105] J. Steidtner, B. Pettinger. High-resolution microscope for tip-enhanced optical processes in ultrahigh vacuum. Rev. of Sci. Inst. **78** 103104, (2007).

[106] Z. Zhang, *et al*. Insights into the nature of plasmon-driven catalytic reactions revealed by HV-TERS. Nanoscale, **5**, 3249–52, (2013)

[107] N. Jiang, E. T. Foley, J. M. Klingsporn, M. D. Sonntag, N. A. Valley, J. A. Dieringer, T. Seideman, G. C. Schatz, M. C. Hersam, and R. P. Van Duyne. Observation of multiple vibrational modes in ultrahigh vacuum tip-enhanced Raman spectroscopy combined with molecular-resolution scanning tunneling microscopy. Nano letters, **12**, 5061–7, (2012).

[108] S. Sheng, W. Li, J. Gou, P. Cheng, L. Chen, K. Wu. Low-temperature, ultrahigh-vacuum tip-enhanced Raman spectroscopy combined with molecular beam epitaxy for in situ two-dimensional materials' studies. Rev. Sci. Instrum. **89**, 053107 (2018).

[109] C. C. Neacsu, J. Dreyer, N. Behr, M. B. Raschke, Scanning-probe Raman spectroscopy with single-molecule sensitivity. Phys. Rev. B **73**, 193406 (2006).

[110] M. D. Sonntag, et al. Single-molecule tip-enhanced Raman spectroscopy. J. Phys. Chem. C **116**, 478–483 (2012).

[111] A. Shiotari, T. Kumagai, M. Wolf, Tip-Enhanced Raman Spectroscopy of Graphene Nanoribbons on Au(111). J. Phys. Chem. C, **118**, 11806−11812 (2014).

[112] N. Venkateswaran, K. Sattler, J. Xhie, and M. Ge, Photon emission from nano-granular gold excited by electron tunneling. Surf. Sci. **274**, 199 (1992).

[113] N. J. Watkins, J. P. Long, Z. H. Kafafi, and A. J. Makinen, Fiber optic light collection system for scanning-tunneling-microscope-induced light emission. Rev. Sci. Instrum. **78**, 053707 (2007).

[114] S. Zhang, D. Huang, S. Wu, A cryogen-free low temperature scanning tunneling microscope capable of inelastic electron tunneling spectroscopy. Rev. Sci. Instrum. **87**, 063701 (2016).

[115] P. Verma, Tip-Enhanced Raman Spectroscopy: Technique and Recent Advances. Chem. Rev. **117**, 6447–6466 (2017).

[116] R. Berndt, R. R. Schlittler, and J. K. Cimzewski, High resolution atomic force microscopy potentiometry. J. Vac. Sci. Technol. B **9**,573 (1991).

[117] R. Berndt, J. K. Gimzewski, and P. Johansson, Inelastic tunneling excitation of tip-induced plasmon modes on noble-metal surfaces. Phys. Rev. Lett. **67**, 3796 (1991).

[118] A. Shiotari, B.-H. Liu, S. Jaekel, L. Grill, S. Shaikhutdinov, H.-J. Freund, M.Wolf, T. Kumagai, Local Characterization of Ultrathin ZnO Layers on Ag(111) by Scanning Tunneling Microscopy and Atomic Force Microscopy. J. Phys. Chem. C **118**, 27428 (2015).

[119] M. L. Brongersma, N. J. Halas, P. Nordlander, Plasmon-induced hot carrier science and technology. *Nat. Nanotechnol.* **10**, 25-34 (2015).

[120] W. Zhu, R. Esteban, A. G. Borisov, J. J. Baumberg, P. Nordlander, H. J. Lezec, J. Aizpurua, K. B. Crozier, Quantum mechanical effects in plasmonic structures with subnanometre gaps Nat. Commun. **7**, 11495 (2016).

[121] M. Urbieta, M. Barbry, Y. Zhang, P. Koval, D. Sánchez-Portal, N. Zabala, J. Aizpurua, Atomic-scale lightning rod effect in plasmonic picocavities: a classical view to a quantum effect. ACS Nano **12**, 585– 595 (2018).

[122] B. Pettinger, P. Schambach, C. J. Villagómez, N. Scott, Tip-enhanced Raman spectroscopy: near-fields acting on a few molecules. *Ann. Rev. Phys. Chem.* **63**, 379-399 (2012).

[123] E. A. Pozzi, G. Goubert, N. Chiang, N. Jiang, C. T. Chapman, M. O. McAnally, A.-I. Henry, T. Seideman, G. C. Schatz, M. C. Hersam, and R. P. Van Duyne, Ultrahigh-vacuum tip-enhanced raman spectroscopy. *Chem. Rev.* **117**, 4961-4982 (2017).

[124] N. Tallarida, J. Lee, and V. A. Apkarian, Tip-Enhanced Raman Spectroscopy on the angstrom Scale: bare and CO-terminated Ag tips. *ACS Nano* **11**, 11393-11401 (2017).

[125] J. Lee, S. M. Perdue, D. Whitmore, V. A. Apkarian, Laser-induced scanning tunneling microscopy: Linear excitation of the junction plasmon. *J. Chem. Phys.* **133**, 104706 (2010).

[126] Y. Terada, S. Yoshida, O. Takeuchi, H. Shigekawa, Real-space imaging of transient carrier dynamics by nanoscale pump–probe microscopy. *Nat. Photon.* **4**, 869-874 (2010).

[127] A. Dolocan, D. P. Acharya, P. Zahl, P. Sutter, N. Camillone III, Two-Color Ultrafast Photoexcited Scanning Tunneling Microscopy. *J. Phys. Chem.* C **115**, 10033-10043 (2011).

[128] T. L. Cocker, V. Jelic, M. Gupta, S. J. Molesky, J. A. J. Burgess, G. De Los Reyes, L. V. Titova, Y. Y. Tsui, M. R. Freeman, F. A. Hegmann, An ultrafast terahertz scanning tunnelling microscope. *Nat. Photon.* **7**, 620-625 (2013).

[129] K. Yoshioka, I. Katayama, Y. Minami, M. Kitajima, S. Yoshida, H. Shigekawa, J. Takeda, Real-space coherent manipulation of electrons in a single tunnel junction by single-cycle terahertz electric fields. *Nat. Photon.* **10**, 762-765 (2016).

[130] T. L. Cocker, D. Peller, P. Yu, J. Repp, R. Huber, Tracking the ultrafast motion of a single molecule by femtosecond orbital imaging. *Nature* **539**, 263-267 (2016).

[131] S. Li, S. Chen, J. Li, R. Wu, W. Ho, Joint Space-Time Coherent Vibration Driven Conformational Transitions in a Single Molecule. *Phys. Rev. Lett.* **119**, 176002 (2017).

[132] S. Dey, D. Mirell, A. R. Perez, J. Lee, V. A. Apkarian, Nonlinear femtosecond laser induced scanning tunneling microscopy. *J. Chem. Phys.* **138**, 154202 (2013).

[133] S. Grafström, Photoassisted scanning tunneling microscopy. *J. Appl. Phys.* **91**, 1717-1753 (2002).

[134] M. L. Brongersma, N. J. Halas, P. Nordlander, Plasmon-induced hot carrier science and technology. *Nat. Nanotechnol.* **10**, 25-34 (2015).

[135] S. W. Wu, N. Ogawa, and W. Ho, Atomic-scale coupling of photons to single-molecule junctions. *Science* **312**, 1362-1365 (2006).

[136] S. W. Wu and W. Ho, Two-photon-induced hot-electron transfer to a single molecule in a scanning tunneling microscope. *Phys. Rev.* B **82**, 085444 (2010).

[137] J. Martínez-Blanco, S. Fölsch, Light emission from Ag(111) driven by inelastic tunneling in the field emission regime. J. Phys.: Condens. Matter **27**, 255008 (2015).

[138] T. Kumagai, S. Liu, A. Shiotari, D. Baugh, S. Shaikhutdinov, M. Wolf, Local electronic structure, work function, and line defect dynamics of ultrathin epitaxial ZnO layers on a Ag(111) surface. J. Phys.: Condens. Matter **28**, 494003 (2016).

[139] J. Aizpurua, S. P. Apell, R. Berndt, Role of tip shape in light emission from the scanning tunneling microscope. Phys. Rev. B **62**, 2065–2073 (2000).

[140] M. I. Stockman, Nanofocusing of optical energy in tapered plasmonic waveguides. Phys. Rev. Lett. **106**, 019901 (2011).

[141] C. Ropers, C. C. Neacsu, T. Elsaesser, M. Albrecht, M. B. Raschke, C. Lienau, Grating-coupling of surface plasmons onto metallic tips: A nanoconfined light source. Nano Lett. **7**, 2784–2788 (2007).

[142] T. Jung, Y. W. Mo, and F. J. Himpsel, Identification of Metals in Scanning Tunneling Microscopy via Image States. Phys. Rev. Lett. **74**, 1641-1644 (1995).

[143] M. Pivetta, F. Patthey, M. Stengel, A. Baldereschi, and W.-D. Schneider, Local work function Moiré pattern on ultrathin ionic films: NaCl on Ag(100). Phys. Rev. B **72**, 115404 (2005).

[144] P. Ruffieux, K. Aït-Mansour, A. Bendounan, R. Fasel, L. Patthey, P. Gröning, and O. Gröning, Mapping the electronic surface potential of nanostructured surfaces. Phys. Rev. Lett. **102**, 086807 (2009).

[145] K. Schouteden and C. Van Haesendonck, Quantum confinement of hot image-potential state electrons. Phys. Rev. Lett. **103**, 266805 (2009).

[146] F. Craes, S. Runte, J. Klinkhammer, M. Kralj, T. Michely, C. Busse, Mapping Image Potential States on Graphene Quantum Dots. Phys. Rev. Lett. **111**, 056804 (2013).

[147] E. V. Chulkov, V. M. Silkina, P. M. Echenique, Image potential states on metal surfaces: binding energies and wave functions. Surf. Sci. **437**, 330–352 (1999).

[148] J. Zuloaga, E. Prodan, P. Nordlander, Quantum Description of the Plasmon Resonances of a Nanoparticle Dimer. Nano Lett. **9**, 887–891 (2009).

[149] R. Esteban, A. G. Borisov, P. Nordlander, J. Aizpurua, Bridging quantum and classical plasmonics with a quantum-corrected model. Nat. Commun. **3**, 825 (2012).

[150] C. Ciracì, R. T. Hill, J. J. Mock, Y. Urzhumov, A. I. Fernández-Domínguez, S. A. Maier, J. B. Pendry, A. Chilkoti, D. R. Smith, Probing the ultimate limits of plasmonic enhancement. Science **337**, 1072–1074 (2012).

[151] K. J. Savage, M. M. Hawkeye, R. Esteban, A. G. Borisov, J. Aizpurua, J. J. Baumberg, Revealing the quantum regime in tunnelling plasmonics. Nature **491**, 547–577 (2012).

[152] J. A. Scholl, A. García-Etxarri, A. Leen Koh, J. A. Dionne, Observation of quantum tunneling between two plasmonic nanoparticles. Nano Lett. **13**, 564–569 (2013).

[153] D. B. Dougherty, P. Maksymovych, J. Lee, M. Feng, H. Petek, and J. T. Yates, Jr. Tunneling spectroscopy of Stark-shifted image potential states on Cu and Au surfaces. Phys. Rev. B **76**, 125428 (2007).

[154] W. Zhu, R. Esteban, A. G. Borisov, J. J. Baumberg, P. Nordlander, H. J. Lezec, J. Aizpurua, and K. B. Crozier, Quantum mechanical effects in plasmonic structures with subnanometre gaps. Nat. Commun. **7**, 11495 (2016).

[155] Ellmer, K.; Klein, A.; Rech, B., Eds.; Transparent conductive Zinc Oxide: basics and applications in thin film solar cells; Springer Series in Materials Science 104; Springer: Berlin, (2008).

[156] C. V. Ovesen, B. S. Clausen, J. Schiøtz, P. Stoltze, H. Topsøe, J. K. Nørskov, Kinetic Implications of Dynamical Changes in Catalyst Morphology during Methanol Synthesis over Cu/ZnO Catalysts J. Catal. **168**, 133–142 (1997).

[157] Ü. Özgür, Y.I. Alivov, C. Liu, A. Teke, M. A. Reshchikov, S. Doğan, V. Avrutin, S.-J. Cho H. Morkoç, A comprehensive review of ZnO materials and devices. J. Appl. Phys. **98**, 041301 (2005).

[158] J. Goniakowski, F. Finocchi, C. Noguera, Polarity of oxide surfaces and nanostructures. Rep. Prog. Phys. **71**, 016501 (2008).

[159] C. Noguera, Polar oxide surfaces. J. Phys.: Condens. Matter **12**, R367 (2000).

[160] C. Tusche, H. L. Meyerheim, J. Kirschner, Observation of depolarized ZnO(0001) monolayers: formation of unreconstructed planar sheets. Phys. Rev. Lett. **99**, 026102 (2007).

[161] B. Bieniek, Ultra thin ZnO on metal substrates: An ab initio study. PhD Thesis Technischen Universität, Berlin (2016).

[162] B.-H. Liu, J. A. Boscoboinik, Y. Cui, S. Shaikhutdinov, H.-J. Freund, Stabilization of ultrathin zinc oxide films on metals: reconstruction versus hydroxylation. J. Phys. Chem. C **119**, 7842 (2015).

[163] J. Lee, *et al.* Tunable Lattice Constant and Band Gap of Single- and Few-Layer ZnO. J. Phys. Chem. Lett. **7**, 1335 (2016).

[164] J. Li, W.-D. Schneider, R. Berndt, Local density of states from spectroscopic scanning-tunneling-microscope images: Ag(111). Phys. Rev. B **56**, 7656 (1997).

[165] S. Grothe, et al. Quantifying many-body effects by high-resolution Fourier transform scanning tunneling spectroscopy. Phys. Rev. Lett. **111**, 246804–246805 (2013)

[166] M. Topsakal, S. Cahangirov, E. Bekaroglu, S. Ciraci, First-principles study of zinc oxide honeycomb structures. Phys. Rev. B **80**, 235119 (2009).

[167] M. Pivetta, F. Patthey, M. Stengel, A. Baldereschi, W.-D. Schneider, Local work function Moiré pattern on ultrathin ionic films: NaCl on Ag(100). Phys. Rev. B **72**, 115404 (2005).

[168] J. M. Blanco, S. Fölsch, Light emission from Ag(111) driven by inelastic tunneling in the field emission regime. J. Phys.: Condens. Matt. **27**, 255008 (2015).

[169] D. Dougherty, P. Maksymovych, J. Lee, M. Feng, H. Petek, J. Yates, Tunneling spectroscopy of Stark-shifted image potential states on Cu and Au surfaces. Phys. Rev. B **76**, 125428 (2007).

[170] C. L. Lin, et al. Manifestation of work function difference in high order Gundlach oscillation. Phys. Rev. Lett. **99,** 216103 (2007).

[171] D. Woodruff, W. Royer, N. Smith, Empty surface states, image states, and band edge on Au (111). Phys. Rev. B **34**, 764 (1986).

[172] G. Binnig, K. H. Frank, H. Fuchs, N. Garcia, B. Reihl, H. Rohrer, F. Salvan, A. R. Williams, Tunneling spectroscopy and inverse photoemission: image and field states. Phys. Rev. Lett. **55**, 991 (1985).

[173] M. Rohleder, W. Berthold, J. Güdde, U. Höfer, Time-Resolved Two-photon photoemission of buried interface states in Ar/Cu(100). Phys. Rev. Lett. **94**, 017401 (2005).

[174] M. Rohleder, K. Duncker, W. Berthold, J. Güdde, U. Höfer, photon photoemission. New J. Phys. **7**, 103 (2005).

[175] S. Schintke, *et al.* Insulator at the Ultrathin Limit: MgO on Ag (001). Phys. Rev. Lett. **87**, 276801 (2001)

[176] H.-C. Ploigt, C. Brun, M. Pivetta, F. Patthey, W.-D. Schneider, Local work function changes determined by field emission resonances: NaCl/Ag(100). Phys. Rev. B **76**, 195404 (2007)

[177] P. Ruffieux, K. Aït-Mansour, A. Bendounan, R. Fasel, L. Patthey, P. Gröning, O. Gröning, Mapping the electronic surface potential of nanostructured surfaces. Phys. Rev. Lett. **102**, 086807 (2009).

[178] O. Kolesnychenko, Y. Kolesnichenko, O. Shklyarevskii, H. V. Kempen, Field-emission resonance measurements with mechanically controlled break junctions. Physica B **291**, 246 (2000).

[179] M. Chelvayphan, C. Mee, Work function measurements on (110), (100) and (111) surfaces of silver. J. Phys. C: Solid State Phys. **15**, 2305 (1982).

[180] T, König, G, H, Simon, H.-P. Rust, M. Heyde, Work function measurements of thin oxide films on metals—MgO on Ag(001). J. Phys. Chem. C **113**, 11301 (2009).

[181] I. Demiroglu, S. T. Bromley, Evidence for multi-polymorphic islands during epitaxial growth of ZnO on Ag(1 1 1). J. Phys.: Condens. Matter **28**, 224007 (2016).

[182] L. Giordano, F. Cinquini, G. Pacchioni, Tuning the surface metal work function by deposition of ultrathin oxide films: Density functional calculations. Phys. Rev. B **73**, 045414 (2005).

[183] C.-l. Chiang, C. Xu, Z. Han, and W. Ho, Real-space imaging of molecular structure and chemical bonding by single-molecule inelastic tunneling probe. Science **344**, 885 (2014)

[184] L. Gross, F. Mohn, N. Moll, P. Liljeroth, and G. Meyer, The Chemical Structure of a Molecule Resolved by Atomic Force Microscopy. Science **325**, 1110 (2009).

[185] A. Shiotari, Y. Sugimoto, Ultrahigh-resolution imaging of water networks by atomic force microscopy. Nat. Commun. **8**, 14313 (2017).

[186] J. Peng, J. Guo, P. Hapala, D.n. Cao, R. Ma, B. Cheng, L. Xu, M. Ondráček, P. Jelínek, E. Wang, and Y. Jiang, Weakly perturbative imaging of interfacial water with submolecular resolution by atomic force microscopy. Nat. Commun. **9**, 122 (2018).

[187] L. Gross, N. Moll, F. Mohn, A. Curioni, G. Meyer, F. Hanke, and M. Persson, High-resolution molecular orbital imaging using a p-Wave STM Tip. Phys. Rev. Lett. **107**, 086101 (2011).

[188] C. Wagner, R. Temirov, Tunnelling junctions with additional degrees of freedom: An extended toolbox of scanning probe microscopy. Prog. Surf. Sci. **90**, 194 (2015).

[189] O. Krejci, P. Hapala, M. Ondracek, and P. Jelinek, Principles and simulations of high-resolution STM imaging with a flexible tip apex. Phys. Rev. B **95**, 045407 (2017).

[190] A. Yu, S. Li, G. Czap, and W. Ho, J. Phys. Chem. C 119, 14737 (2015).

[191] J. A. Gupta, C. P. Lutz, A. J. Heinrich, D. M. Eigler, Strongly coverage-dependent excitations of adsorbed molecular hydrogen. Phys. Rev. B **71**, 115416 (2005).

[192] S. Li, A. Yu, F. Toledo, Z. Han, H. Wang, H. Y. He, R. Wu, W. Ho, Rotational and Vibrational excitations of a hydrogen molecule trapped within a nanocavity of tunable dimension. Phys. Rev. Lett. **111**, 146102 (2013).

[193] F. D. Natterer, F. Patthey, H. Brune, Resonant-Enhanced Spectroscopy of Molecular Rotations with a Scanning Tunneling Microscope. ACS Nano **8**, 7099 (2014).

[194] C. Lotze, M. Corso, K. J. Franke, F. von Oppen, and J. I. Pascual, Driving a macroscopic oscillator with the stochastic motion of a hydrogen molecule. Science **338**, 779 (2012).

[195] R. H. M. Smit, Y. Noat, C. Untiedt, N. D. Lang, M. C. van Hemert, J. M. van Ruitenbeek, Measurement of the conductance of a hydrogen molecule. Nature **419**, 906 (2002).

[196] M. Kiguchi, R. Stadler, I. S. Kristensen, D. Djukic, and J. M. van Ruitenbeek, Evidence for a single hydrogen molecule connected by an atomic chain. Phys. Rev. Lett. **98**, 146802 (2007).

[197] Sz. Csonka, A. Halbritter, G. Mihály, O. I. Shklyarevskii, S. Speller, H. van Kempen, Conductance of Pd-H nanojunctions. Phys. Rev. Lett. **93**, 016802 (2004).

[198] W. H. A. Thijssen, D. Djukic, A. F. Otte, R. H. Bremmer, J. M. van Ruitenbeek, Vibrationally induced two-Level systems in single-molecule junctions. Phys. Rev. Lett. **97**, 226806 (2006).

[199] A. Halbritter, P. Makk, Sz. Csonka, G. Mihály, Huge negative differential conductance in Au−H_2 molecular nanojunctions. Phys. Rev. B **77**, 075402 (2008).

[200] M. L. Trouwborst, E. H. Huisman, S. J. van der Molen, B. J. van Wees, Bistable hysteresis and resistance switching in hydrogen-gold junctions. Phys. Rev. B **80**, 081407(R) (2009).

[201] K. Miwa, H. Imada, S. Kawahara, Y. Kim, Effects of molecule-insulator interaction on geometric property of a single phthalocyanine molecule adsorbed on an ultrathin NaCl film. Phys. Rev. B **93**, 165419 (2016).

[202] M. Oobatake, T. Ooi, Determination of Energy Parameters in Lennard-Jones Potentials from Second Virial Coefficients. Prog. Theor. Phys. **48**, 2132 (1972).

[203] A. Yazdani, D. M. Eigler, N. D. Lang, Off-Resonance conduction through atomic wires. Science **272**, 1921 (1996).

[204] D. Henwood, J. D. Carey, Ab initio investigation of molecular hydrogen physisorption on graphene and carbon nanotubes. Phys. Rev. B **75**, 245413 (2007).

[205] P. T. Lam, P. V. Dung, A. Sugiyama, N. D. Duc, T. Shimoda, A. Fujiwara, D. H. Chi, First principles study of the physisorption of hydrogen molecule on graphene and carbon nanotube surfaces adhered by Pt atom. Comput. Mater. Sci. **49**, S15 (2010).

[206] U. Ozgur, Y. I. Alivov, C. Liu, A. Take, M. A. Reshchikov, S. Doğan, V. Avrutin, S. J. Cho, H. Morkoc, A comprehensive review of ZnO materials and devices. J. Appl. Phys. **98**, 041301 (2005).

[207] S. Sheng, *et al.* Vibrational properties of a monolayer silicene sheet studied by tip-enhanced Raman spectroscopy. Phys. Rev. Lett. **119**, 196803 (2017).

[208] H. Wang, G. Qin, G. Li, Q. Wang, M. Hu, Low thermal conductivity of monolayer ZnO and its anomalous temperature dependence. Phys. Chem. Chem. Phys. **19**, 12882–9 (2017).

[209] C. Peng, *et al.* Dependence of phonon transport properties with stacking thickness in layered ZnO. J. Phys. D: Appl. Phys. **51**, 315303 (2018).

[210] X. Zha, R.-q. Zhang, Z. Lin, Tuning thermal expansions of zinc oxide sheets by varying the layer thickness. Europhys. Lett. **107**, 26007 (2014).

[211] Y. Pennec, W. Auwärter, A. Schiffrin, A. Weber-Bargioni, A. Riemann, J. V. Barth, Supramolecular gratings for tuneable confinement of electrons on metal surfaces. Nat. Nanotechnol. **2**, 99–103 (2007).

[212] M. F. Crommie, C. P. Lutz, D. M. Eigler, Confinement of electrons to quantum corrals on a metal surface. Science **262**, 218–220 (1993).

[213] J. Lobo-Checa, M. Matena, K. Muller, J. H. Dil, F. Meier, L. H. Gade, T. A. Jung, M. Stohr, Band formation from coupled quantum dots formed by a nanoporous network on a copper surface science **325**, 300–303 (2009).

[214] F. Rossel, M. Pivetta, W.Schneider. Luminescence experiments on supported molecules with the scanning tunneling microscope. Surf. Sci. Rep. **65**,129-144 (2010).

[215] J. Aizpurua, S. P. Apell, R. Berndt, Role of tip shape in light emission from the scanning tunneling microscope. *Phys. Rev.* B **62**, 2065-2073 (2000).

[216] I. Demiroglu, D. Stradi, F. Illas, S. T. Bromley, A theoretical study of a ZnO graphene analogue: adsorption on Ag(111) and hydrogen transport. J. Phys.: Condens. Matter **23**, 334215 (2011).

[217] S. C. Li, J. G. Wang, P. Jacobson, X. Q. Gong, A. Selloni, U. Diebold, Correlation between Bonding Geometry and Band Gap States at Organic−Inorganic Interfaces: Catechol on Rutile TiO2(110). J. Am. Chem. Soc. **131**, 980–984 (2009).

[218] N. Agrait, A. L. Yeyati, J. M. van Ruitenbeek, Quantum properties of atomic-sized conductors. Phys. Rep. **377**, 81–279 (2003).

[219] W. Zhu, R. Esteban, A. G. Borisov, J. J. Baumberg, P. Nordlander, H. J. Lezec, J. Aizpurua, K. B. Crozier, Quantum mechanical effects in plasmonic structures with subnanometre gaps. Nat. Commun. **7**, 11495 (2016).

Publications

Publications within this thesis

S. Liu, M. Müller, Y. Sun, I. Hamada, A. Hammud, M. Wolf, T. Kumagai. Resolving the Correlation between Tip-Enhanced Resonance Raman Scattering and Local Electronic States with 1 nm Resolution. *Nano Lett.*, 19, 3, 5725–5731 (2019).

S. Liu, M. Wolf, T. Kumagai. Plasmon-Assisted Resonant Electron Tunneling in a Scanning Tunneling Microscope Junction. *Phys. Rev. Lett.* 121, 226802 (2018).

S. Liu, A. Shiotari, D. Baugh, M. Wolf, T. Kumagai. Enhanced resolution imaging of ultrathin ZnO layers on Ag(111) by multiple hydrogen molecules in a scanning tunneling microscope junction. *Phys. Rev. B* 97, 195417 (2018).

T. Kumagai, S. Liu, A. Shiotari, D. Baugh, S. Shaikhutdinov, & M. Wolf. Local electronic structure, work function, and line defect dynamics of ultrathin epitaxial ZnO layers on a Ag(111) surface (Invited, Special Issue "Emerging Leaders"). *J. Phys.: Condens. Matter* 28, 494003 (2016).

Publications concering other topics

S. Liu, D. Baugh, K. Motobayashi, X. Zhao, S. V. Levchenko, S. Gawinkowski, J. Waluk, L. Grill, M. Persson and T. Kumagai. Anharmonicity in a double hydrogen transfer reaction studied in a single porphycene molecule on a Cu(110) surface. *Phys. Chem. Chem. Phys.*, 20, 12112–12119 (2018).

H. Böckmann, S. Liu, M. Müller, A. Hammud, M. Wolf, and T. Kumagai. Near-Field Manipulation in a Scanning Tunneling Microscope Junction with Plasmonic Fabry-Pérot Tips. N*ano Lett.*, (accepted, online May 9, 2019).

H. Böckmann, S. Liu, J. Mielke, S. Gawinkowski, J. Waluk, L. Grill, M. Wolf, & T. Kumagai. Direct Observation of Photoinduced Tautomerization in Single Molecules at a Metal Surface. *Nano Lett.*, 16, 1034–1041 (2016).

J. N. Ladenthin, L. Grill, S. Gawinkowski, S. Liu, J. Waluk, & T. Kumagai. Hot Carrier-Induced Tautomerization within a Single Porphycene Molecule on Cu(111). *ACS Nano* 9, 7287–7295 (2015).

Acknowledgments

I want to thanks everyone who contributes to this thesis and it is impossible to finnish it without the helps.

I want to thanks Prof. Martin Wolf for giving me the opportunity to do this dissertation research project in the Department of Physical Chemistry of the Fritz-Haber Institute and also want to thank Prof. Dr. Stephanie Reich for being my second supervisor.

I would like to express my deep gratitude to my group leader Takashi Kumagai, who mentoring this research project in the Nanoscale Surface Chemistry Group, for guidance, teaching me a lot more than this dissertation.

Thanks to my group colleagues, Janina Ladenthin, Hannes Böckmann, Stefan Böttcher, Matthias Koch and my other colleagues in the department for the great research environment. I would like to express all my gratitude to my family and friends for always supporting me.

Selbstständigkeitserklärung

Ich erkläre, dass ich die vorliegende Arbeit selbstständig und nur unter Verwendung der angegebenen Literatur und Hilfsmittel angefertigt habe.

Berlin, Juni 2019

Shuyi Liu